Power Flow Control in LV Distribution Systems

This is a PhD Thesis

Original Citation:
Power Flow Control in LV Distribution Systems / De Santis, Dario. - (2018). [10.60576/poliba/iris/de-santis-dario_phd2018]

Availability:
This version is available at http://hdl.handle.net/11589/120394 since: 2018-01-16

Published version
Politecnico di Bari
DOI:10.60576/poliba/iris/de-santis-dario_phd2018

Terms of use:
Altro tipo di accesso

10 April 2024

Department of Electrical and Information Engineering

Electrical and Information Engineering

Ph.D. Program

SSD: ING-IND/33–Power Systems

Final Dissertation

Power Flow Control in LV Distribution Systems

---

by

Dario De Santis

_____

Referees:

Prof.ssa Regina Lamedica

Prof.ssa Eleonora Riva Sanseverino

Supervisor:

Prof. Massimo La Scala

_____

Coordinator of Ph.D. Program:

Prof. Vittorio Passaro

_____

_____

Course n°30, 01/11/2014-31/10/2017

Acknowledgements

I would like to thank my supervisor Professor Massimo La Scala for giving me the opportunity to do this wonderful study path and my sincere gratitude is reserved to my girlfriend Maddalena and my parents for their support during my Ph.D. course.

Furthermore, I want to thank Prof. Min Chen and Zhejiang University for their great hospitality.

Index

Introduction

One of the first applications of the power electronics is the HVDC system to obtain direct currents from alternate currents in the high voltage system, but in LV and MV distribution systems it was not very used because it was very expensive. With the PWM converters, the new device technologies (such as IGBT and MOSFET) and the reduction of the power electronics converters costs, it was possible to have photovoltaic or wind generators on the grid and it was possible to have some converters to supply ancillary services.

So, nowadays the power electronics for low voltage and medium voltage grids has a key role about distributed generations, storage systems, DC charging stations and some devices to improve the power quality. In particular, with the power converters, it is possible to solve some typical problems on LV grids such as the active power flow inversion, peak shaving, load balancing, voltage regulation and reactive power compensation. In this work, has been studied the state of the art of power electronics converters installed on LV grids and the new solutions has been designed to reduce costs, to have more control and to solve the typical problems on LV systems.

The focus on the Back to Back converter and the Unified Power Flow Controller has been made. These converters allow to manage the reactive power, the voltage level in the PCC (Point of Common Coupling) and the active and reactive power flow between two feeders. Furthermore, thanks to the improvement of electrical batteries, the electrical mobility market is growing so in LV grids there is an increment of DC and AC charging stations. For this reason, it has been chosen the DC charging station to design the new all-in-one solutions, so, in this way it has been possible to reach the goals of this work. Hence, two components for LV grids (using the power electronics converters) have been designed and tested. The first one consists in a DC charging station with a double three-phase power supply with an integrated UPFC and the second one consists in a DC charging station with an integrated B2B converter.

To test the new components designed in this work, the MATLAB/Simulink software has been used.

In the chapter 1 the LV grids typologies are presented, and the most important power electronics solutions used for LV grids are presented, instead, in the chapter 2 the new components are explained with the power scheme and the mathematical formulae. The plant equations to design the control systems for the proposed solutions are shown.

In the chapter 3 and 4 the design of the control systems and the test cases for the charging station with UPFC and B2B are explained. In particular, for the UPFC solution it is explained the design of the control system for the STATCOM and SSSC in dq synchronous rotating frame; to test the control design and to verify the mathematical formulae, two test cases has been made with the MATLAB\Simulink where in the first one the electrical vehicle is charged and with the SSSC one load is supplied by two grids. In the second test case, the solar energy is used to charge partially the EV and to supply partially the load avoiding the power flow inversion in one of two grids and it was tested the DC/DC control system. For the B2B solution, it is explained the design of the control system for both AC/DC converters in dq synchronous rotating frame; to test the control design and to verify the mathematical formulae, two test cases has been made where in the first one the electrical vehicle is charged, and one load is supplied by two grids, instead, in the second test case the solar energy is used to charge the EV and to supply partially the load avoiding the power flow inversion.

Finally, in conclusion, main considerations on this work are discussed.

CHAPTER 1
LV Grids and Power Electronics

1.1 Low voltage distribution grids

The electrical low voltage grid is an important structure to supply loads like public street lighting, public and private offices, homes, schools and small industries. Furthermore, nowadays due to the development of electrical batteries, LV grids also are very important to supply AC and DC charging stations for electrical mobility (cars and bus). The electrical grids can use DC systems or AC systems, the second one is the solution actually used in the distribution systems. There are three main topologies of these grids; the first one is the radial grid where there is only one supply point and one feeder to supply several loads, the second one is the loop grid where there is only one supply point but with two feeders in a loop configuration (open loop or closed loop) and the third solution consists in the meshed grid where there are several supply points. In figure 1.1 the radial solution is shown, in figure 1.2 and in figure 1.3 loop solutions are shown with open and closed configuration. Finally, in figure 1.4 the meshed grid is shown.

Figure 1.1: Radial AC LV Grid
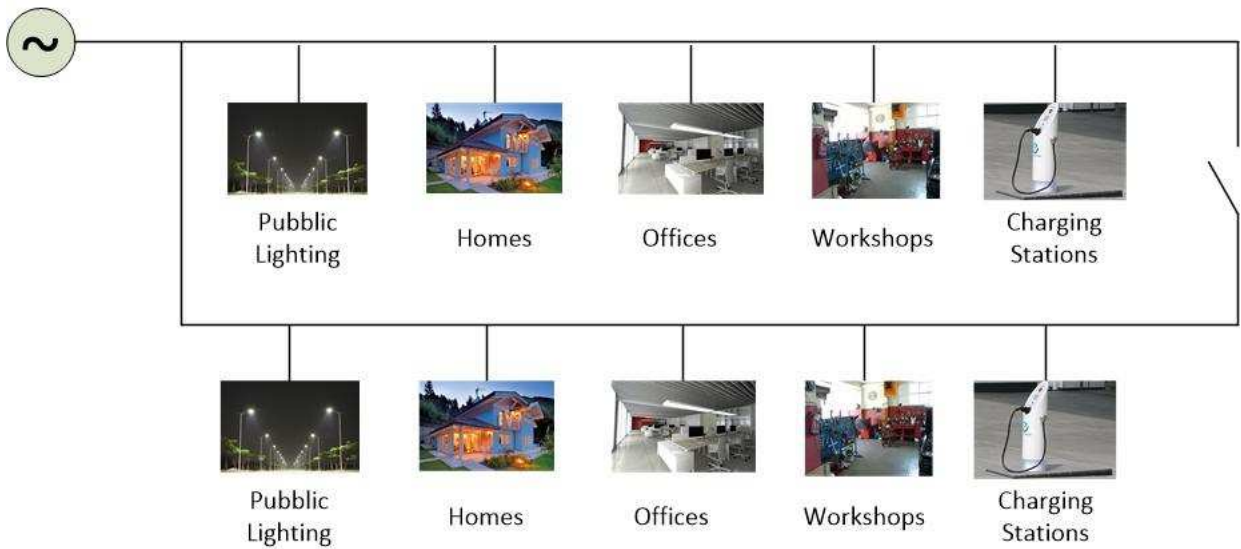
Figure 1.2: Open loop AC LV grid
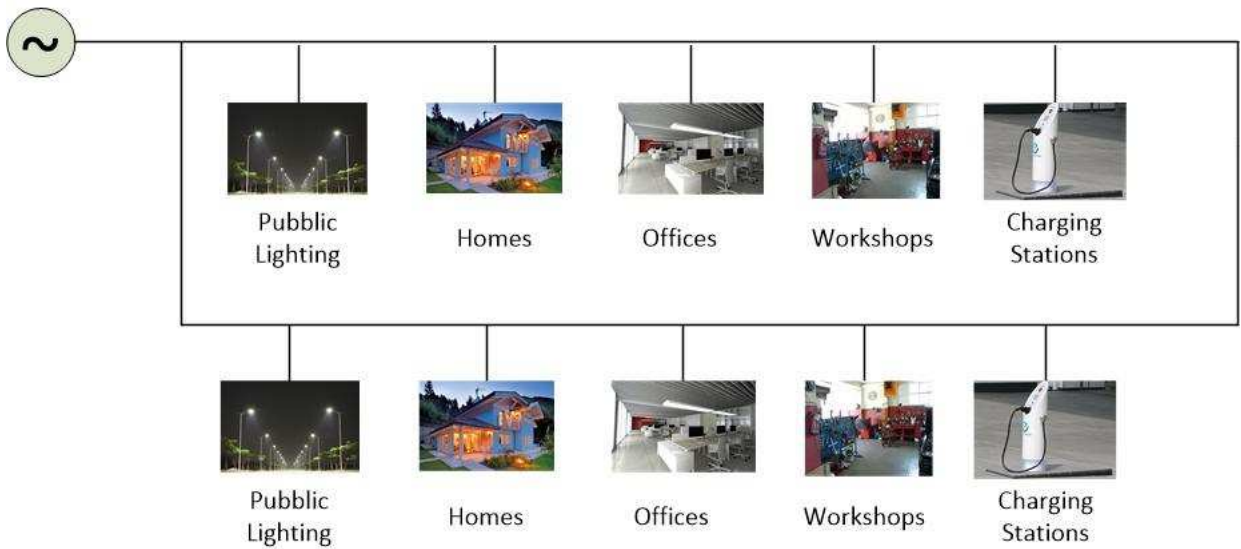
Figure 1.3: Closed loop AC LV grid
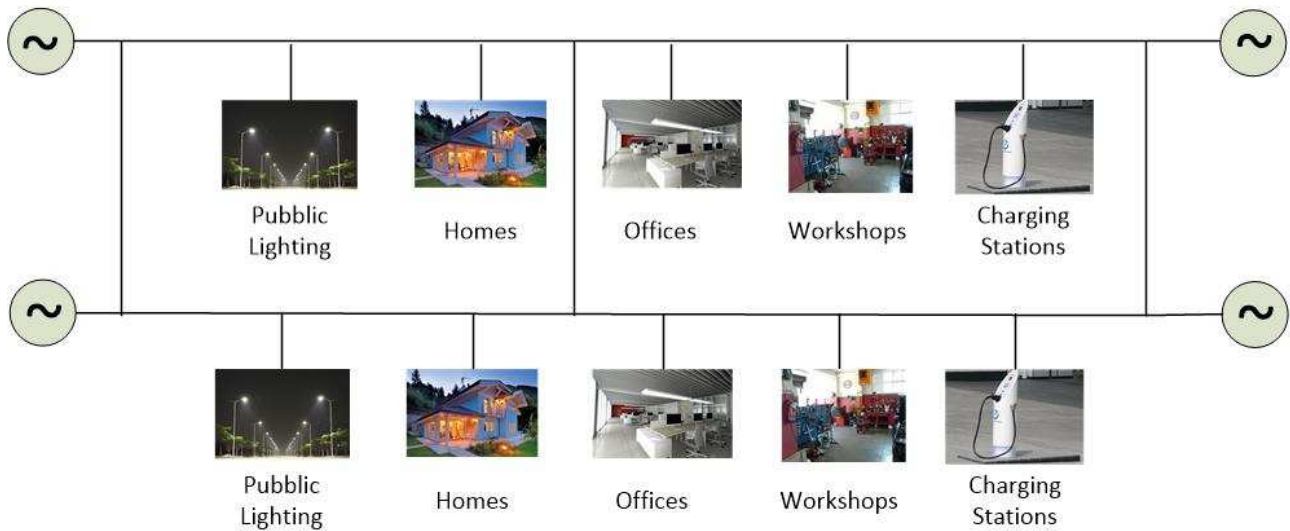
Figure 1.4: Meshed AC LV grid

The AC LV grids have different voltage levels; in Europe the line voltage equals 400 V, in China actually it is equal to 380 V, instead, in the United States the phase voltage is equal to 120 V. The power is supplied from medium voltage grids using step-down transformers in the classical low voltage grid. The power flow is unidirectional, from transmission grids to low voltage grids and the main power is supplied with thermal and hydro power plants with high power density.

1.2 Microgrids and distributed generation

The development of power electronics converters has allowed the growing of distributed generators such as solar generator, wind generator and tidal turbine so the traditional low voltage distribution system has changed in a new low voltage system where there are several Distributed Generation Systems (DGSs) and the power flow is not unidirectional every time but in the case of the excess of active power flow there is an energy flow inversion from LV distribution system to MV distribution system (from down to up). This aspect is most important in the management of low voltage grids, in fact, thanks to DGSs, it is possible to obtain a new power electrical system with a low voltage level (e.g., 400V) using storage

systems with the lithium technology or similar solutions [1] [2]. The Department of Energy (DOE) defines the microgrid as ''a group of interconnected loads and distributed energy resources within clearly defined electrical boundaries that acts as a single controllable entity with respect to the grid. A microgrid can connect and disconnect from the grid to enable it to operate in both grid-connected or island mode'' [3]. The microgrids can work in grid-connected or stand-alone operation modes. Particularly, the stand-alone operation, although may only for very limited period, can provide improved reliability to the smart grids. Some other systems, such as electric vehicles can be considered as always operating in standalone mode. Due to the intermittent nature of RE resources, other energy sources (such as diesel) and Storage Elements (SEs) are critical part to enable the stand-alone operation of microgrids or to smooth the microgrid power during grid-connected operation. SEs can be classified into two categories: capacity oriented energy storage and access-oriented energy storage. Capacity-oriented energy storage does not have fast response time, and they are used for long-term energy balancing to buffer out low-frequency power oscillation of DGs output power and compensate intermittency of RE sources in microgrids. Batteries, pumped hydroelectric systems, compressed air energy storage and hydrogen storage are types of capacity oriented energy storage. Access-oriented storage devices have fast response time, and they are responsible for short time disturbances in microgrids, by providing the high-frequency component of power. They can supply or absorb the high-power transients with high-power density. Flywheels, SuperCapacitors (SCs) and superconducting magnetic energy storage are considered as access-oriented storage devices [4]. In figure 1.5 an AC microgrid is shown, instead, in figure 1.6 a DC microgrid is shown.
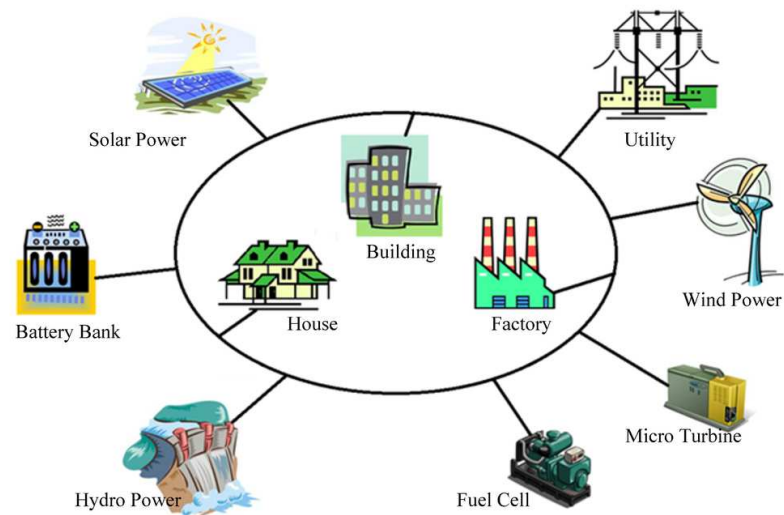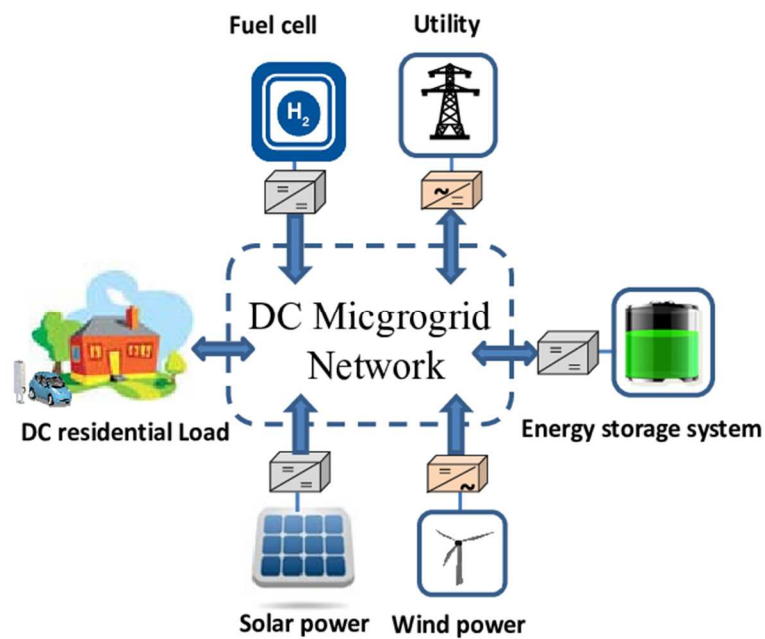
Figure 1.5: AC microgrid

Figure 1.6: DC microgrid

1.3 Power electronics on low voltage grids

On the low voltage grids there are new technologies to regulate the voltage and the reactive power and to manage active and reactive power flow in radial and meshed grids [5] due to low costs and to reliability of power electronics converters. So, today the power electronics has a key role for the future of electrical grids; for this reason, in this work, this aspect has been taken in consideration to design new components to control the active and the reactive power in LV grids.

1.3.1 Voltage and reactive control

In AC LV grids is most important to control the reactive and the voltage when the voltage profile is not ideal for the normal operations. To do this, it is possible to use the power electronics converters. These devices can be dedicated to regulate the reactive in the Point of Common Coupling (PCC) or they can be used to exchange active power with LV grids and at the same time, they can exchange reactive power with the grid. The first solution is composed of two main typologies; the STATic COMpensator (STATCOM) [6] and the Static Var Compensator (SVC) with the thyristor technology. The STATCOM is shown in figure 1.7, instead, the second solution is shown in figure 1.8, where an Active Front End (AFE) converter is used to exchange both active and reactive power. With the power electronics converters, it is possible to manage the reactive power or the voltage level in the PCC in the better way than the classical solution (with capacitors) with a very fast response and with a step-less solution. Furthermore, with the solution shown in figure 1.8, the reactive and voltage regulation is very cheap, because it is possible to regulate reactive and voltage with an all-in-one solution [7] [8].
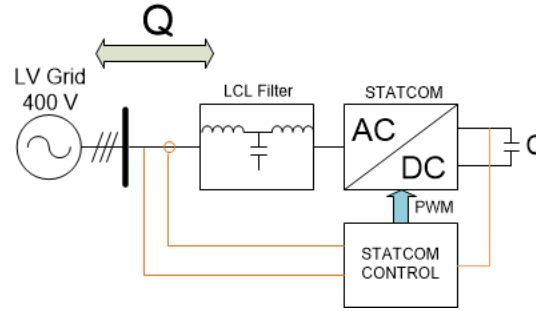
Figure 1.7: Power electronics converter to exchange only reactive power with the LV grid
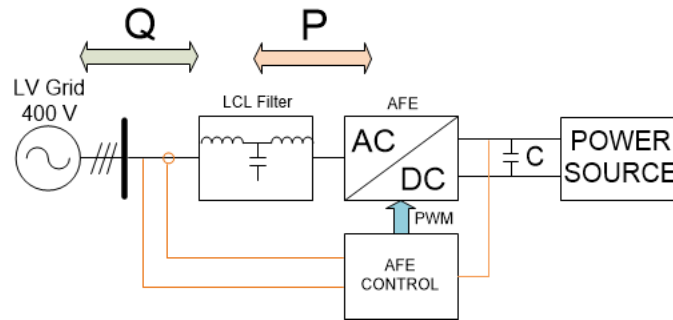
Figure 1.8: Power electronics converter to exchange reactive and active power with the LV grid

In figure 1.9 STATCOM control loop for direct component is shown, it is possible to see the direct current reference equals 0, in this way the power converter will be able to exchange only reactive power and it works as a static compensator. To control reactive power, it is possible to use the control loop shown in figure 1.10, where the reactive set-point is received from a central controller and thanks to the outer loop, it is possible to obtain the current reference for the current's inner loop. The STATCOM solution is very fast to follow the set-point and it doesn't have a step regulation. In figure 1.11 the control loop to use the STATCOM converter like SVC is shown, in this way, it is possible to control the voltage module in the PCC. To do this, the voltage module outer loop is used to obtain the current reference for the current's control loop.
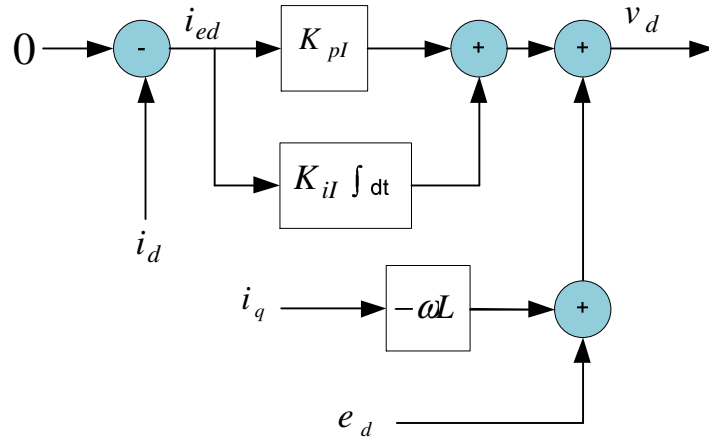
Figure 1.9: Direct current control's loop
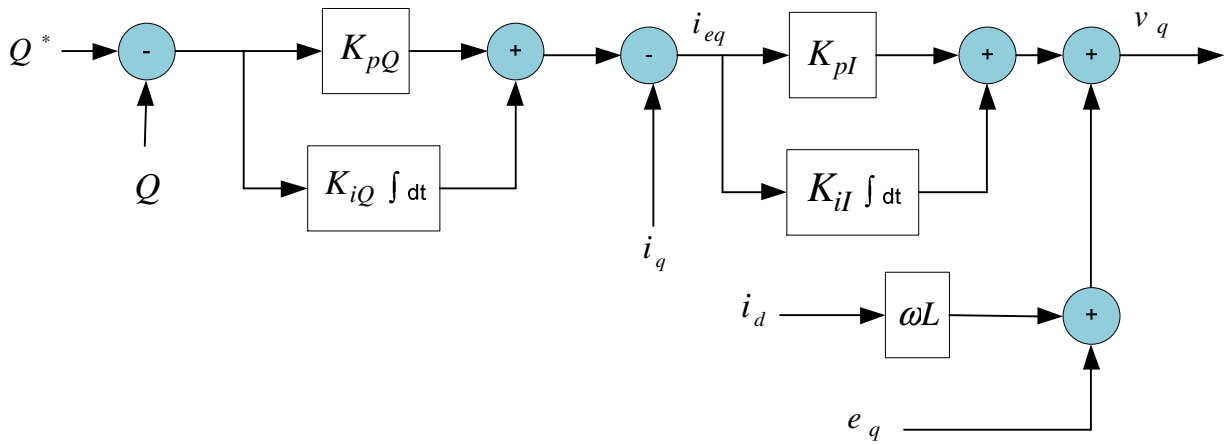
Figure 1.10: Quadrature current control's loop for reactive control
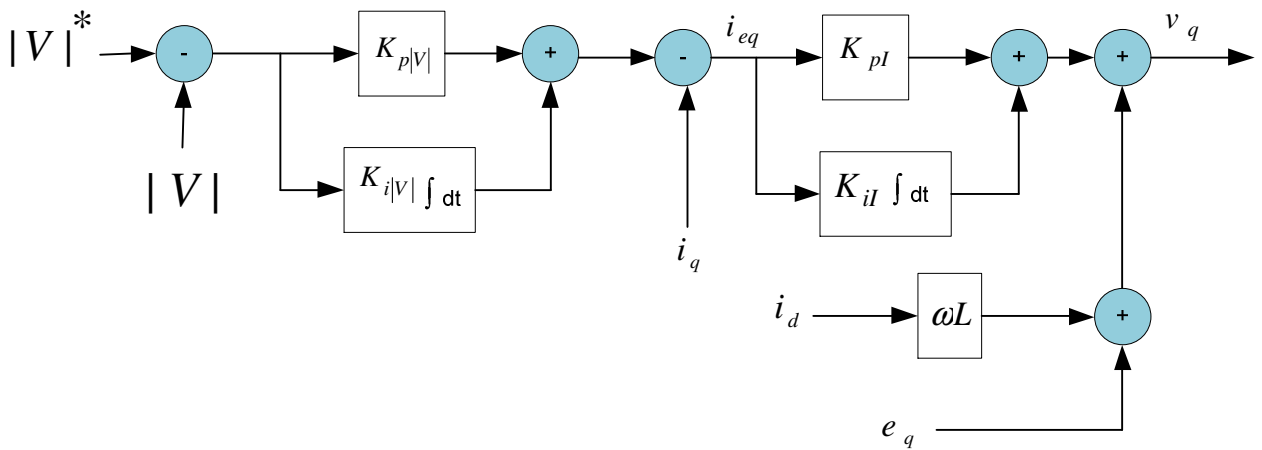
Figure 1.11: Quadrature current control's loop for voltage control

In figure 1.12 the AFE control loop for direct component is shown, where to exchange the active power with the LV grid there is an outer loop to control the DC link voltage. In this way the V_{DC} controller will be able to obtain the current reference for the inner loop. To control the reactive power, it is possible to use the control loop shown in figure 1.10, instead, to control the voltage level must be used the control loop shown in figure 1.11. The AFE converter can work as STATCOM, SVC and at the same time can be used to connect solar system or wind system to inject active power into the grid or can be used to interface a storage system to exchange the bidirectional active power flow with the grid. Furthermore, it is possible to add other functions to the AFE converter such as active filtering and power balancing. With this solution, it is not necessary to use other devices to regulate the reactive power or the voltage level on the grid.
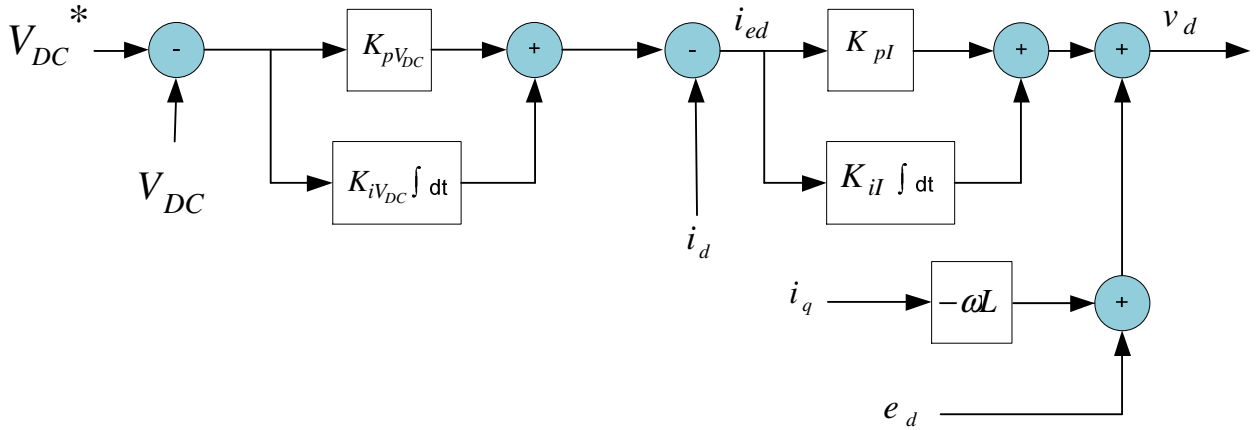
Figure 1.12: Direct current control's loop for active power

To compensate the reactive power on the LV grid, it is possible to use the thyristor technology to regulate capacitor or inductor current. An example is shown in figure 1.13, where are shown two SVC typologies with simplified schemes; the first one consists in a reactor current controlled with two thyristors in an anti-parallel connection, the second solution consists in capacitors switched by thyristors in an anti-parallel connection.
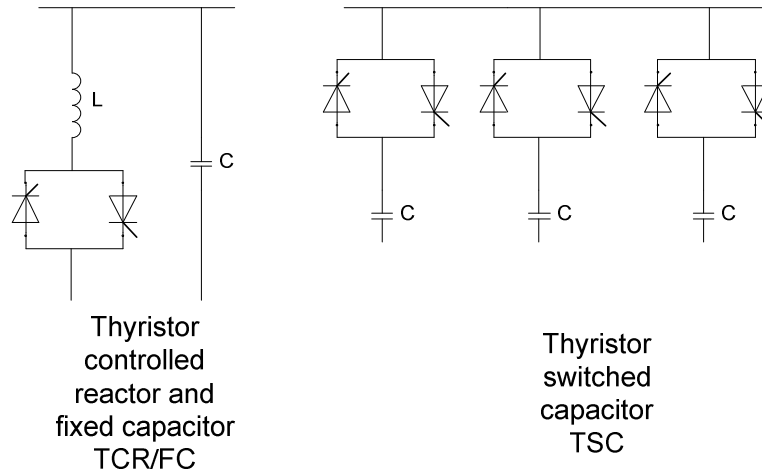
Figure 1.13: SVC with thyristor technology

1.3.2 Ancillary services with DC charging stations

With the PWM technology, it is possible to control the current and the voltage in the best way. So, it is possible to have a full control of the reactive and active power exchanged between the power electronics converter and the grid. In this way, the converters (for DC charging stations, photovoltaic generators, for storage systems, for wind systems and so on) can be used to manage the reactive or the voltage level in the PCC and at the same time they can exchange the active power in the bidirectional mode. An example is shown in figure 1.14, where is used a DC charging to charge a car and to exchange reactive power with the LV grid. Furthermore, using the auxiliary battery, it is possible to optimize the charging process and also to exchange active power with the grid to do peak shaving [7] [8].
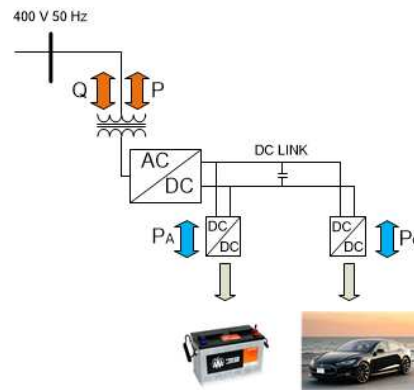
Figure 1.14: DC charging station with an AFE converter

14

In figure 1.15 are shown simulation results about all active and reactive powers for the DC charging station shown in figure 1.14; with the auxiliary battery (integrated in the DC charging station), the EV charging power is equal to 20 kW and it is kept constant, instead, the grid active power decreases from 20 kW to 10 kW. In this way, it is possible to avoid a congestion on the feeder and to optimize the EV charging time. So, in figure 1.16 is shown the simulation result about the grid current that decreases reducing the grid load.
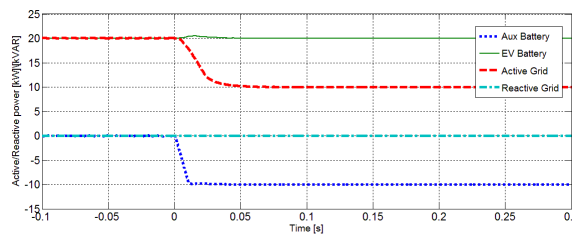
Figure 1.15: DC charging station active and reactive power
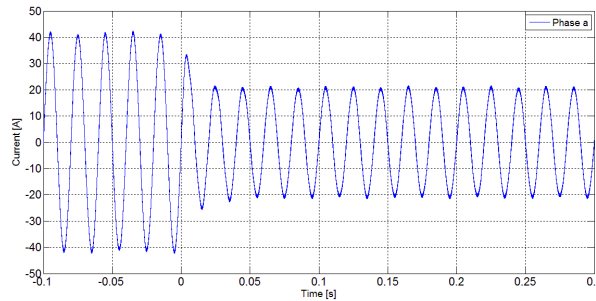
Figure 1.16: DC charging station phase a current

In figure 1.17 are shown simulation results about all active and reactive powers for the DC charging station shown in figure 1.14 with the active power injected in the grid; the auxiliary battery is used to charge the EV battery and it is able to supply the active power to the grid. This aspect is most important to do peak shaving or to reduce the grid load. Instead, in figure 1.18 the simulation result about the grid current is shown. It is possible to note the increasing of the grid current and the phase inversion.
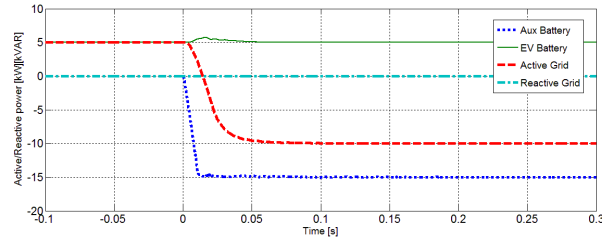
Figure 1.17: DC charging station active and reactive power
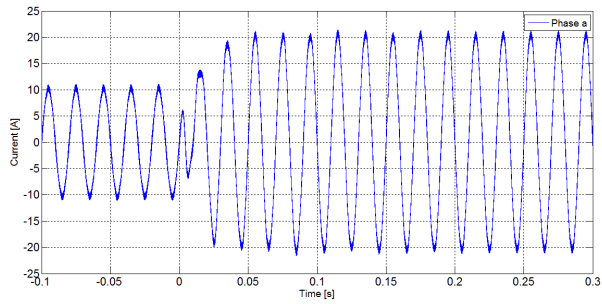
Figure 1.18: DC charging station phase a current

In figure 1.19 the simulation result about the PCC voltage (rms value) regulation is shown; using the $V_{DC}|V|$ control, the charging station is able to exchange reactive power with the grid to reach the voltage set-point. In this case the set-point is equal to 230 Vrms. This function is most important to control the voltage profile in LV grids.
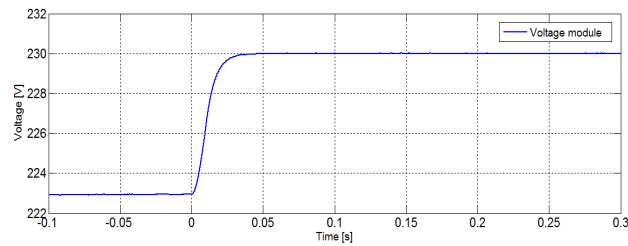
Figure 1.19: Voltage control

16

1.3.3 V2G charging stations

Due to the increasingly serious energy crisis and environment pollution issues, continuous development of the power storage battery technology and the arrival of the low-carbon era, EV has become an important direction of development of new energy vehicles, which is a significant means to solve energy and environment problems. With the increasing number of EV integration into the power system, the potential impact of EV on an electric utility could be substantial. In the aspects of generation side and transmission side, the effect is relatively small, but the impact on the distribution system can not be ignored. From the power system operator view, the load fluctuations and the power losses during charging are the significant concerns and have to be minimized. Not only load fluctuations, but also power quality (e.g., voltage profile, three-phase unbalance, harmonics, etc.) are essential to the system operator as well as to grid customers. In addition, a series of subsequent problem must be focused on, such as system planning, system efficiency, system reliability, EV user benefit, EV user convenience and so on. V2G concept was proposed by the above issues. V2G (Vehicle-to-Grid) is determined by Amory Lovins in 1995 firstly, and William Kempton developed it. The primary concept of V2G is that EVs can provide energy to the power system when it parked, battery of EVs can charge during low demand times and discharge when power is needed. In this way, the EV users buy electricity from the grid in the low price, and sell electricity in the high price to obtain a certain benefit. The V2G system offers a source of backup for renewable resources. These features can enable ancillary services including spinning reserve, black-start and control of voltage and frequency. Just as mentioned, the V2G has many benefits, but the most important is to solve the two problems which caused by EV integration into grid: harmonics pollution and load fluctuations. Meanwhile, it needs to bring benefits to the grid and EV users. Therefore, the study of solution to those two problems has great theoretical value and practical significance. In recent years, due to widespread use of EV and battery, V2G has received wide attention. V2G is still a relatively new concept, as an important part of the smart grid, it is research is still in its infancy.

V2G technology can achieve the following functions:

- Load balancing;

- Harmonics suppressing;

- Peak load shaving;

- System operation cost reducing;

- Load factors improving;

- Profit generating;

- Emission reducing;

- Tracking of variable renewable energy resources.

Up to now, V2G researches have been mainly focused on the economic feasibility, global structure and implementation method. In 2005, Willett Kempton from University of Delaware studied primary V2G problems: capacity calculation and system profit. In the same year, he researched the V2G implementation issues: stabilizing the grid to support large-scale renewable energy [9]. In 2009, Dirk Uwe Sauer from Germany published articles focused on the impacts from the mobile energy storage and the results showed that mobile storage systems consist of EVs and control systems can partially replace the static storage systems [10]. In [11], it researches the V2G application that the EVs join the peak modulation and establishes the V2G system model which provides the reference for the future research. Due to the diverse characteristics and different power supply function of EVs, some researches show that the V2G can be divided into four categories to achieve:

- centralized implementation. It is suitable for large-scale charging place. Taking centralized control and having great impact on the grid;

- autonomous implementation. The feature is flexible, convenient and free from time and place and so on. But it does not good to achieve unified management;

- based on micro-grid implementation. EVs integrate into the micro-grid rather than directly exchange the power from the grid. The EV also can be regarded as the energy storage system to achieve self-sufficient in a certain area;

- based on replacing battery implementation. In this model, battery types need to be unified.

At present, with the development of V2G, the key issues are as follows:

- intelligent dispatching from the grid view;

- smart charging management from the EV view;

- bi-directional charger;

- effect of V2G on battery.

To solve two great problems of the harmonics pollution and the load fluctuations from EVs, the researches focus on the bidirectional charger and the charging/discharging strategy.

Most of the conventional chargers are unidirectional, and they will cause the harmonics problems which will not meet the requirements in the power system. To achieve the V2G, we need to equip a two-way smart charger between the power grid and the EV. Battery charger play a critical role in the development of EV. The purpose is to ensure that can improve the efficiency, reduce the cost and volume and suppress total harmonic distortion under normal condition, and still it could have a good control performance when it is subjected to the external disturbance. From the literature, the research mainly focuses on the charger typology and the control strategy.

According to the different EV charger typology, it can be divided into the following three types:

- consisting of uncontrolled rectifier and chopper. The feature is large volume, large current harmonics of grid side and low efficiency. It is not suitable for access to the public grid;

- consisting of uncontrolled rectifier and DC-DC converter. The feature is large current harmonics of grid side (about 30%), low efficiency and low cost. It is the main charger on the market;

- consisting of PWM rectifier and DC-DC converter. The feature is small harmonic, high power factor, dual energy flow and so on.

A typical bidirectional charger has two stages: an active grid-connected bidirectional ac–dc converter that enforces power factor and a bidirectional dc–dc converter to regulate battery current. Bidirectional charging system is characterized by non-linearity, time varying and strong coupling, greatly challenging the control system design, especially when model inaccuracy and external disturbances are taken account in. So, the control requirements are very high. At present, the control methods are many: traditional linear/nonlinear control, modern nonlinear control and intelligent control. Such as: PID control, Active Disturbance Rejection Control (ADRC), fuzzy control, adaptive control, neural network control, Lyapunov stability theory control and so on. ADRC is proposed by Jingqing Han and Zhiqiang Gao developed it. Comparing PID and ADRC, the advantages of ADRC as follows:

- fast response, small overshoot;

- at steady state, the fluctuation of voltage or current is small;

- strong resistance to external disturbances.

But the drawback is its parameters are relatively large, it is hard to set parameters. Just as mentioned, there are many control methods, and the control mode is complex. The technology of the traditional control method is mature and easy to realize. The intelligent control needs not to set up a charger mathematics model, so, it is introduced into the control of the charger. But the intelligent control is still very immature, it still stays at the stage of simulation.

In summary, the bidirectional charger for research mainly includes the following aspects:

- charger structure;

- harmonic suppression from grid connection;

- charger operation efficiency [12].

1.3.4 Power flow control with UPFC

In LV grids with a closed loop or meshed configuration, it is possible to control active and reactive power flows between two feeders to reduce the active power losses in the loop or in the meshed grid. With the power flow control, it is possible to solve some typical problems in LV grids such as a power flow inversion in one of two feeders, a congestion problem in one feeder or it is possible to pilot the active power flow to use in the best way the green energy in the distribution system. For example, to avoid the waste of green power, it is possible to pilot the active power flow towards near loads with the power electronics converters. There are some devices to control active and reactive power flows, one of them is the Unified Power Flow Controller (UPFC) [13] [14]. The UPFC power scheme is shown in figure 1.20.
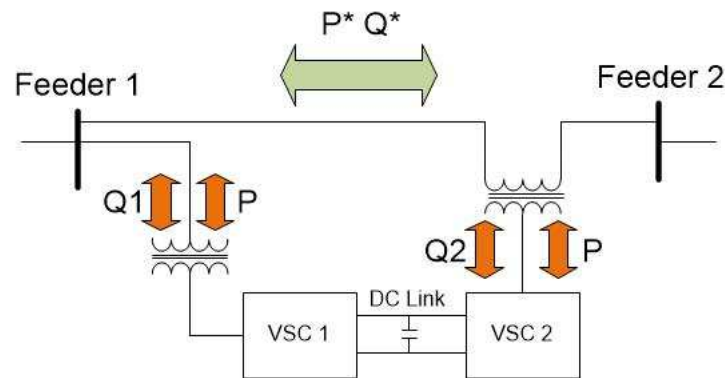
Figure 1.20: UPFC power scheme

In figure 1.21 a LV distribution system with a closed loop configuration is shown. There are two feeders with the loads and Distributed Generations (DGs). Using the UPFC, it is possible to manage the closed loop in the best way, in fact, the active and reactive power flows in both feeders are controlled. Furthermore, it is possible to have an open loop configuration and to change the configuration from open to close with a smooth transient.
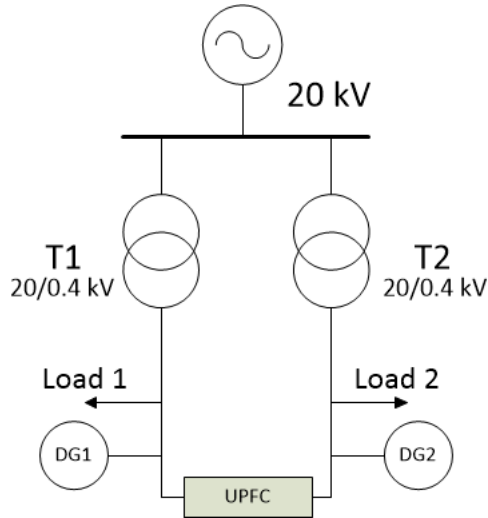
Figure 1.21: UPFC in the closed loop configuration

In figure 1.22 is shown an example of active and reactive power dynamic exchanged with the UPFC connected between two feeders (simulation results). In this case the reactive is equal to 0 before and after the UPFC operations, so, the device exchanges only the active power.
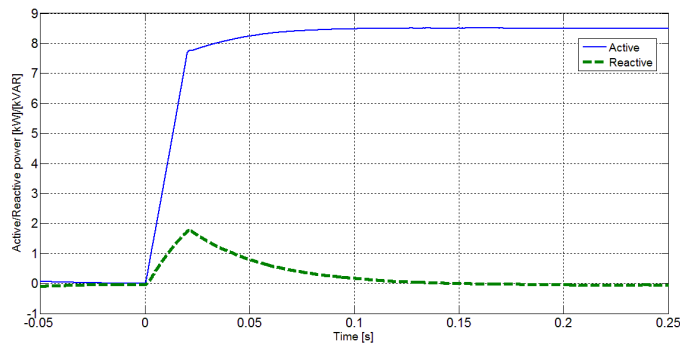
Figure 1.22: UPFC active and reactive power

In figure 1.23 are shown simulation results about the active and reactive power of the transformer 1, where the active power is reduced due to the UPFC and in figure 1.24 are shown simulation results about the active and reactive power of the transformer 2. The active power is increased to supply the load of the feeder 1.
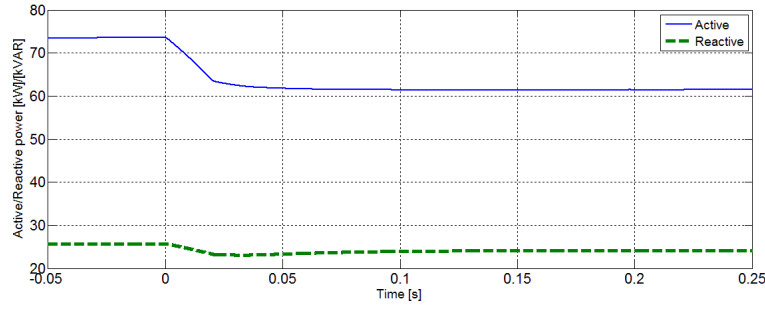
Figure 1.23: Transformer 1 active and reactive power
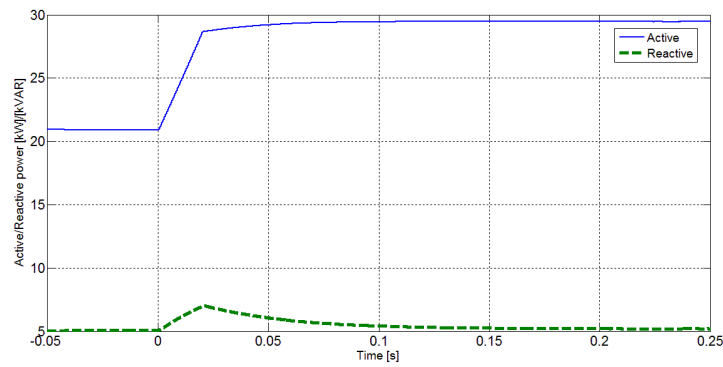
Figure 1.24: Transformer 2 active and reactive power

1.3.5 Power flow control with B2B

Another device to control power flows on LV grids between two feeders is the B2B (Back to Back) converter. This converter consists in two AC/DC converters connected to the common DC link. In figure 1.25 is shown the power scheme of B2B converter, where the master converter is used to manage active and reactive powers with PQ control mode to control the active power between two feeders and to control reactive power in the master converter PCC. Instead, the slave converter is used to control the DC link voltage and the reactive power in the slave converter PCC. The main difference with the UPFC solution is the decoupling between two feeders, so, the all active power flows through all converters, and this solution is more expensive than the UPFC solution but more flexible, because it is possible to control the reactive power or the voltage module independently for both PCCs [15] [16].

23
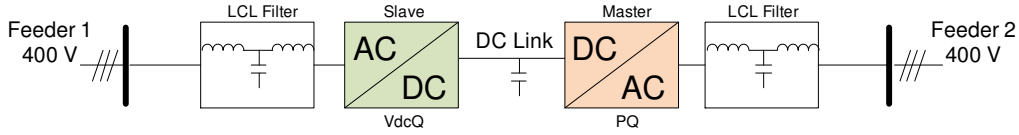
Figure 1.25: B2B power scheme

1.3.6 Droop control

Another important aspect, in a AC or DC microgrid, is the droop control for the voltage in DC microgrid and for the voltage and frequency in AC microgrid. The droop control is used to sharing the active power and the reactive power for each converter in automatic without any central controller in the island mode. While, in the grid-connected mode, thanks to the droop control, it is possible to do primary frequency and voltage regulations. In this way, it is possible to use a power electronics converter like a traditional generator [17]. In figure 1.26 and in figure 1.27 are shown the droop characteristics for a resistive/inductive equivalent impedance seen from the point of connection of the converter. In figure 1.28 the control scheme to implement the droop control in a AC microgrid in the case the converter operating as a current source or a voltage source is shown.
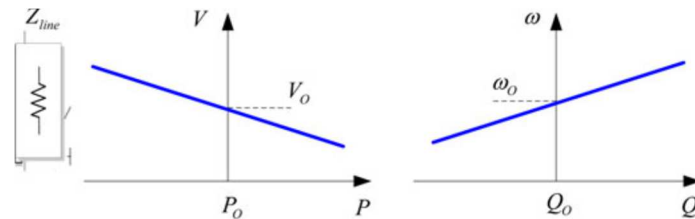
Figure 1.26: Droop control characteristic for a resistive line impedance
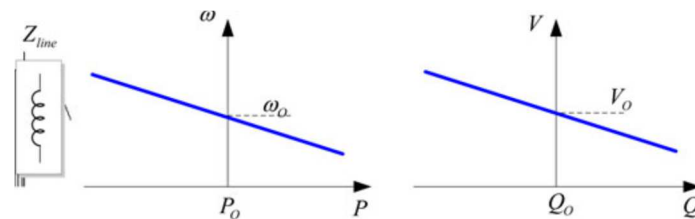
Figure 1.27: Droop control characteristic for an inductive line impedance
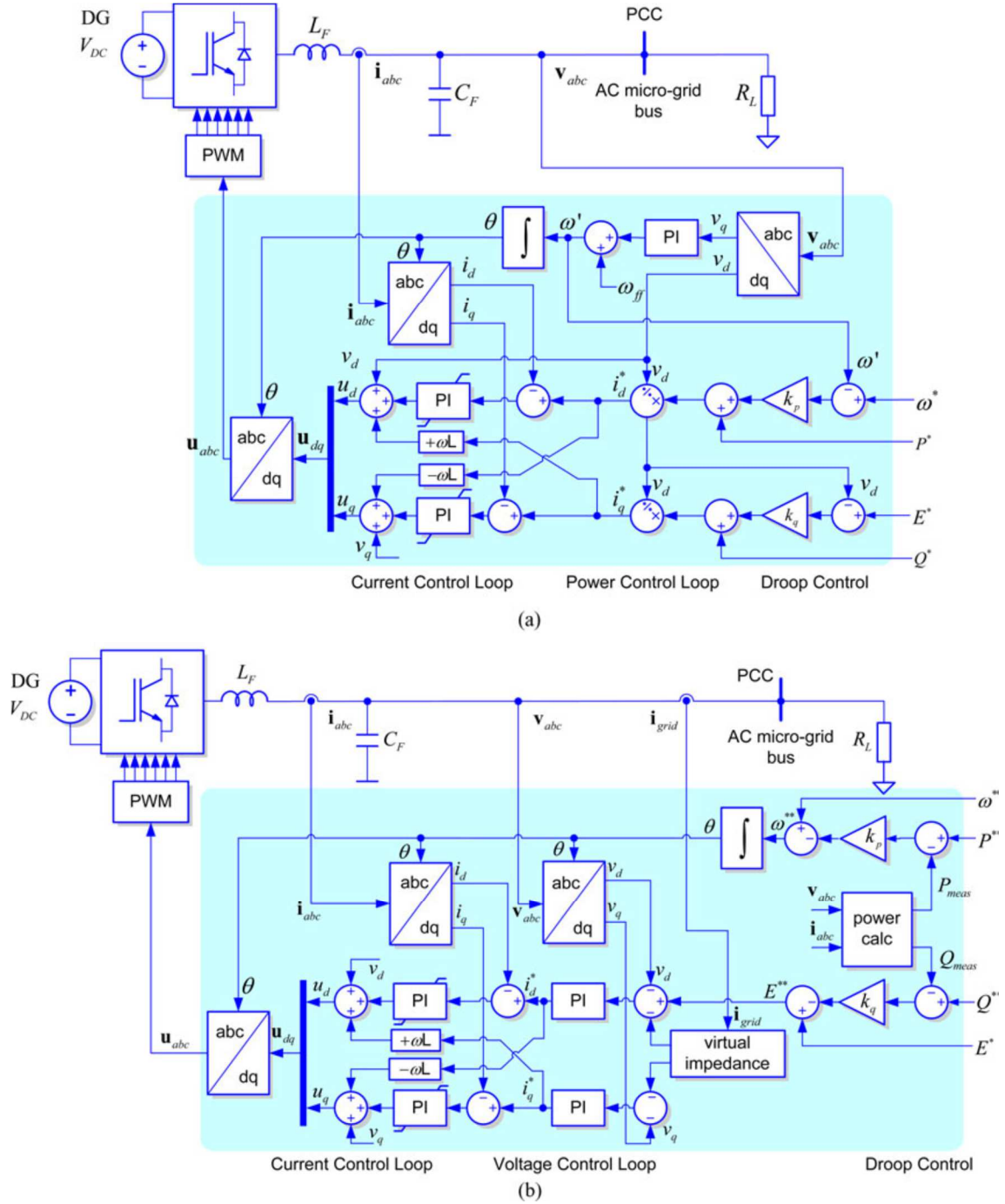
Figure 1.28: Droop control in inverter control scheme
(a) power converter as a current source (b) power converter as a voltage source

1.3.7 Virtual synchronous generator

Distributed power generation systems that use renewable energy resources such as solar panels and wind turbines have been developed in recent decades. As an inverter is usually installed at the output terminal, these systems are known as inverter-interfaced Distributed Generators (DGs). To facilitate the grid integration of DGs, the concept of "microgrid" is proposed to manage a cluster of DGs, Distributed Energy Storage Systems (DESSs) and nearby loads as a single sub-system. By applying microgrid configuration, the complexity of the power system introduced by DGs can be significantly reduced. Meanwhile, as a microgrid can operate in both island and grid-connected mode, high power supply reliability for internal loads can be obtained. The control system of a microgrid is usually in a hierarchical structure, in which the primary control level embedded in DGs is responsible for basic operation and the secondary (and sometimes a tertiary) control level installed in a Microgrid Central Controller (MGCC) is designed for optimal operations. Droop control is widely adopted in primary control level of microgrids, because it can provide automatic active and reactive power-sharing between DGs in island mode and seamless transition between the two operation modes.

However, unlike SGs (synchronous generators) with rotating mass, inverters have barely any inertia to support dynamic frequency stability. As a result, microgrids with high penetration rate of inverter-interfaced DGs may suffer from power quality issues such as large frequency deviation during loading transitions and fault events. To address this issue, Virtual Synchronous Generator (VSG) control or synchronverter inverter control methods to mimic dynamic characteristics of a SG by emulating the swing equation with virtual inertia and virtual damping factor, are proposed in the literature. It is demonstrated that thanks to the virtual inertia, VSG control results in lower frequency deviation during both loading transitions and fault events, thus improves the power quality of the microgrid. Control scheme embedded in the DGs using VSG concept is shown in figure 1.29.
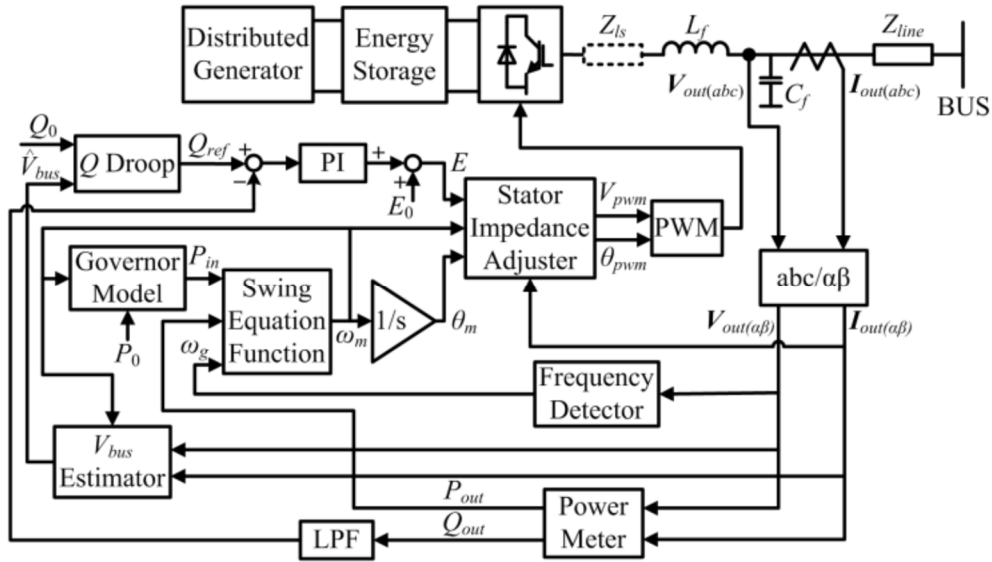
Figure 1.29: VSG control block diagram

Control scheme embedded in the DGs using VSG concept is shown in figure 1.29, where in the block "Swing Equation Function", the swing equation of the SG is emulated through iterative method to provide virtual inertia and damping. Instead, the "Stator Impedance Adjuster" block is to adjust the total output impedance of the DG by adding virtual stator impedance [18].

1.4 Smart monitoring system for LV grids

With the widespread diffusion of renewable and distributed energy sources such as solar or wind power plants, the energy flows through different grids, and in particular on medium and low voltage systems, have become bidirectional. Therefore, distribution systems have become active grids needing appropriate means to measure and manage extremely variable operating conditions. Many important progresses in this direction have been made on high and medium voltage grids, where great research and development efforts have been made to realize modern power electronic devices that can truly help systems operators to face a great range of operational issues such as primary and secondary regulation, voltage support, problems due to flow inversions, load unbalancing, congestions and so on. Low voltage grids, instead, have been still very slightly touched by this deep empowerment of electric networks, although they probably constitute the most important infrastructure of energy distribution system inside urban environments. These electrical networks, moreover, have very large extensions, so it is very important to use cheap, flexible and reliable monitoring systems [19] [20].

Furthermore, with the smart monitoring system it is possible to acquire time and position data for creating a time data logger and geo-localizing each device, thus, offering the possibility of real time fault localization. Fast identification and correction of faults and failures, together with other issues normally requiring the attention of utility companies, can reduce the overall power outage duration in a significant way [21] [22].

CHAPTER 2
New Components to Manage LV Grids

With the development of power electronics and electrical batteries, the market of Electrical Vehicles (EVs) is increasing, so in LV grids, it is most important to have DC and AC charging stations to charge the EV [23]. In this work, this aspect has been considered to research and design innovative solutions for electrical grids. The DC charging station is a better solution than the AC solution because to obtain the DC voltage is necessary to use a rectifier. This device can be passive or active, in the first case there is not any control possibility, instead, in the active solution it is possible to manage the reactive power in the PCC or the voltage level and with the bidirectional power converter the active power can flow towards the grid, so, the EV can supply the grid in Vehicle to Grid (V2G) mode or it is possible to integrate an auxiliary storage to optimize the charging process and to supply the grid for the peak shaving.

With the increase of distributed generation, the active power flow is not always unidirectional but when the total load in one feeder is lower, the inversion of the active power flow can occur. In this way, the green energy flows in the MV/LV transformer and in MV grids, and partially it will be lost in the cables and transformers, and the LV protections can work not well.

It is possible to manage in the best way the energy in the closed loop LV grids or LV meshed grids, so, it is possible to reduce the total active power losses and to have more load capability for all feeders. Of course, it is not easy to control a meshed LV grid in the same way of the radial configuration, but in particular cases, it is convenient to connect two feeders between them to solve overload problems in one of two feeders or the active power inversion, and to improve the voltage profile for all grid. Furthermore, it is possible to reduce the total active power losses with only single interline link to redistribute the active and reactive power flows in the grid.

Actually, in LV grids there are not installed any power electronics converters to manage active and reactive power flows between two feeders in a closed loop configuration and in a meshed configuration, instead, to connect two feeders are used electromechanical switches to change the grid configuration. In the academic literature was studied B2B or UPFC power electronics converters on LV and MV grids, and in the high voltage grids are used UPFC or B2B converters to manage active and reactive power flows. In figure 2.1 is shown two electric feeders connected in two points with PE devices, where there are distributed generators, charging stations, storage systems and classical AC loads. Practically, the two radial grids are two microgrids, and they can be controlled independently; with the interline link, it is possible to control active and reactive power flows between two feeders and to redistribute the power flows into a new meshed grid, in fact, PE converters realize a new meshed grid with two supply points.
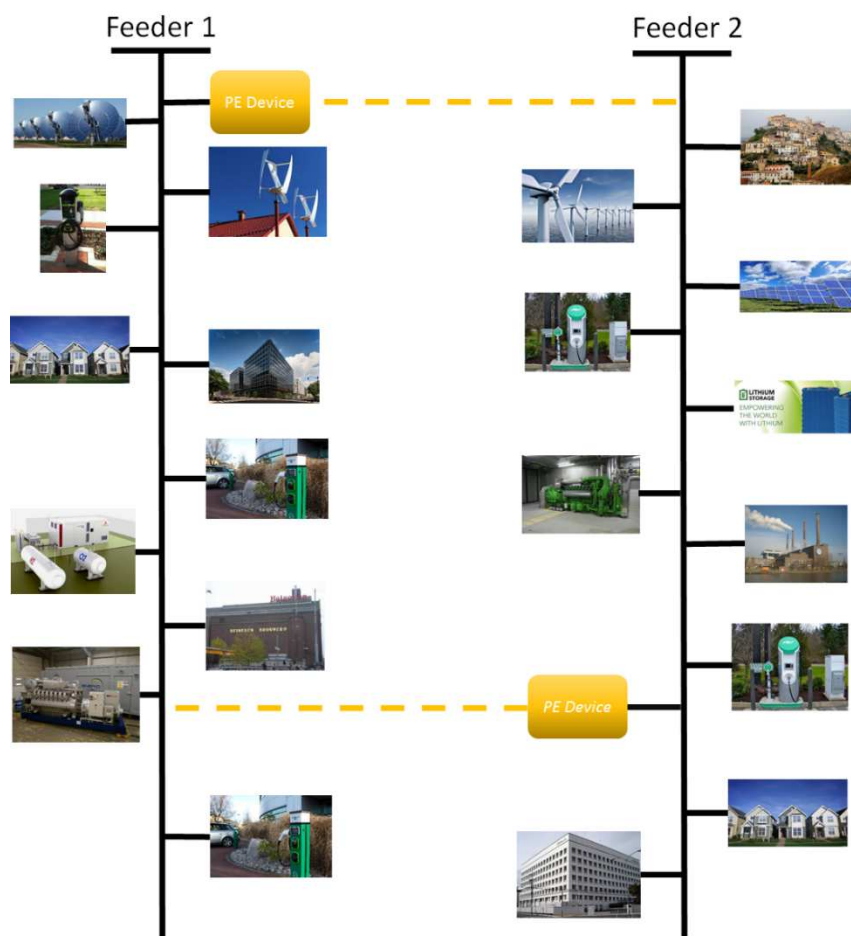
Figure 2.1 LV grids with two feeders interconnected with PE devices

In this work, to design new components to have a better control of LV grids and at the same time to reduce costs and dimensions for the proposed solutions, two aspects were considered. The first one is that the DC charging station is a distributed device installed along the feeder and the second one is that the UPFC or B2B converters (to connect two feeders in LV grids) can have a full control of active and reactive power flow in the interline link and in their PCCs. So, two new devices have been designed and tested: a DC charging station with an integrated UPFC and a DC charging station with an integrated B2B. These all-in-one solutions have different characteristics between them and they allow to have more control of LV grids with low costs. Furthermore, with the all-in-one solution is not necessary to install other devices in the LV grids and with the charging stations, it is possible to control the reactive/voltage profile in one feeder, to manage the bidirectional active power (between the grid and the storage device/car battery) and thanks to the interline link the power flow control between two feeders is easy and more reliable with power electronics converters than the electromechanical switches.

2.1 DC charging station with UPFC

The converter designed is composed of an AC/AC PWM converter with a bidirectional PWM battery charger to control the power between the EV and the AC grids [24]. This power electronics converter is connected between two feeders as shown in figure 2.2 and the interline link is an AC link without decoupling, so, the active and the reactive power flows between two electric feeders in the three-phase AC cable. The AC/AC solution used is the Unified Power Flow Controller (UPFC) [25] [26] where the STATCOM converter is used to manage the reactive power or the voltage level in the feeder 1 PCC and this converter assures the power balance for the DC link. Thus, the control system of this converter can control the DC link voltage, ensuring the right voltage values on the DC link capacitor. The Static Synchronous Series Converter (SSSC) is used to control (by a series transformer) the power flows between two feeders. It can emulate a virtual impedance to manage the active and reactive currents in the interline link [27].
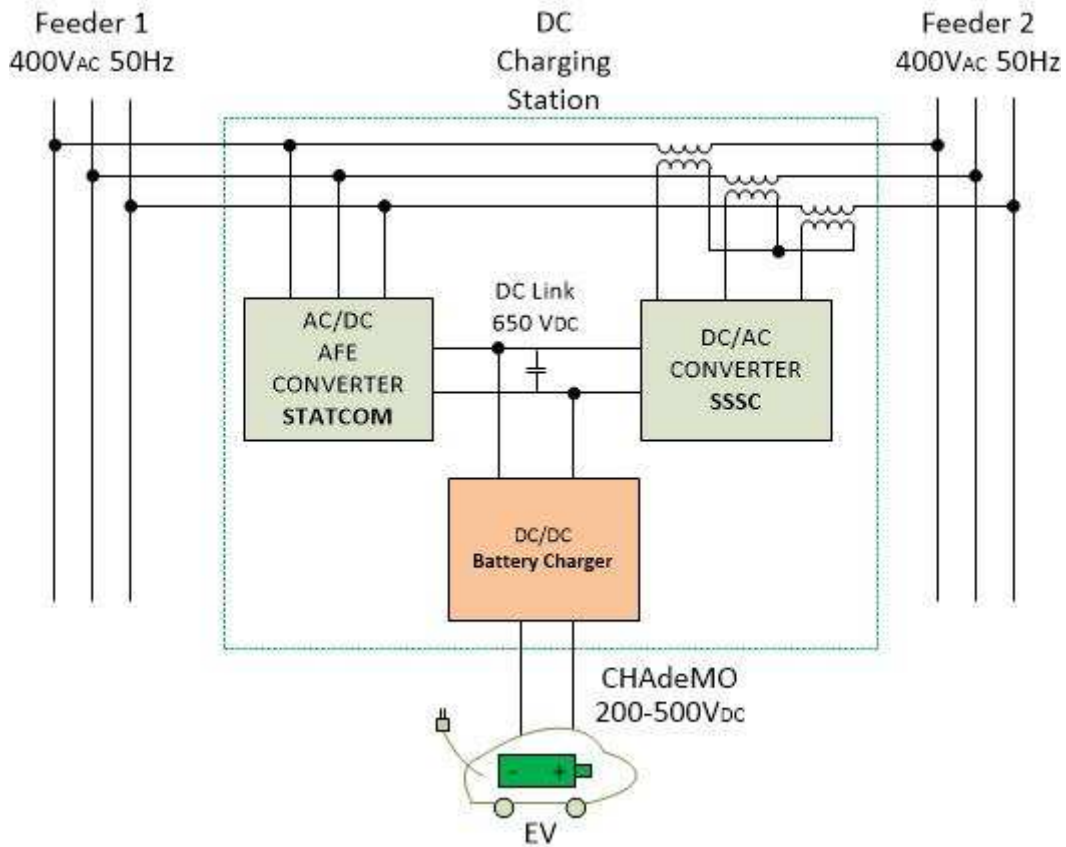
Figure 2.2: DC charging station with an integrated UPFC

The DC/DC converter is used like a battery charger, it is a bidirectional chopper, so, it is possible to control the battery current and the battery power in V2G (Vehicle to Grid) or G2V (Grid to Vehicle) mode. In figure 2.3 is shown the power scheme of the proposed solution, where the voltages and currents measurements signals are shown in orange lines. The STATCOM is designated with the letter ρ and the SSSC is designated with the letter σ. Furthermore, in the figure are shown the L filters used to interface the AC/DC converters to the grid to reduce the current harmonic content. For the EV is used a LC filter to reduce the current harmonic content and at the same time with the capacitor the voltage harmonic content is reduced to obtain a good power quality to charge or to discharge the EV battery.
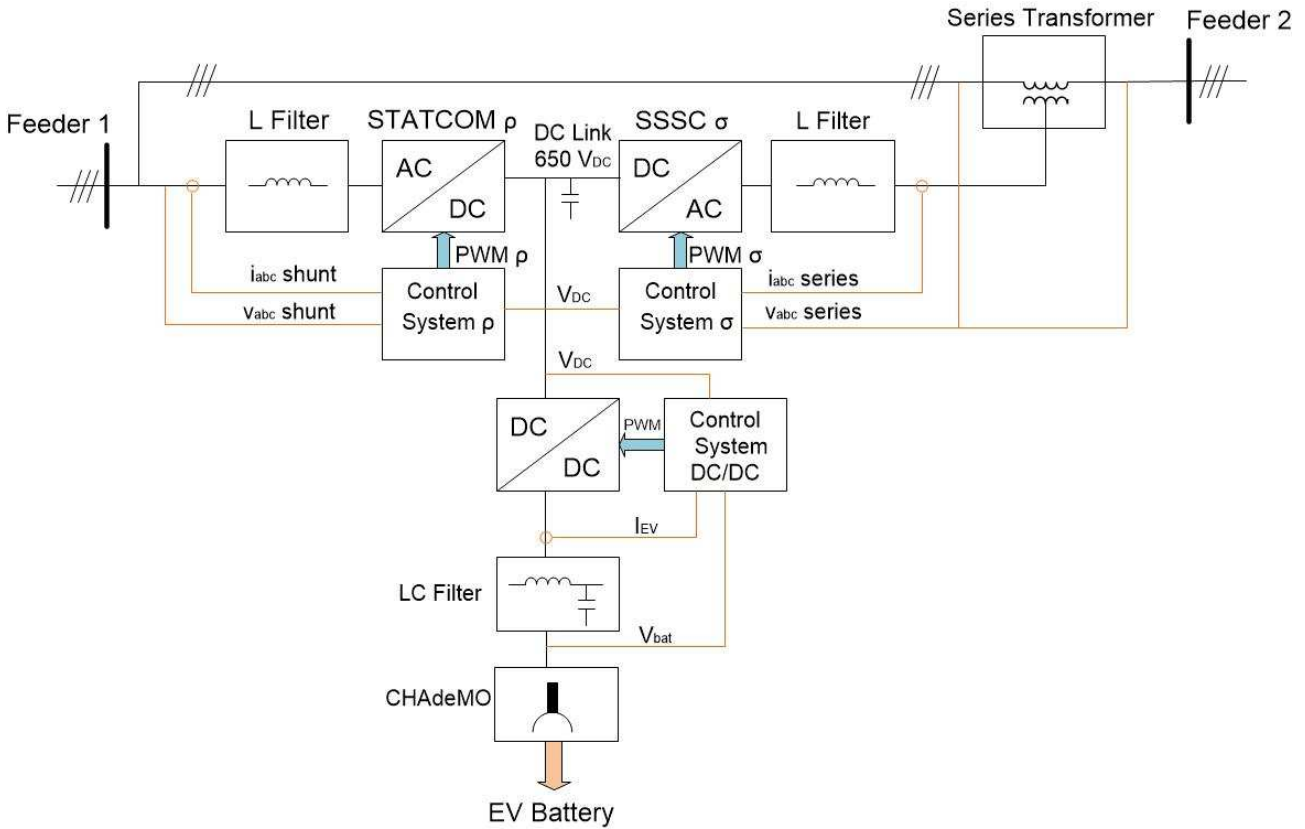
Figure 2.3: Power scheme of the DC charging station with an integrated UPFC

2.1.1 Plant for the STATCOM converter

For the STATCOM converter shown in figure 2.2 and connected to the feeder 1 with a L filter, the one phase equivalent scheme for the positive sequence is shown in figure 2.4. The power electronics converter is equivalent to the voltage source with the instantaneous voltage v_ρ equal to the average value of PWM voltage in one switching period. This voltage source is connected to the grid with a L filter with $R_{f\rho}$ equal to the ohmic component of the filter's impedance and $L_{f\rho}$ equal to the inductive component of the filter's impedance. The equivalent circuit is obtained using the Thevenin model applied in the PCC where e_1 is the no load voltage and L_{g1} and R_{g1} are the inductive and the ohmic component respectively of the grid impedance. The electric current exchanged between the power electronics converter and the grid is shown in the below figure as i_ρ.
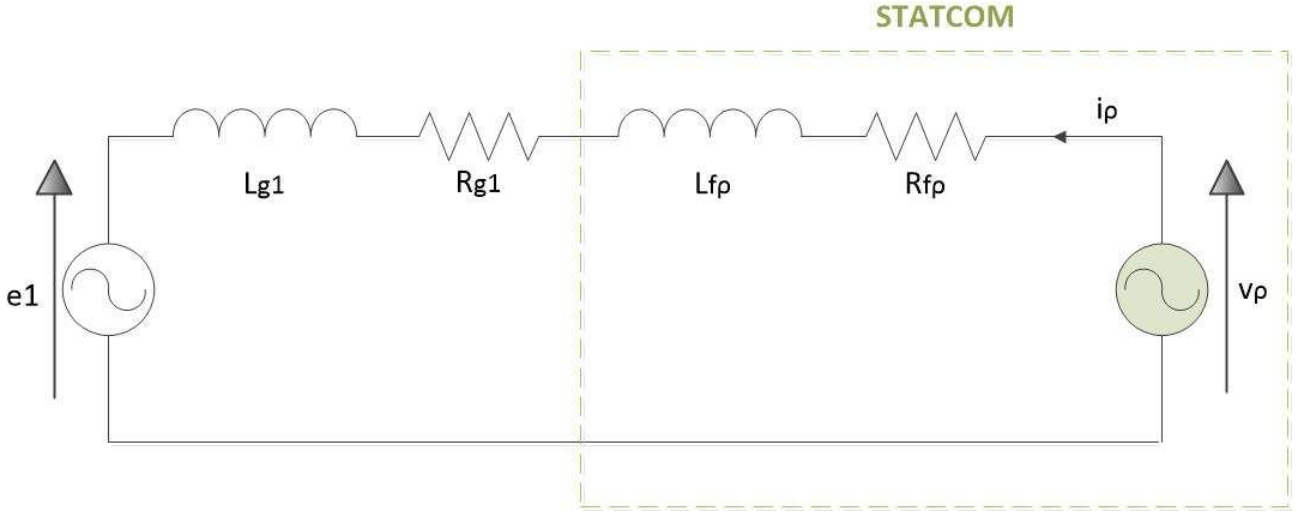
Figure 2.4: One phase representation for the STATCOM plant

Applying the Kirchhoff's voltage law to the circuit shown in figure 2.4, (1) is obtained where the converter voltage is equal to sum of three terms. The first one is the droop voltage due to the ohmic components, the second one is the droop voltage due to the inductive components and the last one is the grid voltage.

$$v_\rho = (R_{f\rho} + R_{g1})i_\rho + (L_{f\rho} + L_{g1})\frac{di_\rho}{dt} + e_1 \tag{1}$$

To consider the three-phase system, (2) shows the three-phase voltages and currents vectors. $\overrightarrow{V_{\rho_{abc}}}$ is the converter phase voltages' vector, $\overrightarrow{I_{\rho_{abc}}}$ is the converter line currents' vector and $\overrightarrow{E_{1_{abc}}}$ is the grid voltages' vector. So, with the equation (2), the vector equation (3) is obtained applying the Kirchhoff's voltage law to the three-phase circuit.

$$\overrightarrow{V_{\rho_{abc}}} = \begin{vmatrix} v_{\rho a} \\ v_{\rho b} \\ v_{\rho c} \end{vmatrix} \quad \overrightarrow{I_{\rho_{abc}}} = \begin{vmatrix} i_{\rho a} \\ i_{\rho b} \\ i_{\rho c} \end{vmatrix} \quad \overrightarrow{E_{1_{abc}}} = \begin{vmatrix} e_{1a} \\ e_{1b} \\ e_{1c} \end{vmatrix} \tag{2}$$

$$\overrightarrow{V_{\rho_{abc}}} = (R_{f\rho} + R_{g1})\overrightarrow{I_{\rho_{abc}}} + (L_{f\rho} + L_{g1})\frac{d\overrightarrow{I_{\rho_{abc}}}}{dt} + \overrightarrow{E_{1_{abc}}} \tag{3}$$

To reduce the number of equations in (3) the Clark transformation is used. In the equations system (4) are shown three generic sinusoidal waveforms with the initial phase equal to ψ. So, the rotating vector in the alpha-beta static frame is obtained thanks to (5). In (6) is shown the operator δ that it allows the alfa-beta transformation. The direct Clark transformation is shown in (7) and the inverse Clark transformation is shown in (8).

$$
\begin{aligned}
x_a &= \widehat{X}\sin(\omega t + \psi) \\
x_b &= \widehat{X}\sin(\omega t + \psi - 120°) \\
x_c &= \widehat{X}\sin(\omega t + \psi - 240°)
\end{aligned}
\tag{4}
$$

$$
\overline{x_{\alpha\beta}} = \frac{2}{3}(x_a + \delta x_b + \delta^2 x_c)
\tag{5}
$$

$$
\delta = e^{j\frac{2}{3}\pi}
\tag{6}
$$

$$
\begin{pmatrix} x_\alpha \\ x_\beta \end{pmatrix} =
\begin{pmatrix} \frac{2}{3} & -\frac{1}{3} & -\frac{1}{3} \\ 0 & \frac{\sqrt{3}}{3} & -\frac{\sqrt{3}}{3} \end{pmatrix}
\begin{pmatrix} x_a \\ x_b \\ x_c \end{pmatrix}
\tag{7}
$$

$$
\begin{pmatrix} x_a \\ x_b \\ x_c \end{pmatrix} =
\begin{pmatrix} 1 & 0 \\ -\frac{1}{2} & \frac{\sqrt{3}}{2} \\ -\frac{1}{2} & -\frac{\sqrt{3}}{2} \end{pmatrix}
\begin{pmatrix} x_\alpha \\ x_\beta \end{pmatrix}
\tag{8}
$$

In figure 2.5 is shown the alpha-beta static frame and the d-q rotating frame. The generic vector $\overline{X}_{\alpha\beta}$ rotates with an angular speed equal to ω and it is calculated by (5). The components on alpha and beta axis are sinusoidal waves, instead, in the d-q rotating frame, the vector components depend on from the frame angular speed. If the d-q frame angular speed is equal to the vector $\overline{X}_{\alpha\beta}$ angular speed (as shown in the figure), the rotating frame is synchronous and the $\overline{X}_{\alpha\beta}$ angular speed in the d-q frame is equal to zero at steady state, thus, the d-q components are constant at steady state. To calculate the angle θ is used the Phase Locked Loop (PLL), that it will be explained in the next chapter.
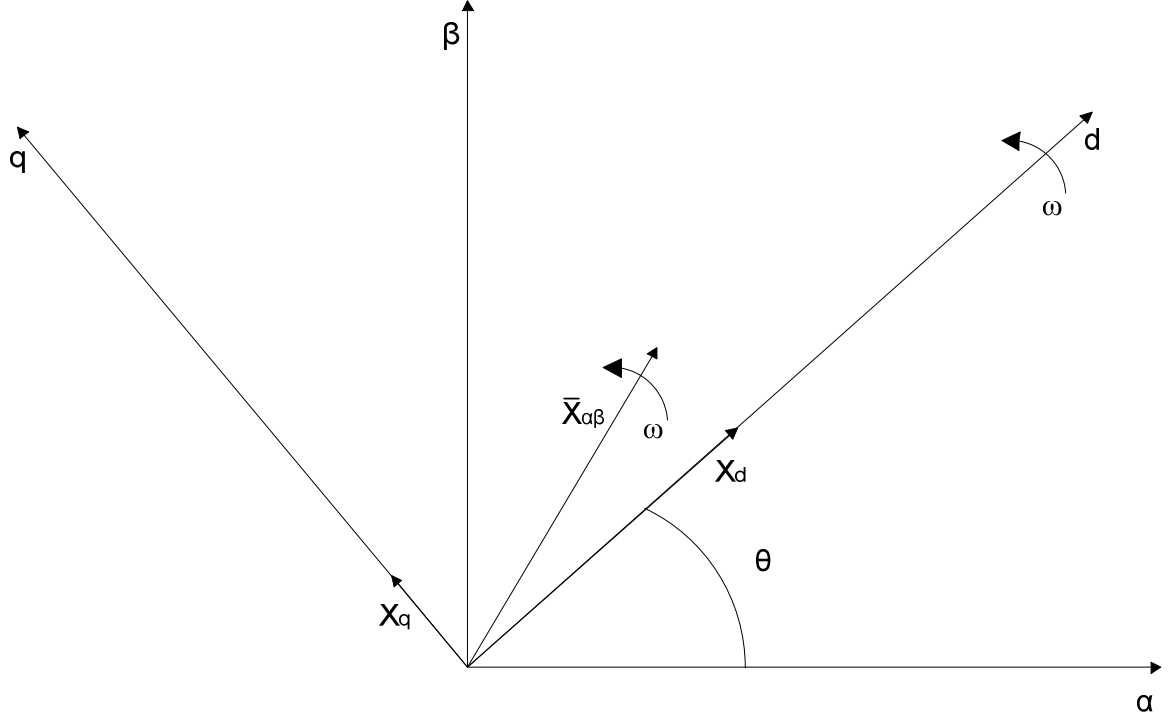
Figure 2.5: alpha-beta static frame and d-q rotating frame

With (9) it is possible to obtain d-q components from alpha-beta components and vice versa. The direct transformation to calculate d-q components is shown in (10), instead the inverse transformation to calculate alpha-beta components is shown in (11).

$$\overline{x_{dq}} = \overline{x_{\alpha\beta}}e^{-j\theta} \tag{9}$$

$$\begin{pmatrix} x_d \\ x_q \end{pmatrix} = \begin{pmatrix} \cos\theta & \sin\theta \\ -\sin\theta & \cos\theta \end{pmatrix}\begin{pmatrix} x_\alpha \\ x_\beta \end{pmatrix} \tag{10}$$

$$\begin{pmatrix} x_\alpha \\ x_\beta \end{pmatrix} = \begin{pmatrix} \cos\theta & -\sin\theta \\ \sin\theta & \cos\theta \end{pmatrix}\begin{pmatrix} x_d \\ x_q \end{pmatrix} \tag{11}$$

With the equation (10) it is possible to obtain the converter phase voltages' vector $\overrightarrow{V_{\rho_{dq}}}$ in d-q reference frame, the phase currents' vector $\overrightarrow{I_{\rho_{dq}}}$ in d-q frame and finally the grid voltages' vector $\overrightarrow{E_{1_{dq}}}$ in d-q frame as shown in (12).

$$\vec{V_\rho}_{dq} = \begin{vmatrix} v_{\rho d} \\ v_{\rho q} \end{vmatrix} \quad \vec{I_\rho}_{dq} = \begin{vmatrix} i_{\rho d} \\ i_{\rho q} \end{vmatrix} \quad \vec{E1}_{dq} = \begin{vmatrix} e_{1d} \\ e_{1q} \end{vmatrix} \tag{12}$$

Applying the d-q transformation in (3), (14) is obtained, where R_ρ and L_ρ are calculated by (13) to simplify the equation.

$$R_\rho = R_{f\rho} + R_{g1} \qquad L_\rho = L_{f\rho} + L_{g1} \tag{13}$$

$$\vec{V_\rho}_{dq} = R_\rho \vec{I_\rho}_{dq} + L_\rho \frac{d\vec{I_\rho}_{dq}}{dt} + j\omega_{dq\rho} L_\rho \vec{I_\rho}_{dq} + \vec{E1}_{dq} \tag{14}$$

The direct and quadrature components are shown in (15).

$$
\begin{aligned}
v_{\rho d} &= R_\rho i_{\rho d} + L_\rho \frac{di_{\rho d}}{dt} - \omega_{dq\rho} L_\rho i_{\rho q} + e_{1d} \\
v_{\rho q} &= R_\rho i_{\rho q} + L_\rho \frac{di_{\rho q}}{dt} + \omega_{dq\rho} L_\rho i_{\rho d} + e_{1q}
\end{aligned}
\tag{15}
$$

To design the control system for the STATCOM converter is necessary to obtain the plant with the mathematical formulation, so, to use the linear representation, is used the Laplace transformation. In this way, the equations in s-domain for the STATCOM plant in d-q rotating frame are shown in (16) with the initial conditions equal to zero. In figure 2.6 the schematic representation for the plant is shown, where the outputs are the currents, the inputs are the grid voltages and the converter voltages, furthermore, there are the coupling terms for both axis.

$$
\begin{aligned}
I_{\rho d}(s) &= \frac{1}{L_\rho s + R_\rho}(V_{\rho d}(s) + \omega_{dq\rho} L_\rho I_{\rho q}(s) - E_{1d}(s)) \\
I_{\rho q}(s) &= \frac{1}{L_\rho s + R_\rho}(V_{\rho q}(s) - \omega_{dq\rho} L_\rho I_{\rho d}(s) - E_{1q}(s))
\end{aligned}
\tag{16}
$$

$$E_{1d}(s)$$

$$V_{\rho d}(s) \quad \boxed{\dfrac{1}{L_\rho s + R_\rho}} \quad I_{\rho d}(s)$$

$$\omega_{d\varphi} L_\rho I_{\rho q}(s)$$

$$E_{1q}(s)$$

$$V_{\rho q}(s) \quad \boxed{\dfrac{1}{L_\rho s + R_\rho}} \quad I_{\rho q}(s)$$

$$\omega_{d\varphi} L_\rho I_{\rho d}(s)$$
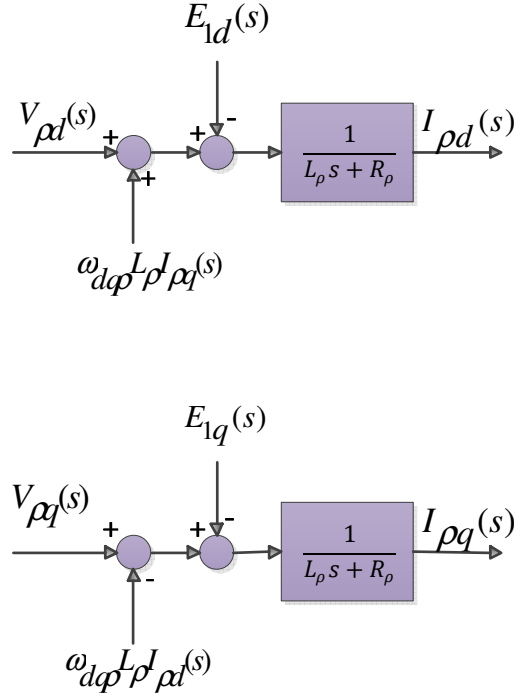
Figure 2.6: d-q plant in s-domain for the STATCOM converter

2.1.2 Plant for the SSSC converter

For the SSSC converter shown in figure 2.2 and connected between the feeder 1 and the feeder 2 with a L filter and with a series transformer, the one phase equivalent scheme for the positive sequence is shown in figure 2.7. The power electronics converter is equivalent to the voltage source with the instantaneous voltage v_σ equal to the average value of PWM voltage in one switching period. This voltage source is connected to the series transformer with a L filter with R_σ equal to the ohmic component of the filter's impedance and L_σ equal to the inductive component of the filter's impedance. In the equivalent circuit v_1 is the voltage in the PCC of the feeder 1 and v_2 is the voltage in the PCC of the feeder 2. The interline current i_σ between two feeders is shown in the figure.
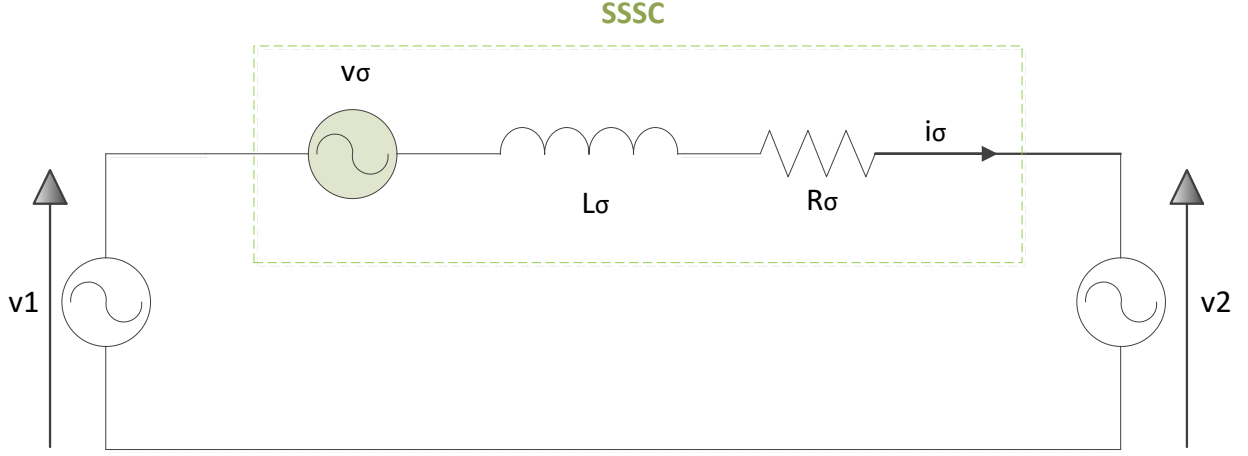
Figure 2.7: One phase representation for the SSSC plant

Applying the Kirchhoff's voltage law to the circuit shown in figure 2.7, (17) is obtained where the converter voltage v_σ is equal to sum of four terms. The first one is the droop voltage due to the ohmic component, the second one is the droop voltage due to the inductive component and the last two are the phase voltage of two feeders.

$$v_\sigma = R_\sigma i_\sigma + L_\sigma \frac{di_\sigma}{dt} + v_2 - v_1 \tag{17}$$

To consider the three-phase system, (18) shows the three-phase voltages and currents vectors. $\overrightarrow{V_{\sigma abc}}$ is the converter phase voltages' vector, $\overrightarrow{I_{\sigma abc}}$ is the interline currents' vector, $\overrightarrow{V_{1 abc}}$ is the PCC 1 phase voltage's vector and $\overrightarrow{V_{2 abc}}$ is the PCC 2 phase voltage's vector. So, thanks to (18), the vector equation (19) is obtained applying the Kirchhoff's voltage law to the circuit shown in figure 2.7.

$$\overrightarrow{V_{\sigma abc}} = \begin{vmatrix} v_{\sigma a} \\ v_{\sigma b} \\ v_{\sigma c} \end{vmatrix} \quad \overrightarrow{I_{\sigma abc}} = \begin{vmatrix} i_{\sigma a} \\ i_{\sigma b} \\ i_{\sigma c} \end{vmatrix} \quad \overrightarrow{V_{1 abc}} = \begin{vmatrix} v_{1 a} \\ v_{1 b} \\ v_{1 c} \end{vmatrix} \quad \overrightarrow{V_{2 abc}} = \begin{vmatrix} v_{2 a} \\ v_{2 b} \\ v_{2 c} \end{vmatrix} \tag{18}$$

$$\overrightarrow{V_{\sigma abc}} = R_\sigma \overrightarrow{I_{\sigma abc}} + L_\sigma \frac{d \overrightarrow{I_{\sigma abc}}}{dt} + \overrightarrow{V_{2 abc}} - \overrightarrow{V_{1 abc}} \tag{19}$$

Thanks to (10) it is possible to obtain the converter phase voltages' vector $\overrightarrow{V_{\sigma\,dq}}$ in d-q reference frame, the phase currents' vector $\overrightarrow{I_{\sigma\,dq}}$ in d-q frame and finally the feeders voltages' vectors $\overrightarrow{V_{1\,dq}}$ and $\overrightarrow{V_{2\,dq}}$ in d-q rotating synchronous frame.

$$\overrightarrow{V_{\sigma\,dq}} = \begin{vmatrix} v_{\sigma d} \\ v_{\sigma q} \end{vmatrix} \quad \overrightarrow{I_{\sigma\,dq}} = \begin{vmatrix} i_{\sigma d} \\ i_{\sigma q} \end{vmatrix} \quad \overrightarrow{V_{1\,dq}} = \begin{vmatrix} v_{1d} \\ v_{1q} \end{vmatrix} \quad \overrightarrow{V_{2\,dq}} = \begin{vmatrix} v_{2d} \\ v_{2q} \end{vmatrix} \tag{20}$$

Applying the d-q transformation in (19), (21) is obtained to have a mathematical model of the plant for the SSSC converter.

$$\overrightarrow{V_{\sigma\,dq}} = R_\sigma \overrightarrow{I_{\sigma\,dq}} + L_\sigma \frac{d\,\overrightarrow{I_{\sigma\,dq}}}{dt} + j\omega_{dq\rho} L_\sigma \overrightarrow{I_{\sigma\,dq}} + \overrightarrow{V_{2\,dq}} - \overrightarrow{V_{1\,dq}} \tag{21}$$

The direct and quadrature components are shown in (22).

$$\begin{aligned} v_{\sigma d} &= R_\sigma i_{\sigma d} + L_\sigma \frac{di_{\sigma d}}{dt} - \omega_{dq\rho} L_\sigma i_{\sigma q} + v_{2d} - v_{1d} \\ v_{\sigma q} &= R_\sigma i_{\sigma q} + L_\sigma \frac{di_{\sigma q}}{dt} + \omega_{dq\rho} L_\sigma i_{\sigma d} + v_{2q} - v_{1q} \end{aligned} \tag{22}$$

To design the control system for the SSSC converter is necessary to obtain the plant with the mathematical formulation, so, to use the linear representation, is used the Laplace transformation. In this way, the equations in s-domain for the SSSC plant in d-q rotating frame are shown in (23). In figure 2.8 the schematic representation for the plant is shown, where the outputs are the currents, the inputs are the feeders voltages and the converter voltages, furthermore, there are the coupling terms for both axis.

$$\begin{aligned} I_{\sigma d}(s) &= \frac{1}{L_\sigma s + R_\sigma} \left(V_{\sigma d}(s) + \omega_{dq\rho} L_\sigma I_{\sigma q}(s) - (V_{2d}(s) - V_{1d}(s)) \right) \\ I_{\sigma q}(s) &= \frac{1}{L_\sigma s + R_\sigma} \left(V_{\sigma q}(s) - \omega_{dq\rho} L_\sigma I_{\sigma d}(s) - (V_{2q}(s) - V_{1q}(s)) \right) \end{aligned} \tag{23}$$
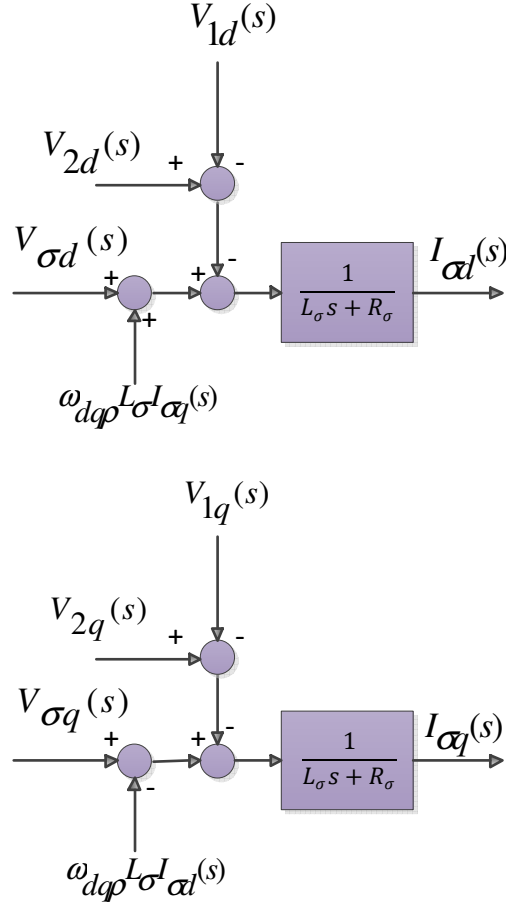
Figure 2.8: d-q plant in s-domain for the SSSC converter

2.2 DC charging station with B2B

The DC charging station with B2B is made up of two inverters in the back to back configuration [28] [29]. One of two converters is called "pilot" and the other one is called "co-pilot". The pilot converter is able to exchange the active power between two feeders and it independently is able to manage reactive power in the PCC, instead the co-pilot converter assures the active power balance in the DC link. The device designed is similar to the DC charging station with UPFC, but the interline link is different because it is not in AC. In fact, thanks to the two conversion systems, the link between the two feeders is a DC type with a nominal value equal to 650 V_{DC}. Thus, the entire active power (exchanged between two electrical grids) flows through both conversion systems, so, the nominal apparent power is equal for both converters. This configuration is more expensive than

the UPFC solution, but it is more flexible; it is possible to use one of two converters to charge the

EV at nominal power in case the failure on one of two feeders.
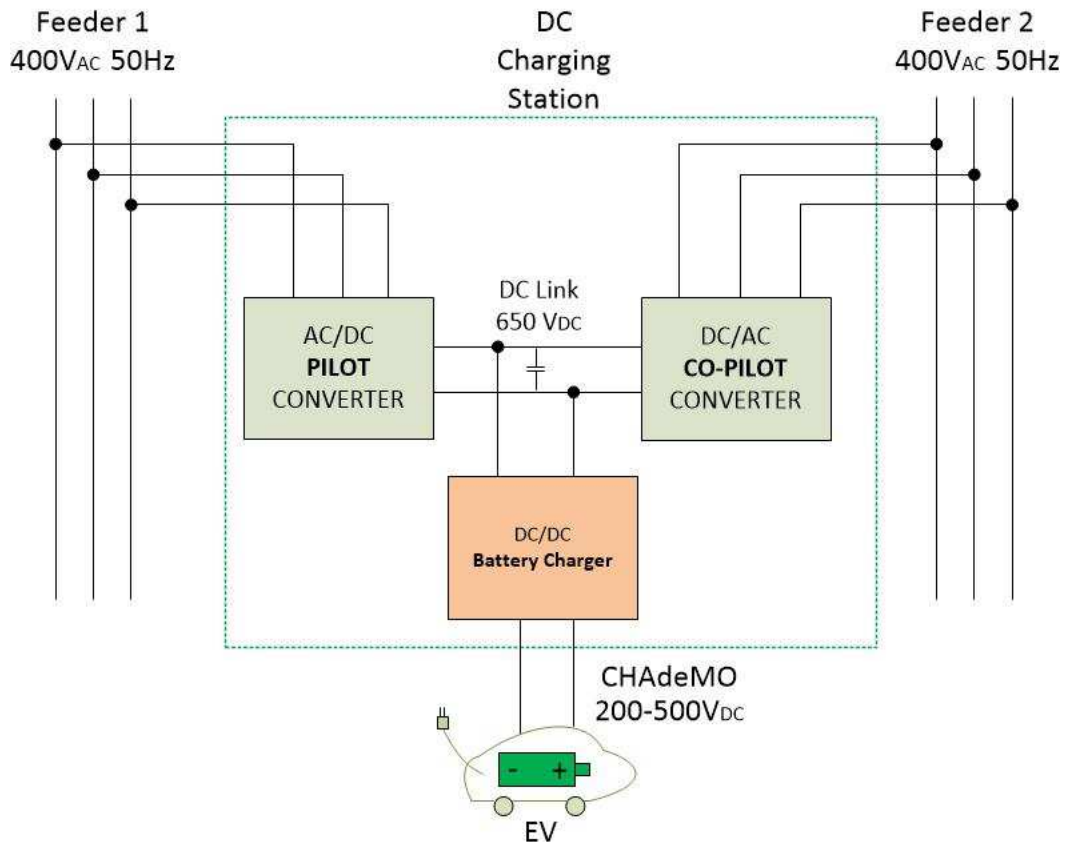
Figure 2.9: DC charging station with an integrated B2B

In figure 2.10 is shown the power scheme of the proposed solution, where the voltages and currents

measurements signals are shown in orange lines. The pilot converter is designated with the letter δ

and the co-pilot converter is designated with the letter ε. Furthermore, in the figure are shown the

LCL filters used to interface the AC/DC converters to the grid to reduce the current harmonic

content. For the EV is used a LC filter to reduce the current harmonic content and at the same time,

with the capacitor the voltage harmonic content is reduced to obtain a good power quality to charge

or to discharge the EV battery.
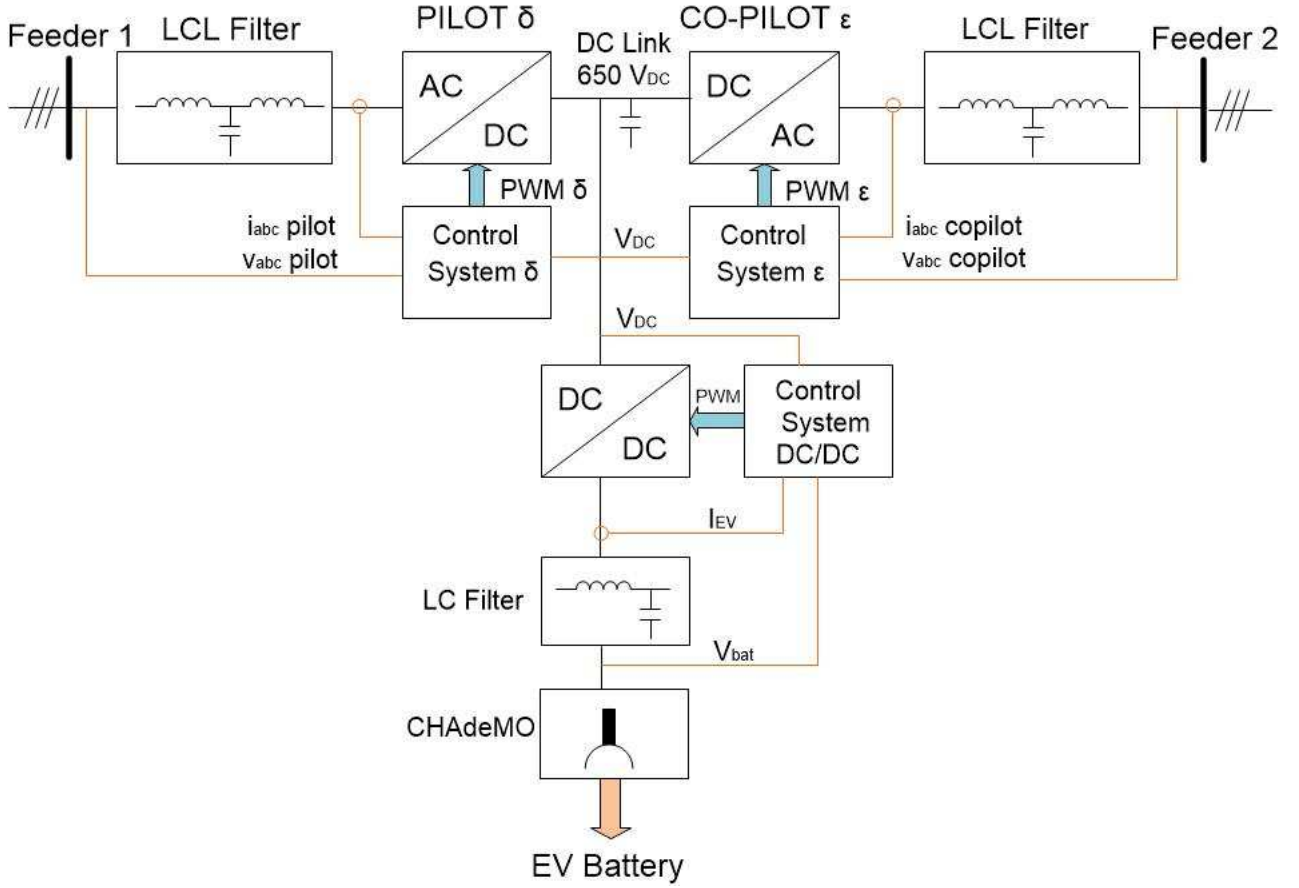
Figure 2.10: Power scheme of the DC charging station with an integrated B2B

2.2.1 Plant for the pilot converter

For the pilot converter shown in figure 2.9 and connected to the feeder 1 with a LCL filter, the one phase equivalent scheme for the positive sequence is shown in figure 2.11. The filter's capacitor is neglected to examine the circuit at the fundamental frequency. The power electronics converter is equivalent to the voltage source with the instantaneous voltage v_δ equal to the average value of PWM voltage in one switching period. This voltage source is connected to the grid with $R_{f\delta}$ equal to the ohmic component of the filter's impedance and $L_{f\delta}$ equal to the inductive component of the filter's impedance. The equivalent circuit is obtained thanks to the Thevenin model applied in the PCC where e_1 is the no load grid voltage and L_{g1} and R_{g1} are the inductive and the ohmic component respectively of the grid impedance. The electric current exchanged between the power electronics converter and the grid is shown in the below figure as i_δ.
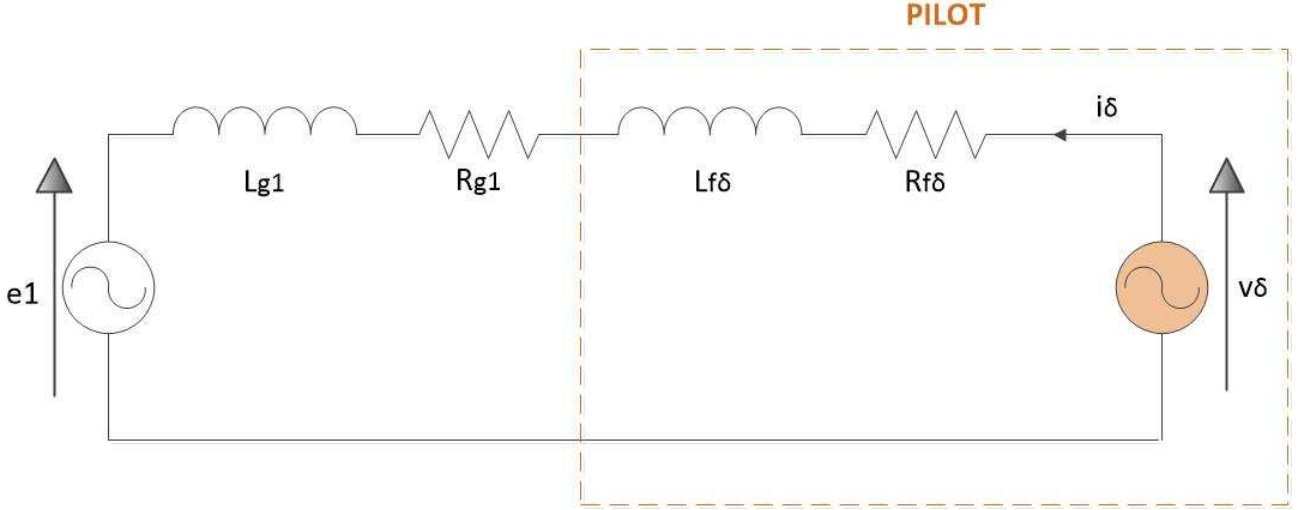
PILOT

Figure 2.11: One phase representation for the pilot converter plant

Applying the Kirchhoff's voltage law to the circuit shown in figure 2.11, (24) is obtained, where the converter voltage is equal to sum of three terms. The first one is the droop voltage due to the ohmic components, the second one is the droop voltage due to the inductive components and the last one is the grid voltage of the feeder 1.

$$v_\delta = \left(R_{f\delta} + R_{g1}\right)i_\delta + \left(L_{f\delta} + L_{g1}\right)\frac{di_\delta}{dt} + e_1 \qquad (24)$$

To consider the three-phase system, (25) shows the three-phase voltages and currents vectors. $\overrightarrow{V_{\delta\,abc}}$ is the converter phase voltages' vector, $\overrightarrow{I_{\delta\,abc}}$ is the converter line currents' vector and $\overrightarrow{E_{1\,abc}}$ is the grid voltages' vector. So, the vector equation (26) is obtained applying the Kirchhoff's voltage law to the three-phase circuit.

$$\overrightarrow{V_{\delta\,abc}} = \begin{vmatrix} v_{\delta a} \\ v_{\delta b} \\ v_{\delta c} \end{vmatrix} \quad \overrightarrow{I_{\delta\,abc}} = \begin{vmatrix} i_{\delta a} \\ i_{\delta b} \\ i_{\delta c} \end{vmatrix} \quad \overrightarrow{E_{1\,abc}} = \begin{vmatrix} e_{1a} \\ e_{1b} \\ e_{1c} \end{vmatrix} \qquad (25)$$

$$\overrightarrow{V_{\delta\,abc}} = \left(R_{f\delta} + R_{g1}\right)\overrightarrow{I_{\delta\,abc}} + \left(L_{f\delta} + L_{g1}\right)\frac{d\overrightarrow{I_{\delta\,abc}}}{dt} + \overrightarrow{E_{1\,abc}} \qquad (26)$$

With the equation (10) it is possible to obtain the converter phase voltages' vector $\overrightarrow{V_{\delta_{dq}}}$ in d-q reference frame, the phase currents' vector $\overrightarrow{I_{\delta_{dq}}}$ in d-q frame and finally the grid voltages' vector $\overrightarrow{E_{1_{dq}}}$ in d-q rotating synchronous frame.

$$\overrightarrow{V_{\delta_{dq}}} = \begin{vmatrix} v_{\delta d} \\ v_{\delta q} \end{vmatrix} \quad \overrightarrow{I_{\delta_{dq}}} = \begin{vmatrix} i_{\delta d} \\ i_{\delta q} \end{vmatrix} \quad \overrightarrow{E_{1_{dq}}} = \begin{vmatrix} e_{1d} \\ e_{1q} \end{vmatrix} \tag{27}$$

Applying the d-q transformation in (26), (29) is obtained, where R_δ and L_δ are calculated by (28) to simplify the equation.

$$R_\delta = R_{f\delta} + R_{g1} \qquad L_\delta = L_{f\delta} + L_{g1} \tag{28}$$

$$\overrightarrow{V_{\delta_{dq}}} = R_\delta \overrightarrow{I_{\delta_{dq}}} + L_\delta \frac{d\overrightarrow{I_{\delta_{dq}}}}{dt} + j\omega_{dq\delta} L_\delta \overrightarrow{I_{\delta_{dq}}} + \overrightarrow{E_{1_{dq}}} \tag{29}$$

The direct and quadrature components of the equation (29) are shown in (30).

$$
\begin{aligned}
v_{\delta d} &= R_\delta i_{\delta d} + L_\delta \frac{di_{\delta d}}{dt} - \omega_{dq\delta} L_\delta i_{\delta q} + e_{1d} \\
v_{\delta q} &= R_\delta i_{\delta q} + L_\delta \frac{di_{\delta q}}{dt} + \omega_{dq\delta} L_\delta i_{\delta d} + e_{1q}
\end{aligned}
\tag{30}
$$

To design the control system for the pilot converter is necessary to obtain the plant with the mathematical formulation, so, to use the linear representation, is used the Laplace transformation. In this way, the equations in s-domain for the pilot converter plant in d-q rotating frame are shown in (31). In figure 2.12 the schematic representation for the plant is shown, where the outputs are the currents and the inputs are the grid voltages and the converter voltages, furthermore, there are the coupling terms for both axis.

$$I_{\delta d}(s) = \frac{1}{L_\delta s + R_\delta}(V_{\delta d}(s) + \omega_{dq\delta}L_\delta I_{\delta q}(s) - E_{1d}(s))$$

$$I_{\delta q}(s) = \frac{1}{L_\delta s + R_\delta}(V_{\delta q}(s) - \omega_{dq\delta}L_\delta I_{\delta d}(s) - E_{1q}(s))$$

(31)
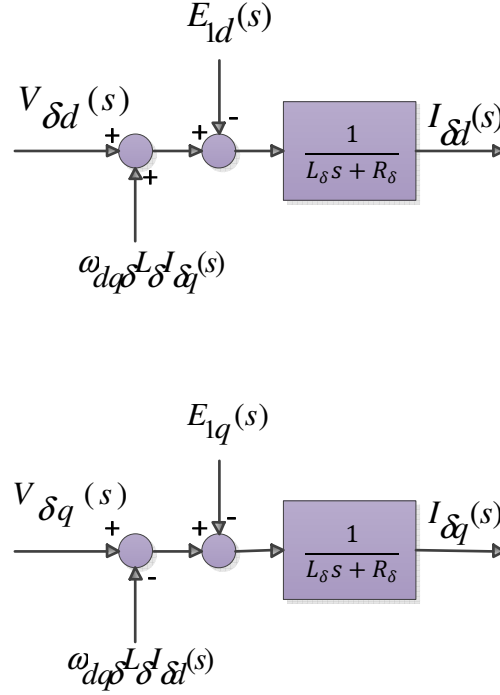

Figure 2.12: d-q plant in s-domain for the pilot converter

2.2.2 Plant for the co-pilot converter

For the co-pilot converter shown in figure 2.9 and connected to the feeder 2 with a LCL filter, the one phase equivalent scheme for the positive sequence is shown in figure 2.13. The filter's capacitor is neglected to examine the circuit at the fundamental frequency. The power electronics converter is equivalent to the voltage source with the instantaneous voltage v_ε equal to the average value of PWM voltage in one switching period. This voltage source is connected to the grid with $R_{f\varepsilon}$ equal to the ohmic component of the filter's impedance and $L_{f\varepsilon}$ equal to the inductive component of the filter's impedance. The equivalent circuit is obtained using the Thevenin model applied in the PCC where e_2 is the no load grid voltage and L_{g2} and R_{g2} are the inductive and the ohmic

component respectively of the grid impedance. The electric current exchanged between the power electronics converter and the grid is shown in the below figure as i_ε.
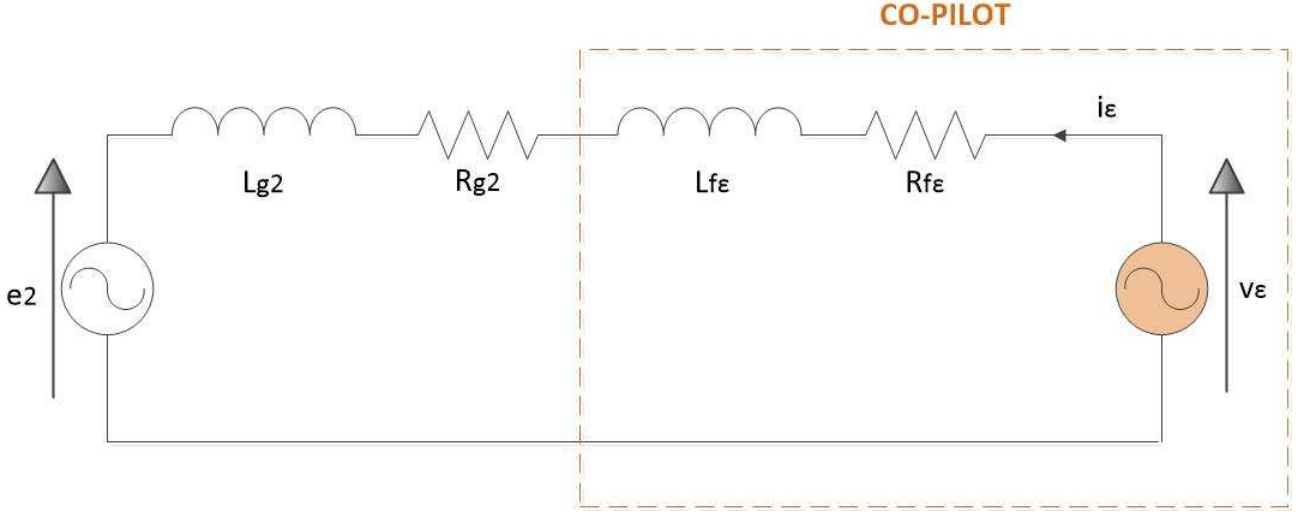
Figure 2.13: One phase representation for the co-pilot converter plant

Applying the Kirchhoff's voltage law to the circuit shown in figure 2.13, (32) is obtained, where the converter voltage is equal to sum of three terms. The first one is the droop voltage due to the ohmic components, the second one is the droop voltage due to the inductive components and the last one is the grid voltage of the feeder 2.

$$v_\varepsilon = \left(R_{f\varepsilon} + R_{g2}\right)i_\varepsilon + \left(L_{f\varepsilon} + L_{g2}\right)\frac{di_\varepsilon}{dt} + e_2 \tag{32}$$

To consider the three-phase system, (33) shows the three-phase voltages and currents vectors. $\overrightarrow{V_\varepsilon}_{abc}$ is the converter phase voltages' vector, $\overrightarrow{I_\varepsilon}_{abc}$ is the converter line currents' vector and $\overrightarrow{E_2}_{abc}$ is the grid voltages' vector. So, thanks to (33), the vector equation (34) is obtained applying the Kirchhoff's voltage law to the three-phase circuit.

$$\overrightarrow{V_\varepsilon}_{abc} = \begin{vmatrix} v_{\varepsilon a} \\ v_{\varepsilon b} \\ v_{\varepsilon c} \end{vmatrix} \quad \overrightarrow{I_\varepsilon}_{abc} = \begin{vmatrix} i_{\varepsilon a} \\ i_{\varepsilon b} \\ i_{\varepsilon c} \end{vmatrix} \quad \overrightarrow{E_2}_{abc} = \begin{vmatrix} e_{2a} \\ e_{2b} \\ e_{2c} \end{vmatrix} \tag{33}$$

$$\overrightarrow{V_{\varepsilon\,abc}} = \left(R_{f\varepsilon} + R_{g2}\right)\overrightarrow{I_{\varepsilon\,abc}} + \left(L_{f\varepsilon} + L_{g2}\right)\frac{d\overrightarrow{I_{\varepsilon\,abc}}}{dt} + \overrightarrow{E_{2\,abc}} \tag{34}$$

Using the equation (10) it is possible to obtain the converter phase voltages' vector $\overrightarrow{V_{\varepsilon_{dq}}}$ in d-q reference frame, the phase currents' vector $\overrightarrow{I_{\varepsilon_{dq}}}$ in d-q frame and finally the grid voltages' vector $\overrightarrow{E_{2_{dq}}}$ in d-q rotating synchronous frame.

$$\overrightarrow{V_{\varepsilon_{dq}}} = \begin{vmatrix} v_{\varepsilon d} \\ v_{\varepsilon q} \end{vmatrix} \quad \overrightarrow{I_{\varepsilon_{dq}}} = \begin{vmatrix} i_{\varepsilon d} \\ i_{\varepsilon q} \end{vmatrix} \quad \overrightarrow{E_{2_{dq}}} = \begin{vmatrix} e_{2d} \\ e_{2q} \end{vmatrix} \tag{35}$$

Applying the d-q transformation in (34), (37) is obtained, where R_ε and L_ε are calculated by (36) to simplify the equation.

$$R_\varepsilon = R_{f\varepsilon} + R_{g2} \qquad L_\varepsilon = L_{f\varepsilon} + L_{g2} \tag{36}$$

$$\overrightarrow{V_{\varepsilon_{dq}}} = R_\varepsilon \overrightarrow{I_{\varepsilon_{dq}}} + L_\varepsilon \frac{d\overrightarrow{I_{\varepsilon_{dq}}}}{dt} + j\omega_{dq\varepsilon}L_\varepsilon \overrightarrow{I_{\varepsilon_{dq}}} + \overrightarrow{E_{2_{dq}}} \tag{37}$$

The direct and quadrature components of the equation (37) are shown in (38).

$$\begin{aligned} v_{\varepsilon d} &= R_\varepsilon i_{\varepsilon d} + L_\varepsilon \frac{di_{\varepsilon d}}{dt} - \omega_{dq\varepsilon}L_\varepsilon i_{\varepsilon q} + e_{2d} \\ v_{\varepsilon q} &= R_\varepsilon i_{\varepsilon q} + L_\varepsilon \frac{di_{\varepsilon q}}{dt} + \omega_{dq\varepsilon}L_\varepsilon i_{\varepsilon d} + e_{2q} \end{aligned} \tag{38}$$

To design the control system for the co-pilot converter is necessary to obtain the plant with the mathematical formulation, so, to use the linear representation, is used the Laplace transformation. In this way, the equations in s-domain for the co-pilot converter plant in d-q rotating frame are shown in (39). In figure 2.14 the schematic representation for the plant is shown, where the outputs are the currents, the inputs are the grid voltages and the converter voltages, furthermore, there are the coupling terms for both axis.

$$I_{\varepsilon d}(s) = \frac{1}{L_\varepsilon s + R_\varepsilon}(V_{\varepsilon d}(s) + \omega_{dq\varepsilon}L_\varepsilon I_{\varepsilon q}(s) - E_{2d}(s))$$

$$I_{\varepsilon q}(s) = \frac{1}{L_\varepsilon s + R_\varepsilon}(V_{\varepsilon q}(s) - \omega_{dq\varepsilon}L_\varepsilon I_{\varepsilon d}(s) - E_{2q}(s))$$

(39)
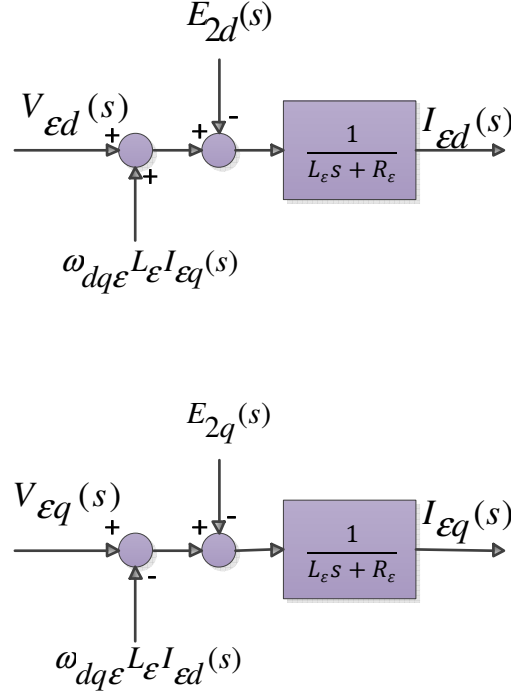
Figure 2.14: d-q plant in s-domain for the co-pilot converter

2.3 Plant for the DC/DC converter

In figure 2.15, the equivalent circuit for the DC/DC converter is shown, where the electric car battery is represented by Thevenin model. E_{bat} is equal to no load condition voltage and R_{bat} is the equivalent resistance to represent the power losses in the battery and in the connection cables between the EV and the DC charging station. The DC/DC power converter is schematised with a DC voltage source with an ohmic-inductive-capacitive impedance for the converter filter, where L_f is the inductive component of the filter, R_f is the ohmic component of the filter and C_f is the filter capacitor. V_{EV} is the DC/DC average voltage output applied to the LC filter and it is obtained thanks to the DC/DC power control.

49
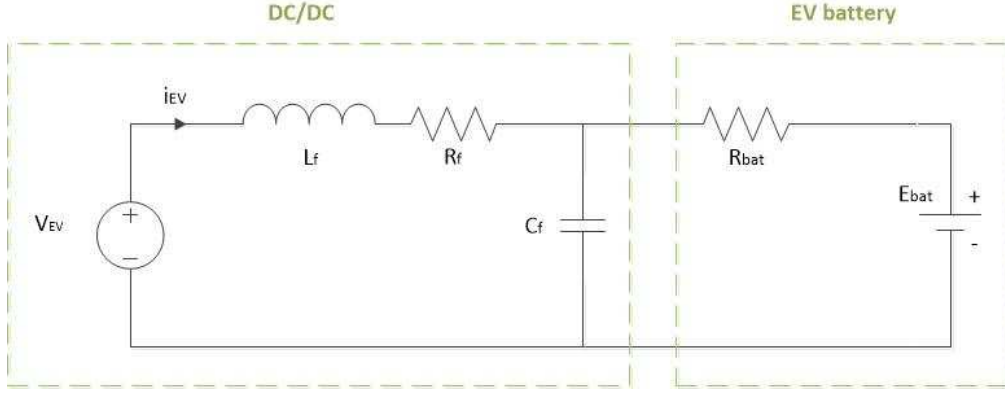
Figure 2.15: Equivalent circuit for the DC/DC plant

Applying the Kirchhoff's voltage law to the circuit shown in figure 2.15, (40) is obtained. For simplicity, the capacitor effect has been neglected, because this component does not influence the design of the current's controller for the EV battery. The capacitor is used only to obtain a little ripple in the output voltage.

$$V_{EV} = (R_f + R_{bat})i_{EV} + L_f \frac{di_{EV}}{dt} + E_{bat} \tag{40}$$

To design the control system for the DC/DC converter is necessary to obtain the plant with the mathematical formulation, so, to use the linear representation, is used the Laplace transformation. In this way, the equation in s-domain for the EV charger plant is shown in (41). In figure 2.16 the schematic representation for the plant is shown, where the output is the battery current and the inputs are the EV battery voltage and the converter voltage.
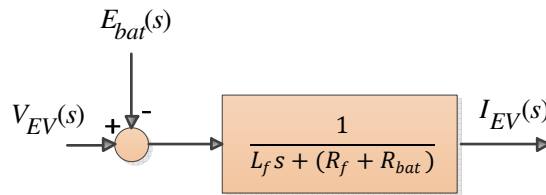
Figure 2.16: plant in s-domain for the DC/DC converter

$$I_{EV}(s) = \frac{1}{L_f s + (R_f + R_{bat})} (V_{EV}(s) - E_{bat}(s)) \tag{41}$$

CHAPTER 3

Design and Test of Charging Station with UPFC Configuration

In this chapter is explained the control system design of the charging station with the mathematical formulae. The power converters into the charging station with an integrated UPFC are PWM Voltage Source Converters (VSCs), for the STATCOM and SSSC converters the conversion system is a three-phase two level inverter, with IGBTs technology. Instead, the PWM bidirectional chopper is used to charge/discharge the EV battery.

To design the charging station two LV grids with the nominal voltage equal to 400 V and the nominal frequency equal to 50 Hz have been taken into consideration as shown in the figure 2.2.

The STATCOM control system is a V_{DC}/Q control type, instead, the SSSC control system is a P/Q control type. Both control systems work in dq synchronous control system and the PLL has been designed in dq rotating frame for the STATCOM and SSSC controllers.

The DC/DC converter control is a power control with two control loops; the outer loop to control the battery power dynamic and the inner loop to control the battery current dynamic. With this control type it is possible to use the EV battery in G2V or V2G mode.

3.1 STATCOM control system overview

In figure 3.1 is shown the STATCOM control system. The V_{DC}/Q controller is able to keep hold the V_{DC} voltage at the reference value and to control the reactive power exchanged between the STATCOM and the PCC of the feeder 1. So, in this way the power active balance in the DC link is assured as shown in the equation (42), where P_ρ is the STATCOM active power, P_σ is the active power exchanged between the SSSC and the three-phase series transformer, P_{EV} is the EV charging power and finally P_{loss} is the total active power losses (it is used the load convention). The control system has seven inputs: the PCC voltages of the feeder 1 in dq rotating frame, the converter currents in dq rotating frame, the DC link voltage and the set-points for the DC link voltage and for

the three-phase reactive power. The controller outputs are direct and quadrature converter voltages. Thanks to the inverse Park transformation, it is possible to obtain the three-phase voltages to apply to the inputs of the three-phase L filter. Finally, to generate PWM signals to send to the IGBTs of the STATCOM converter, it is used the sinusoidal modulation with the third harmonic injection.

$$P_\rho = P_\sigma + P_{EV} + P_{loss} \tag{42}$$
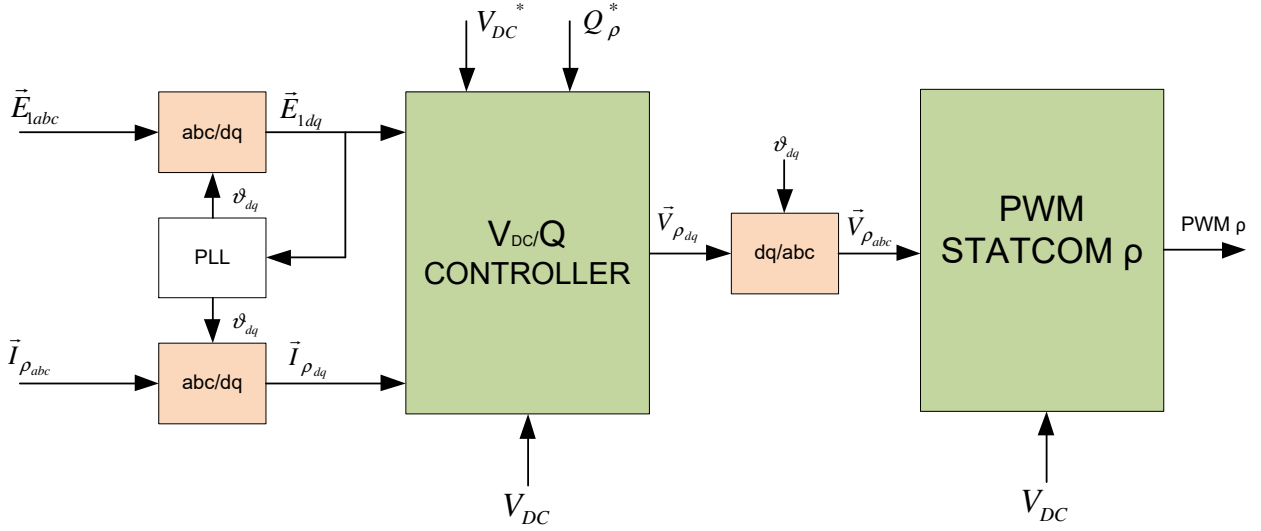
Figure 3.1: STATCOM Control system overview

3.2 STATCOM current controller

The control system has two control loops [30]; the first one is an inner loop and it is used to control the converter current, instead the second one is an outer loop to control the DC link voltage and the reactive power. For the inner loop was used the PI regulators to obtain the current values equal to the set-point values at steady state. (43) shows the set-points currents' vector, the currents' vector measured, the error currents' vector and the decoupling matrix. The proportional gains matrix and the integrator gains matrix are shown in (44). The gain values have been calculated considering the plant shown in figure 2.6, the integrator time constants τ_ρ are equal to the RL circuit time constant. In this way, it is possible to obtain the fast-current response. To limit the overshoot to 5% in the transient, the proportional gains are calculated with the damping equals 0.707 (T$_s$ is the sampling

time, and the controller parameters are shown in (45)). With the equation (46), it is possible to obtain the control algorithm for the current inner loop as shown in figure 3.2 (the matrix U is the identity matrix).

$$\vec{I}^*_{\rho dq} = \begin{vmatrix} i_{\rho d}^* \\ i_{\rho q}^* \end{vmatrix} \quad \vec{I}_{\rho dq} = \begin{vmatrix} i_{\rho d} \\ i_{\rho q} \end{vmatrix} \quad \vec{I}_{e\rho dq} = \begin{vmatrix} i_{\rho d}^* - i_{\rho d} \\ i_{\rho q}^* - i_{\rho q} \end{vmatrix} \quad \Omega_\rho = \begin{pmatrix} 0 & -\omega_{dq\rho}L_\rho \\ \omega_{dq\rho}L_\rho & 0 \end{pmatrix} \quad (43)$$

$$C_{pI\rho} = \begin{pmatrix} K_{pI\rho} & 0 \\ 0 & K_{pI\rho} \end{pmatrix} \quad C_{iI\rho} = \begin{pmatrix} K_{iI\rho} & 0 \\ 0 & K_{iI\rho} \end{pmatrix} \quad (44)$$

$$K_{pI\rho} = \frac{L_\rho}{3T_s} \quad \tau_\rho = \frac{L_\rho}{R_\rho} \quad K_{iI\rho} = \frac{K_{pI\rho}}{\tau_\rho} \quad (45)$$

$$\vec{V}_{\rho dq} = C_{pI\rho} \vec{I}_{e\rho dq} + C_{iI\rho} \int \vec{I}_{e\rho dq} dt + \Omega_\rho \vec{I}_{\rho dq} + U\vec{E}_{1dq} \quad (46)$$
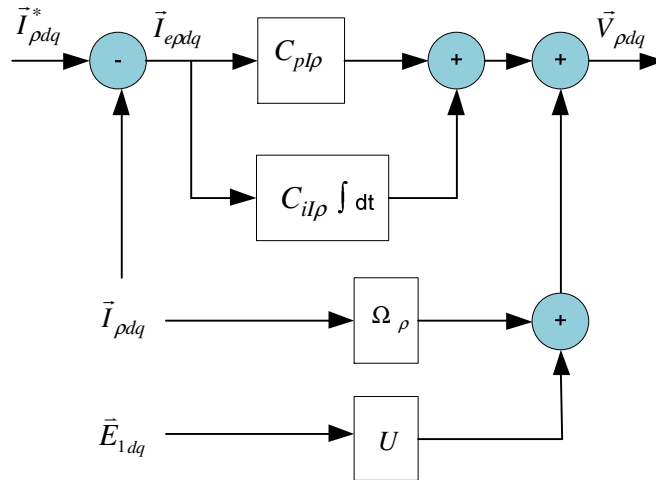

Figure 3.2: STATCOM Current controller

3.2.1 PLL for the STATCOM and SSSC control system

The STATCOM current controller and the SSSC control system work in dq rotating frame. The choice of the frame angle is very important to establish the bond between the current components and the active and reactive power. Thus, to obtain a proportional bond between the active power and the direct current component and between the reactive power and the quadrature current component, the dq frame angle was chosen equal to the grid voltage rotating vector angle. So, the grid voltage quadrature component is equal to zero and the direct component is equal to the grid voltage module. This method is called Voltage Orientated Control (VOC) technique [31]. In figure 3.3 is shown the alfa-beta static frame and the dq rotating frame orientated with VOC. To do this, it is necessary to use the PLL algorithm in dq frame. (47) shows the active and reactive power, instead, (48) and (49) show the PLL equations to obtain the algorithm shown in figure 3.4 with schematic representation. The PLL works with the grid voltage of the feeder 1, and for the STATCOM control system and for the SSSC control system has been chosen the same angle.
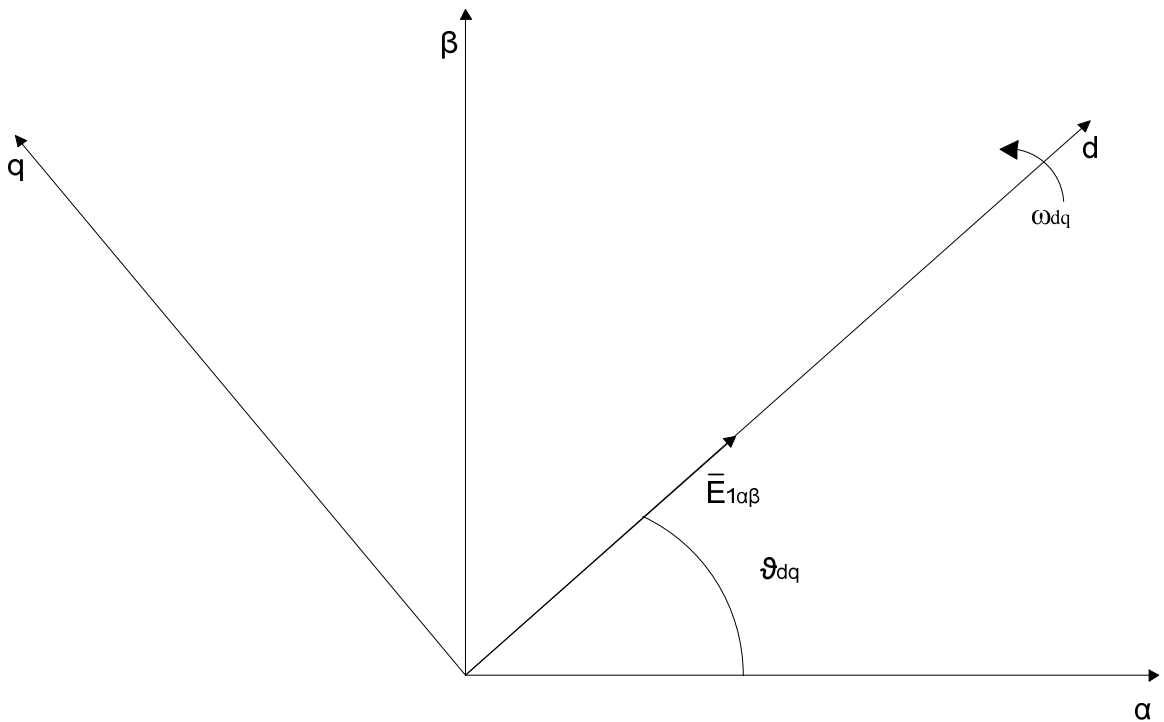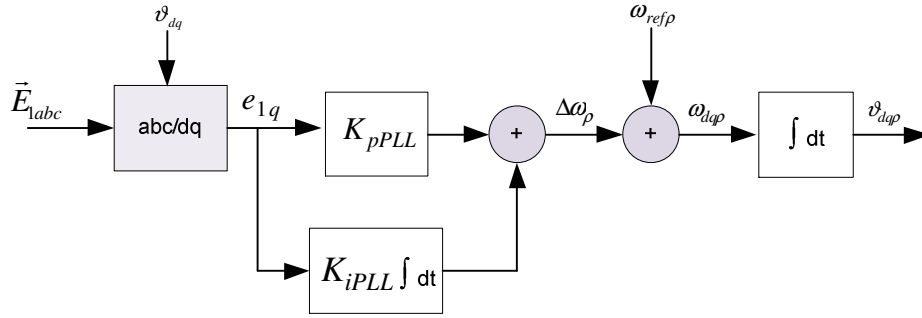

Figure 3.3: alpha-beta static frame and d-q rotating frame with VOC technique

$$P = \frac{3}{2} \; e_d i_d \quad Q = -\frac{3}{2} \; e_d i_q \tag{47}$$

$$\omega_{dq\rho} = K_{pPLL} e_{1q} + K_{iPLL} \int e_{1q} dt + \omega_{ref\rho} \tag{48}$$

$$\vartheta_{dq\rho} = \int \omega_{dq\rho} dt \tag{49}$$

Figure 3.4: PLL scheme in dq frame

3.3 STATCOM DC voltage and reactive controller

The outer loop to control the DC voltage is shown in the figure 3.5, where the inputs are the DC link voltage set-point, the reactive power set point, the DC link voltage and reactive power measured. The outputs are the set-points for the current inner loop; the direct component of the current to control the active power and the quadrature component of the current to control the reactive power. For the direct component is used the PI regulator; thanks to it, is possible to obtain the balance equation (42) at the steady state. The proportional gain and the integrator gain was chosen so that the outer loop dynamic is slower than the inner loop dynamic.

$$i^*_{\rho d} = K_{pV\rho}(V^*_{DC} - V_{DC}) + K_{iV\rho} \int (V^*_{DC} - V_{DC}) dt \tag{50}$$

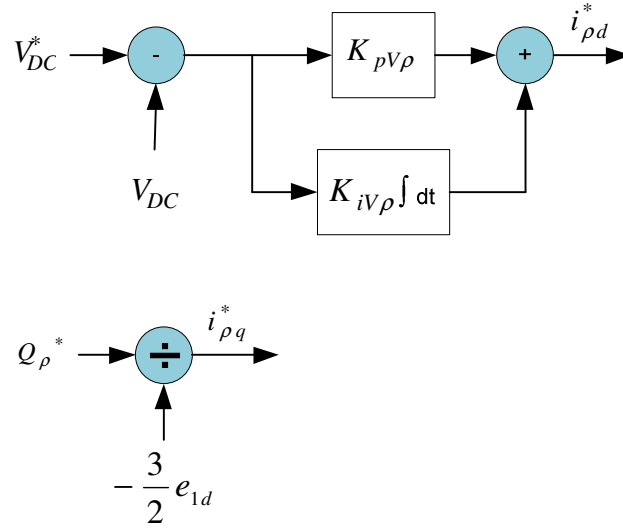$$i^*_{\rho q} = -\frac{Q^*_\rho}{\frac{3}{2} e_{1d}} \tag{51}$$

Figure 3.5: STATCOM Voltage and reactive power controller

3.4 SSSC control system overview

In figure 3.6 is shown the SSSC control system. The P/Q controller is able to control the active and the reactive power between two electric feeders. The control system has eight inputs: the PCC voltages of the feeder 1 in dq rotating frame, the PCC voltages of the feeder 2 in dq rotating frame, the converter currents in dq rotating frame and the set-points for the three-phase active power and for the three-phase reactive power. The controller outputs are direct and quadrature converter voltages. Using the inverse Park transformation, it is possible to obtain the three-phase voltages to apply to the inputs of the three-phase L filter. Finally, to generate PWM signals to send to the IGBTs of the SSSC converter, it is used the sinusoidal modulation with the third harmonic injection.
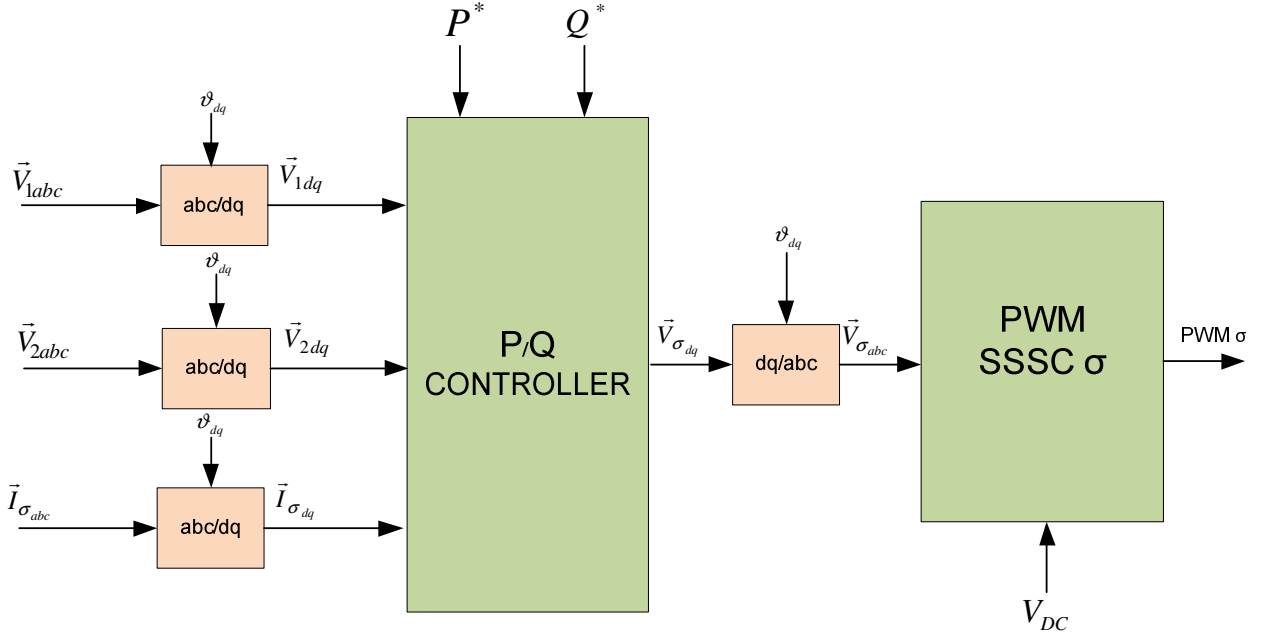
Figure 3.6: SSSC control system overview

3.5 SSSC current controller

The control system has one current control loop; the design of the current controller is similar to the STATCOM current control loop, the plant used is shown in figure 2.8. The current controlled is the interline current between the two feeders. The main difference between the two converters is the forward compensation, in the STATCOM current controller there is the grid voltage instead in the SSSC current controller there is the difference between two feeders' voltages. (52) shows the set-points currents' vector, the currents' vector measured, the error currents' vector and the decoupling matrix. The proportional gains matrix and the integrator gains matrix are shown in (53). The gain values have been calculated considering the plant shown in figure 2.8. (The controller parameters are shown in (54)). With the equation (55), it is possible to obtain the control algorithm for the current inner loop as shown in figure 3.7 (the matrix U is the identity matrix).

$$\vec{I}^*_{\sigma dq} = \begin{vmatrix} i_{\sigma d}{}^* \\ i_{\sigma q}{}^* \end{vmatrix} \quad \overrightarrow{I_{\sigma}}_{dq} = \begin{vmatrix} i_{\sigma d} \\ i_{\sigma q} \end{vmatrix} \quad \overrightarrow{I_{e\sigma}}_{dq} = \begin{vmatrix} i_{\sigma d}{}^* - i_{\sigma d} \\ i_{\sigma q}{}^* - i_{\sigma q} \end{vmatrix} \quad \Omega_{\sigma} = \begin{pmatrix} 0 & -\omega_{dq\rho}L_{\sigma} \\ \omega_{dq\rho}L_{\sigma} & 0 \end{pmatrix} \quad (52)$$

$$C_{pI\sigma} = \begin{pmatrix} K_{pI\sigma} & 0 \\ 0 & K_{pI\sigma} \end{pmatrix} \quad C_{iI\sigma} = \begin{pmatrix} K_{iI\sigma} & 0 \\ 0 & K_{iI\sigma} \end{pmatrix} \quad (53)$$

$$K_{pI\sigma} = \frac{L_{\sigma}}{3T_{s}} \quad \tau_{\sigma} = \frac{L_{\sigma}}{R_{\sigma}} \quad K_{iI\sigma} = \frac{K_{pI\sigma}}{\tau_{\sigma}} \quad (54)$$

$$\overrightarrow{V_{\sigma}}_{dq} = C_{pI\sigma}\overrightarrow{I_{e\sigma}}_{dq} + C_{iI\sigma}\int \overrightarrow{I_{e\sigma}}_{dq}dt + \Omega_{\sigma}\overrightarrow{I_{\sigma}}_{dq} + U(\overrightarrow{V_2}_{dq} - \overrightarrow{V_1}_{dq}) \quad (55)$$
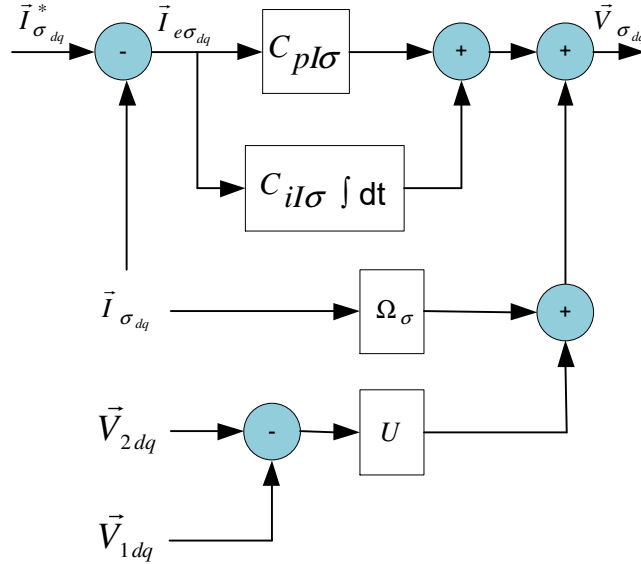

Figure 3.7: SSSC Current controller

3.6 SSSC current set-points calculator

To obtain the current direct and quadrature components set-points for the inner loop, the relation between powers and currents is shown in (56). The current direct and quadrature set-points depend on from the active set-point P* and the reactive set-point Q*. These last set-points are the AC powers between the two feeders. Figure 3.8 shows a simple schematic representation of the

equation (56), where the inputs are the powers set-points and the outputs are the currents set-points for the current controller.

$$\begin{vmatrix} i_{\sigma d}^* \\ i_{\sigma q}^* \end{vmatrix} = \frac{2}{3} \frac{1}{v_{1_d}{}^2 + v_{1_q}{}^2} \begin{pmatrix} v_{1_d} & v_{1_q} \\ v_{1_q} & -v_{1_d} \end{pmatrix} \begin{vmatrix} P^* \\ Q^* \end{vmatrix} \tag{56}$$
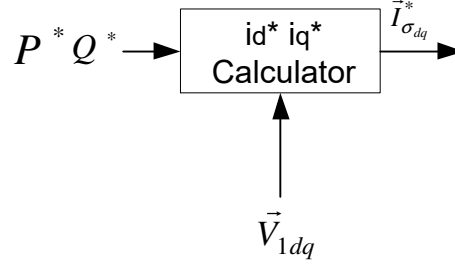
Figure 3.8: Scheme to calculate direct and quadrature components for the current inner loop

3.7 DC/DC power controller

The PWM DC/DC converter thanks to the power controller, it is able to charge or to discharge the EV battery [32]. The inputs of this controller are the DC link voltage V_{DC}, the battery voltage E_{bat} (measured after the LC filter) and the battery current i_{EV}. The output is the modulation index to obtain the PWM signals to send to IGBTs. (57) shows the power error P_{eEV}; it is equal to difference between battery power set-point and battery power measured. (58) shows the power control equation, where is used a classical PI regulator to reach the power set-point at steady state. The design of this controller is made considering the current control inner loop dynamic, so, the proportional gain and the integrator gain were calculated to have a slower power dynamic than the current dynamic. (59) shows the current error where i_{eEV} is equal to difference between battery current set-point and battery current measured. (60) shows the current control equation, where with a classical PI regulator it is possible to reach the current set-point at steady state with a fast dynamic. The design of the current controller has been made considering the DC link voltage

dynamic. Finally, (61) shows the converter voltage V_{EV} that it is applied to the LC filter. In figure 3.9 is shown the DC/DC control schematic representation.
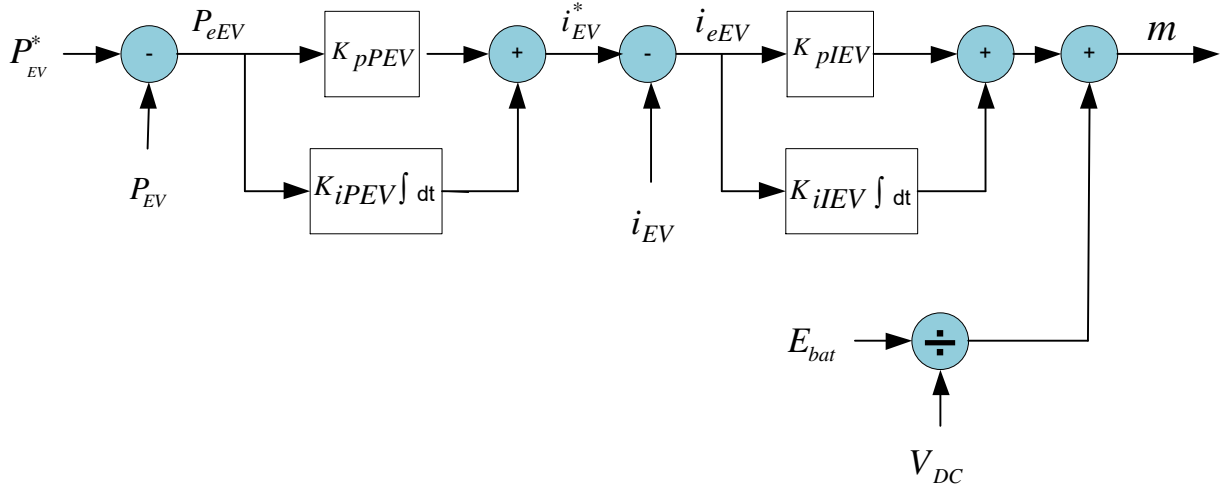
$$P_{eEV} = P_{EV}^* - P_{EV} \tag{57}$$

$$i_{EV}^* = K_{pPEV}P_{eEV} + K_{iPEV}\int P_{eEV}dt \tag{58}$$

$$i_{eEV} = i_{EV}^* - i_{EV} \tag{59}$$

$$m = K_{pIEV}i_{eEV} + K_{iIEV}\int i_{eEV}dt + \frac{E_{bat}}{V_{DC}} \tag{60}$$

$$V_{EV} = mV_{DC} \tag{61}$$

Figure 3.9: EV Battery control

3.8 Power circuit and control parameters

In table 3.1 are listed the main technical parameters about the STATCOM power circuit, the SSSC power circuit and the DC/DC power circuit including the filters parameters. Furthermore, in the table are shown the gains control parameters for all power electronics converters.

Table 3.1: DC charging station with UPFC main technical parameters

| Parameter	Value	Parameter	Value
Grid rated voltage feeder 1 [V]	400	Inductance LC filter DC side [mH]	5
Grid rated voltage feeder 2 [V]	400	Capacitor LC filter DC side [μF]	50
Grid rated frequency [Hz]	50	L filters nominal value AC side STATCOM/SSSC [mH]	5/3
Ohmic component grid 1 impedance [Ω]	0.1	DC link capacitor [μF]	1000
Inductive component grid 1 impedance [mH]	1	Battery resistance [Ω]	0.3
Ohmic component grid 2 impedance [Ω]	0.1	STATCOM current loop proportional gain $K_{pI\rho}$ [V/A]	20.00
Inductive component grid 2 impedance [mH]	1	STATCOM current loop integrator gain $K_{iI\rho}$ [V/A]	666.67
STATCOM switching frequency [kHz]	10	STATCOM voltage loop proportional gain $K_{pV\rho}$ [A/V]	2.00
SSSC switching frequency [kHz]	10	STATCOM voltage loop integrator gain $K_{iV\rho}$ [A/V]	6.67
DC/DC converter switching frequency [kHz]	10	SSSC current loop proportional gain $K_{pI\sigma}$ [V/A]	10.00
Rated apparent power [kVA]	30	SSSC current loop integrator gain $K_{iI\sigma}$ [V/A]	333.33
Rated EV charger power [kW]	20	DC/DC current loop proportional gain K_{pIEV} [p.u./A]	0.01
DC link Voltage [V]	650	DC/DC current loop integrator gain K_{iIEV} [p.u./A]	1
EV Charger Voltage [V]	200-500	DC/DC power loop proportional gain K_{pPEV} [A/W]	0.001
Battery voltage [V]	300	DC/DC power loop integrator gain K_{iPEV} [A/W]	0.1

3.9 Test cases

To test the charging station have been made two tests with MATLAB/Simulink software. In the first one it is simulated the active and reactive power flow control with UPFC converter integrated in the charging station, in particular, active and reactive power flow from grid 1 to grid 2 has been made by SSSC converter, so in this way it is possible to avoid a congestion problem in the grid 2 or to decrease the grid 2 load increasing the grid 2 capability. In the second one there is an active power flow inversion in the grid 2, so with a proposed device, the excess green active power is used to charge the EV and at the same time it is used partially to supply the loads.

3.9.1 Case 1: active and reactive power flow control

In the study case 1, the charging station (with UPFC configuration) is used to charge the EV and it is used to control the active and the reactive power flow between the grid 1 and the grid 2. In figure 3.10 is shown the test model where there are two loads: the load 1 connected to the feeder 1 and the load 2 connected to the feeder 2. With the UPFC integrated in the charging station, at time equals 0.5 s the load 2 is supplied from grid 1 and from grid 2, so, in this way the grid 2 has more power capability or in the case of emergency contingency it is possible to improve the power quality using the UPFC; in fact, it is possible to use the grid 1 to supply the grid 2 loads partially or totally thanks to the interline link in the charging station. In table 3.2 are reassumed the case 1 power values of the all components before and after the SSSC operations at time equals 0.5 s.
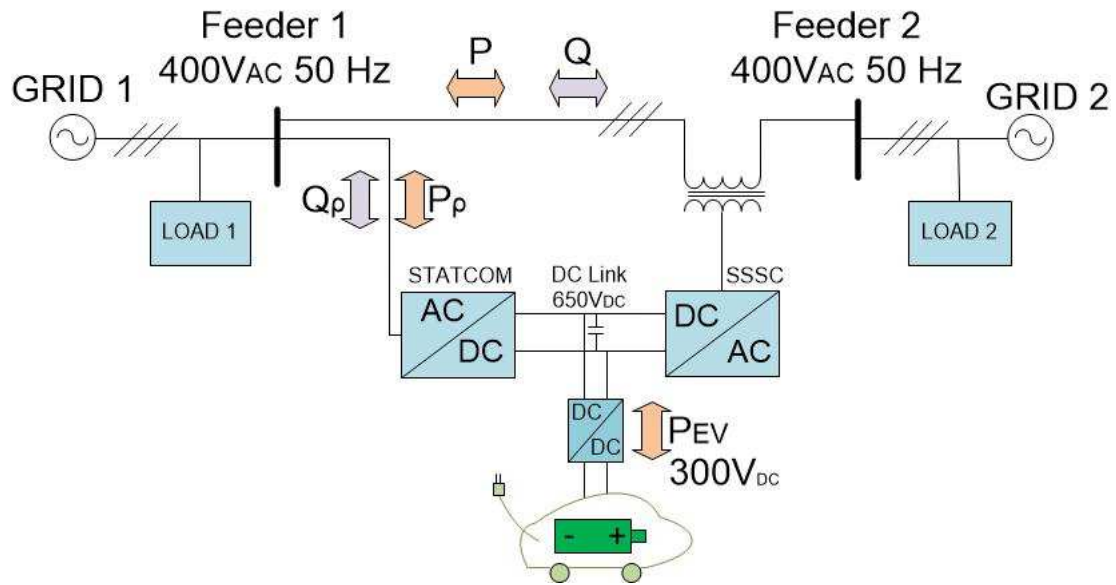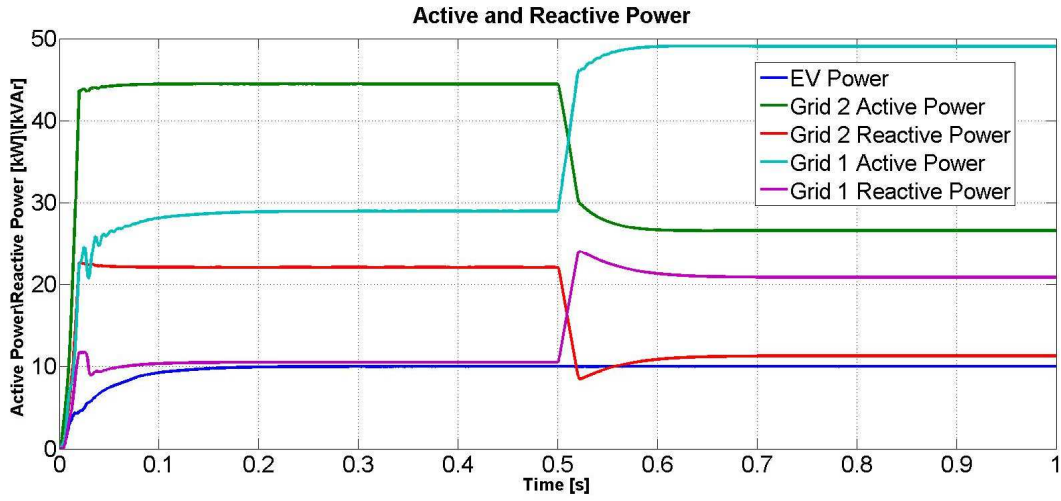
Figure 3.10: Case 1 test model

Table 3.2: Case 1 test power values

Active and reactive powers	Before	After
Grid 1 active power [kW] \ Load 1 active power [kW]	**29** \ 20	**49** \ 20
Grid 1 reactive power [kVAr] \ Load 1 reactive power [kVAr]	**10** \ 10	**21** \ 10
Grid 2 active power [kW] \ Load 2 active power [kW]	**44** \ 50	**27** \ 50
Grid 2 reactive power [kVAr] \ Load 2 reactive power [kVAr]	**22** \ 20	**11** \ 20
EV charging power [kW]	**10**	**10**

Figure 3.11 shows the active and the reactive power of the test model. The EV charging power is equal to 10 kW for all simulation time, instead, the active power flow between the two feeders is equal to 20 kW from grid 1 to grid 2 to supply partially the load 2 after 0.5 s The reactive power between two feeders is equal to zero before time equals 0.5 s and it is equal to 11 kVAr after 0.5 s. So, with the proposed device, it is possible to charge the EV and to supply the load 2 from both grids. The loads used for both feeders are constant impedance loads.
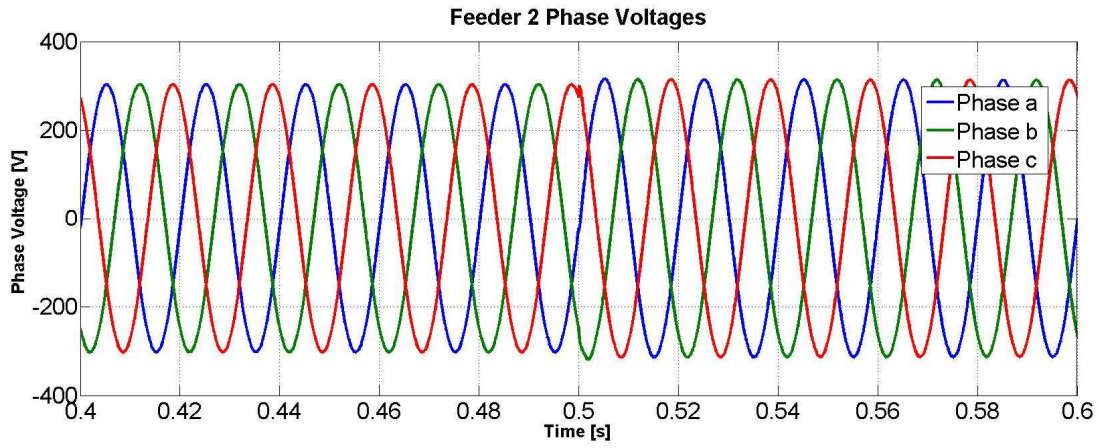
Figure 3.11: Test model active and reactive power

In figure 3.12 are shown PCC feeder 1 phase voltages, where it is possible to see a little decrement of the voltage magnitude for all phases due to the increase of the grid 1 currents after 0.5 s.
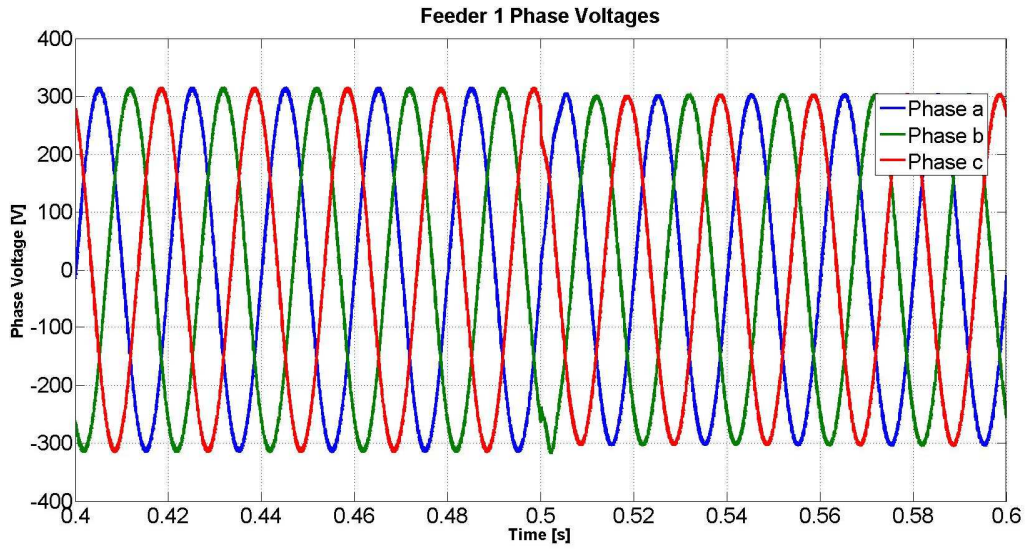

Figure 3.12: PCC of feeder 1 phase voltages

In figure 3.13 are shown PCC feeder 2 phase voltages, where it is possible to see a little increment of the voltage magnitude for all phases due to the decrease of the grid 2 currents after the time equal 0.5 s.

Figure 3.13: PCC of feeder 2 phase voltages

Figure 3.14 shows grid 1 line currents, where it is possible to see the increase of the current magnitudes after 0.5 s due to the SSSC that moves active and reactive power from the PCC of the feeder 1 to the PCC of the feeder 2. Instead, in figure 3.15 is shown grid 2 line currents, where is shown the decrease of grid 2 line currents after 0.5 s.
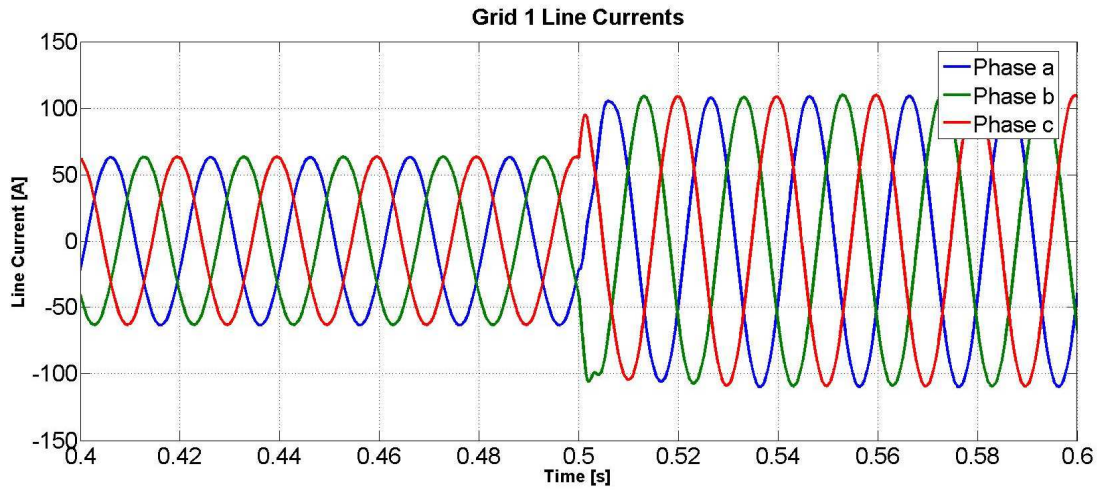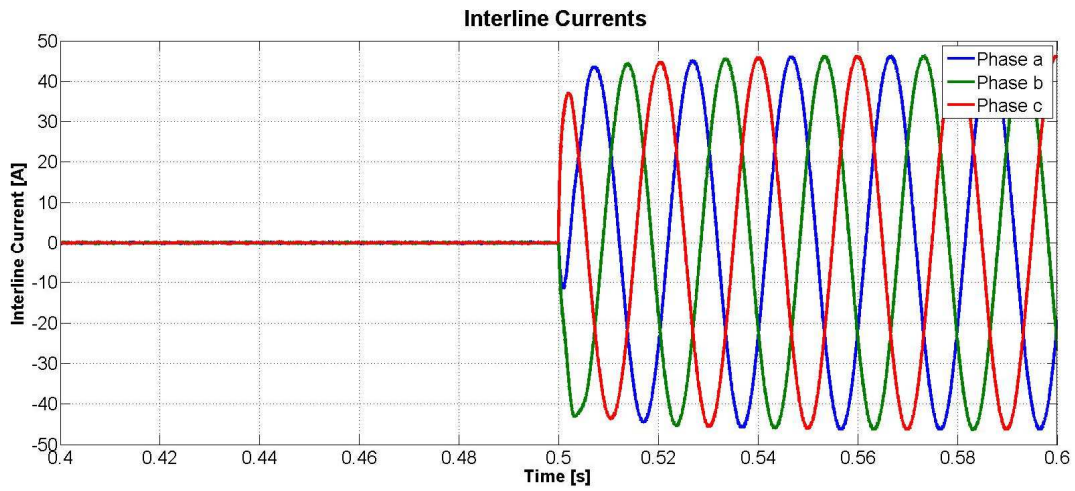

Figure 3.14: Grid 1 line currents
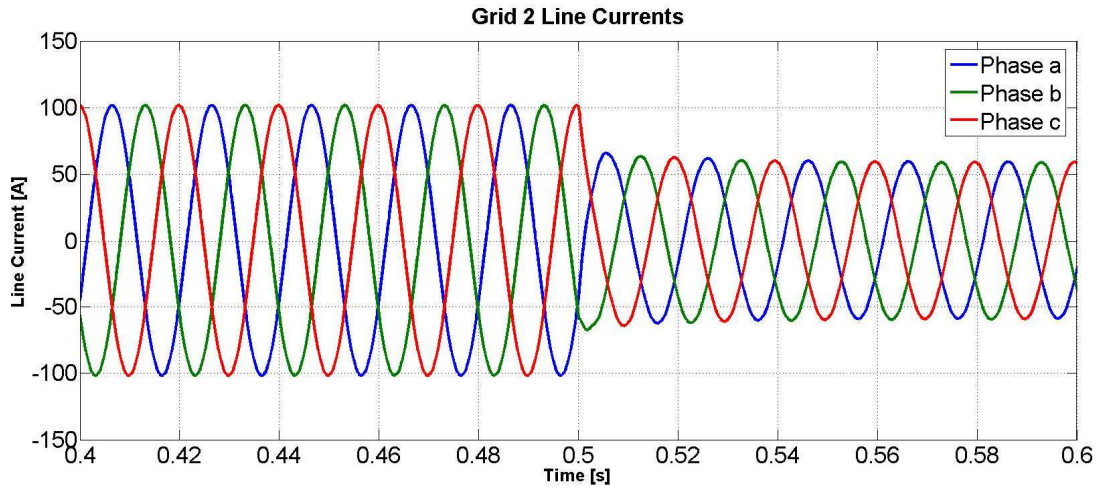
Figure 3.15: Grid 2 line currents

Figure 3.16 shows interline currents between two feeders. After 0.5 s the interline currents flows from the PCC of the feeder 1 to the PCC of the feeder 2 using the SSSC.

Figure 3.16: Interline currents between the two feeders

Finally, the figure 3.17 shows the EV battery voltage and the EV battery current; the values are constant for all simulation time thanks to the DC/DC converters.
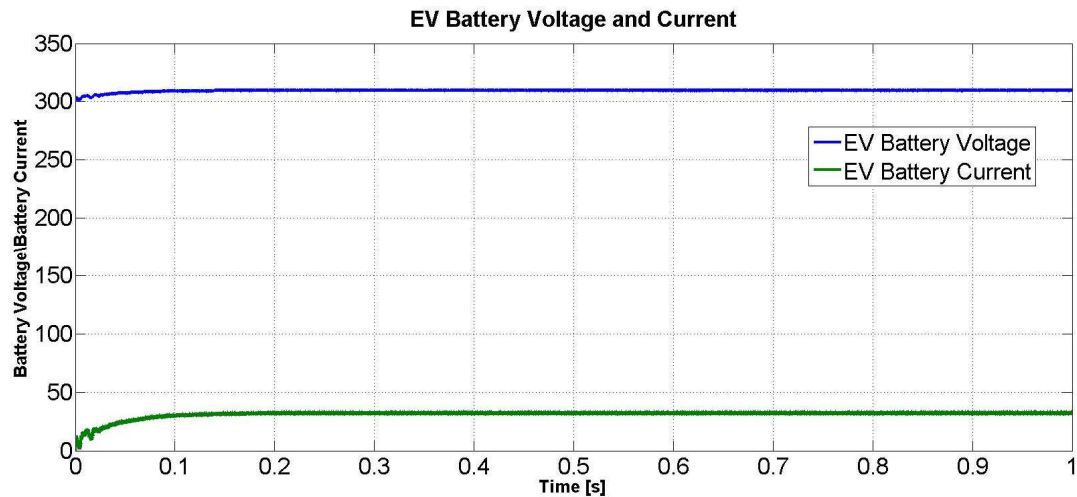
Figure 3.17: EV Battery voltage and current

3.9.2 Case 2: active power flow inversion

In the study case 2, the charging station (with UPFC configuration) charges the EV and it uses the green energy in the best way; in fact, the solar active power is higher than the load power, so, thanks to the UPFC at time equals 0.5 s the load 1 is supplied from the solar generator and the charging power is increased of 10 kW. In this way in the grid 2 has been avoided the power flow inversion and the green energy has been used to supply the load 1 in the grid 1 and to decrease the charging time. In figure 3.18 is shown the case 2 test model and in the table 3.3 are reassumed the case 2 power values of the all components before and after the SSSC operations at time equals 0.5 s.

Figure 3.18: Case 2 test model
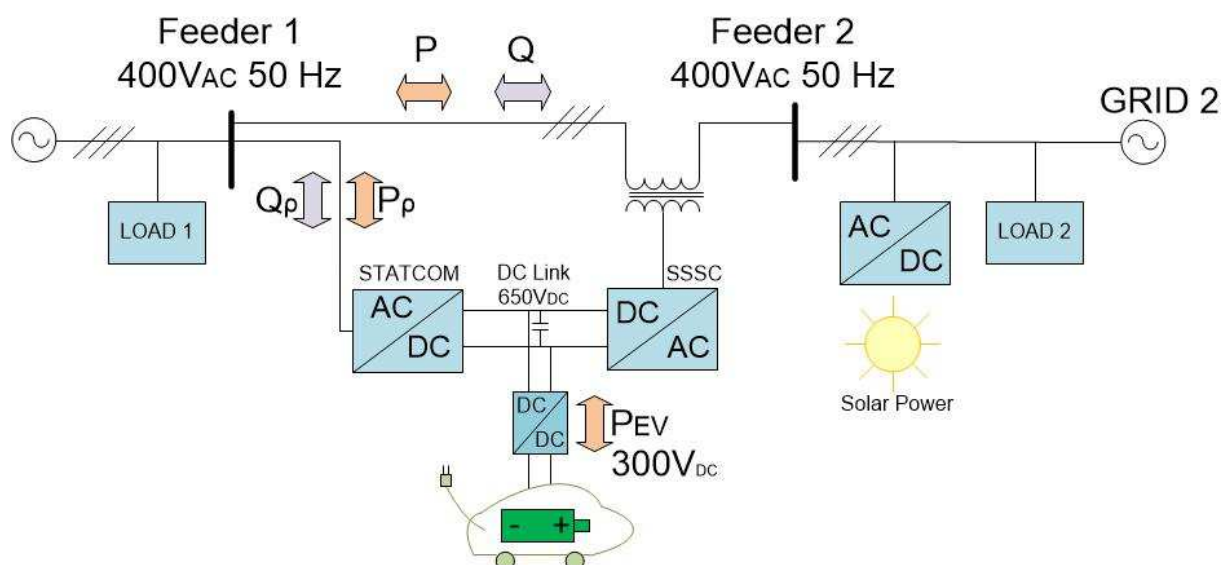
Table 3.3: Case 2 test power values

| Active and reactive powers	Before	After
Solar active power [kW]	30	30
Grid 1 active power [kW] \ Load 1 active power [kW]	15 \ 10	5 \ 10
Grid 1 reactive power [kVAr] \ Load 1 reactive power [kVAr]	7 \ 7	2 \ 7
Grid 2 active power [kW] \ Load 2 active power [kW]	-10 \ 20	9 \ 20
Grid 2 reactive power [kVAr] \ Load 2 reactive power [kVAr]	5 \ 5	5 \ 5
EV charging power [kW]	5	15

Figure 3.19 shows the active and the reactive power of the test model. The EV charging power is equal to 5 kW before 0.5 s and it is equal to 15 kW after 0.5 s. On the feeder 2 there is the load 2 with 20 kW and 5 kVAr and the power solar generation equals 30 kW. So, before 0.5 s in the grid 2 there is an inversion of active power flow; the active power injected in the grid 2 is equal to 10 kW. Using the SSSC after 0.5 s, 20 kW are injected in the grid 1 from the grid 2. So, in this way the grid supplies 10 kW and the charging time is decreased.
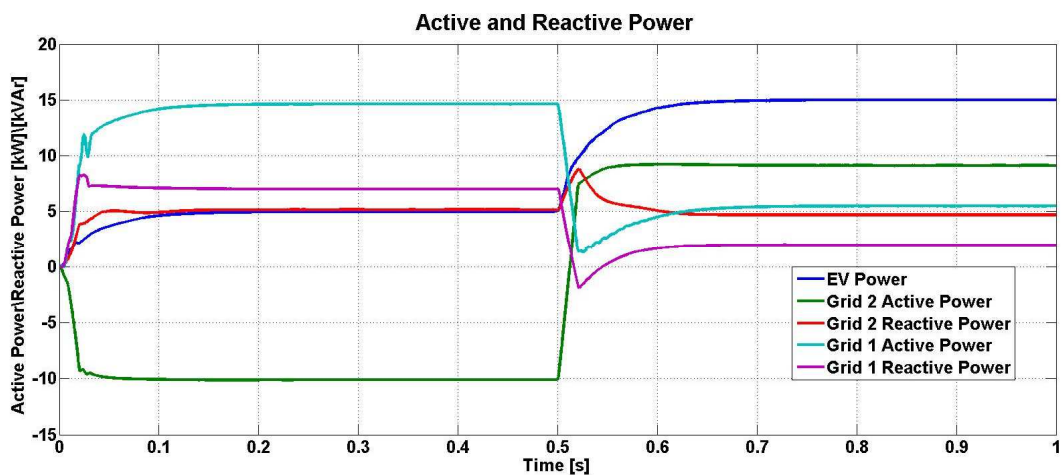
Figure 3.19: Test model active and reactive power

In figure 3.20 are shown PCC feeder 1 phase voltages, where it is possible to see a little increment of the voltage magnitude for all phases due to the decrease of the grid 1 currents after 0.5 s.
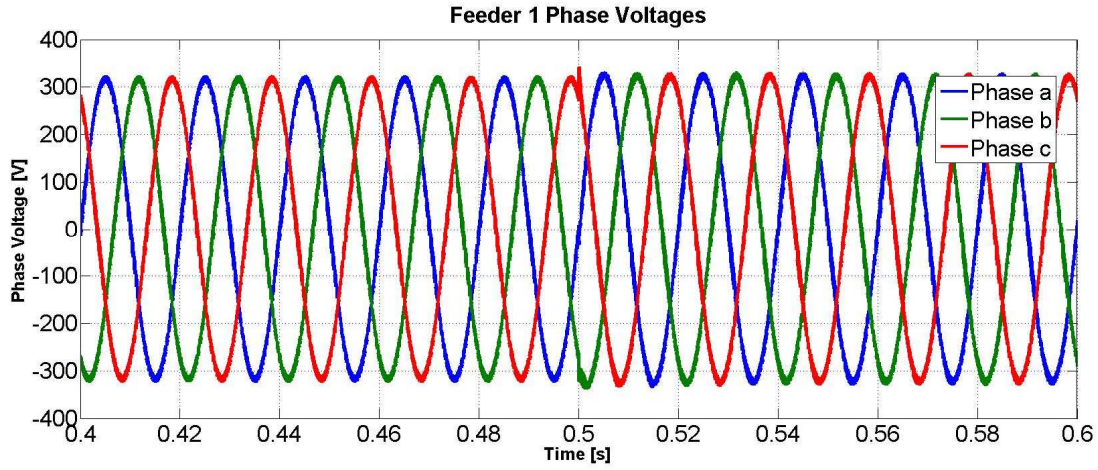
Figure 3.20: PCC of feeder 1 phase voltages

In figure 3.21 are shown PCC feeder 2 phase voltages, where the voltage magnitude is constant before and after the time equals 0.5 s.
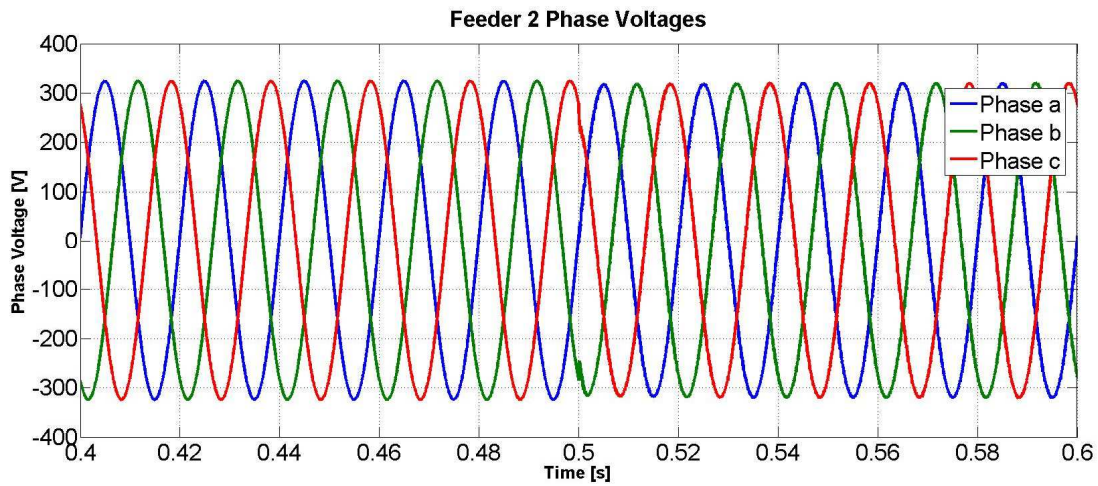
Figure 3.21: PCC of feeder 2 phase voltages

Figure 3.22 shows grid 1 line currents, where it is possible to see the decrease of the current magnitudes after 0.5 s due to the SSSC that moves active power from the PCC of the feeder 2 to the PCC of the feeder 1. Instead, in figure 3.23 are shown grid 2 line currents, where is shown the phase change of grid 2 line currents after 0.5 s.
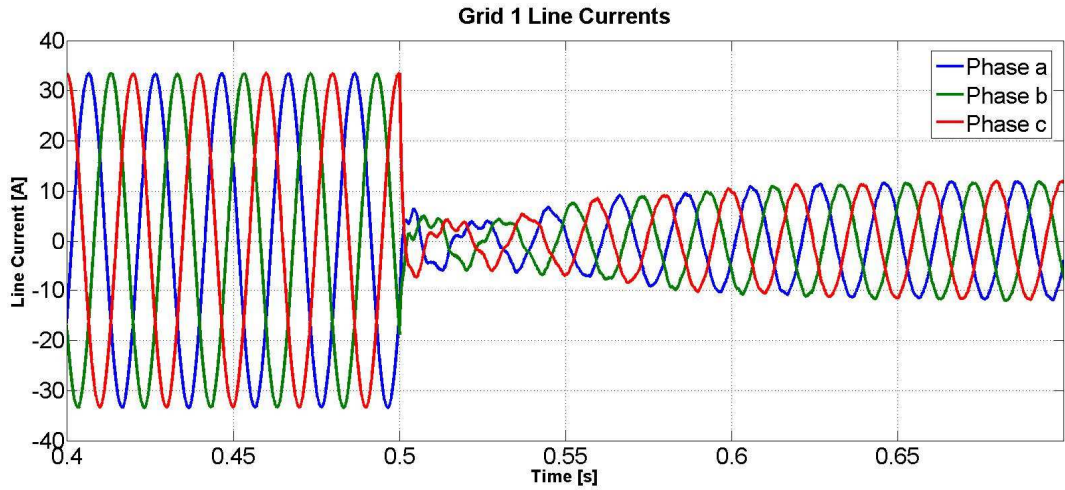
Figure 3.22: Grid 1 line currents
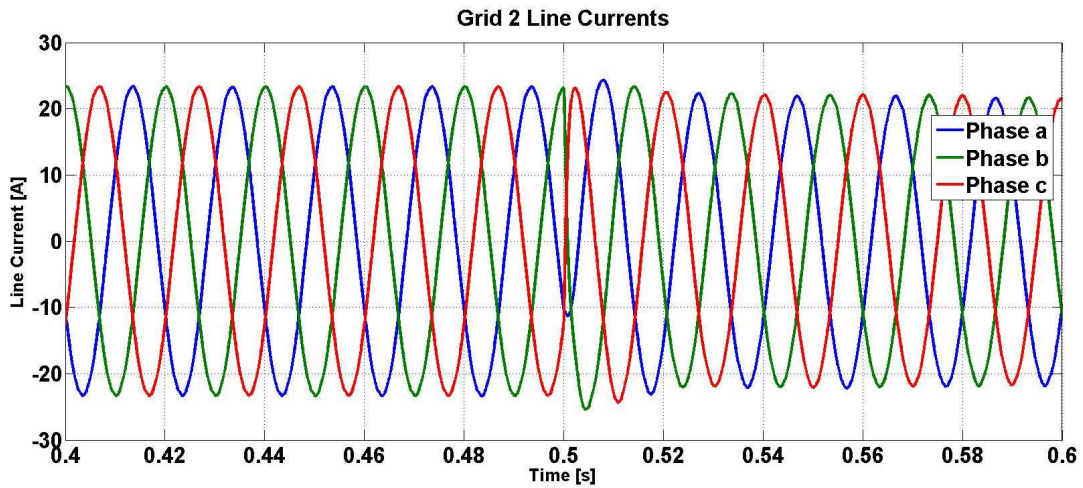
Figure 3.23: Grid 2 line currents

Figure 3.24 shows interline currents between two feeders. After 0.5 s the interline currents flow from the PCC of the feeder 2 to the PCC of the feeder 1 using the SSSC to use the excess power in the grid 2 to supply partially the load 1 and to charge partially the EV battery.
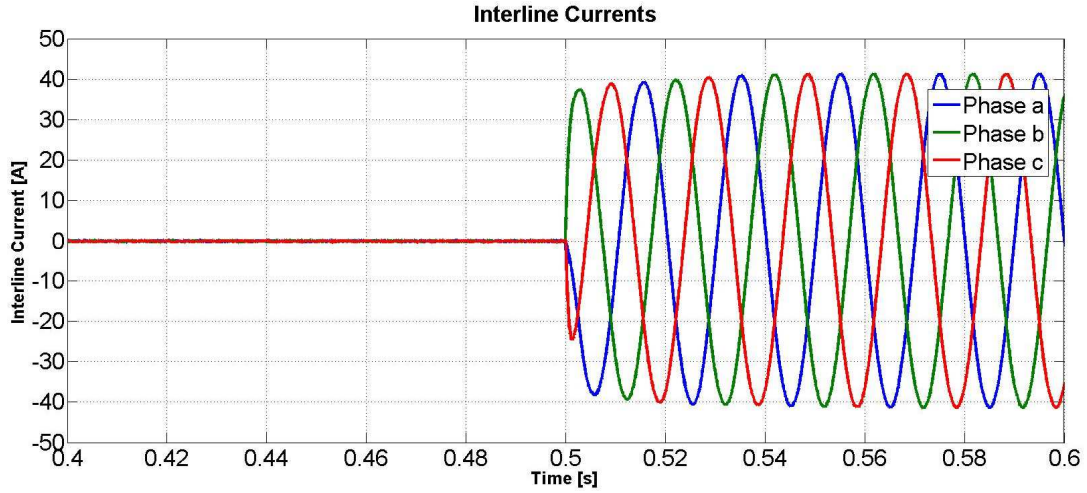
Figure 3.24: Interline currents between the two feeders

Finally, the figure 3.25 shows the EV battery voltage and the EV battery current; the values changes after 0.5 s to increase the charging power. This is possible thanks to the DC/DC converter power control.
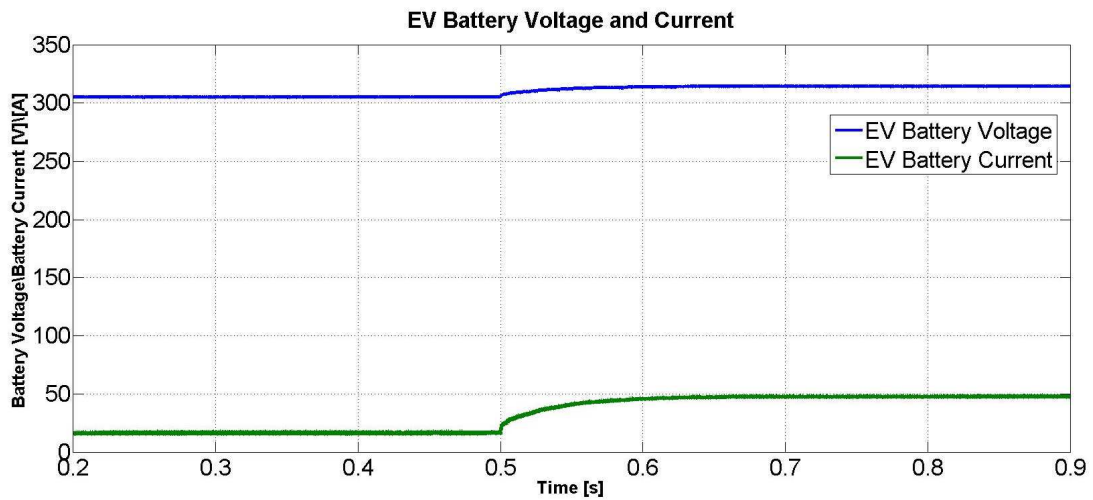
Figure 3.25: EV Battery voltage and current

CHAPTER 4

Design and Test of Charging Station with B2B Configuration

In this chapter the control system design of the charging station is explained with mathematical formulae. The power converters into the charging station with an integrated B2B are PWM VSCs. For the pilot and co-pilot converters the conversion system is a three-phase two level inverter with IGBTs technology. Instead, the PWM bidirectional chopper is used to charge/discharge the EV battery. To design the charging station two LV grids with the nominal voltage equal to 400 V and the nominal frequency equal to 50 Hz have been taken into consideration as shown in the figure 2.9. The pilot converter control system is a P/Q control type instead the co-pilot converter control system is a V_{DC}/Q control type. Both control systems work in dq synchronous rotating frame and the PLL for both converters have been designed in dq frame with the VOC technique.

The DC/DC converter control is equal to the converter control for the charging station with UPFC solution.

4.1 Pilot converter control system overview

In figure 4.1 is shown the pilot converter control system. The P/Q controller is able to control the active power between the two feeders and the reactive power in the PCC of the feeder 1. Has been chosen the name "pilot" because the converter with P/Q control it is able to set the active and reactive power between two feeders, so, the "co-pilot" converter will follow the pilot converter. The control system has six inputs: the grid voltages in dq rotating frame, the converter currents in dq rotating frame and the set-points for the three-phase active and for the three-phase reactive power. The controller outputs are direct and quadrature converter voltages. Using the inverse Park transformation, it is possible to obtain the three-phase voltages to apply to the inputs of the three-phase LCL filter. Finally, to generate PWM signals to send to the IGBTs of the pilot converter it is used the sinusoidal modulation with the third harmonic injection.
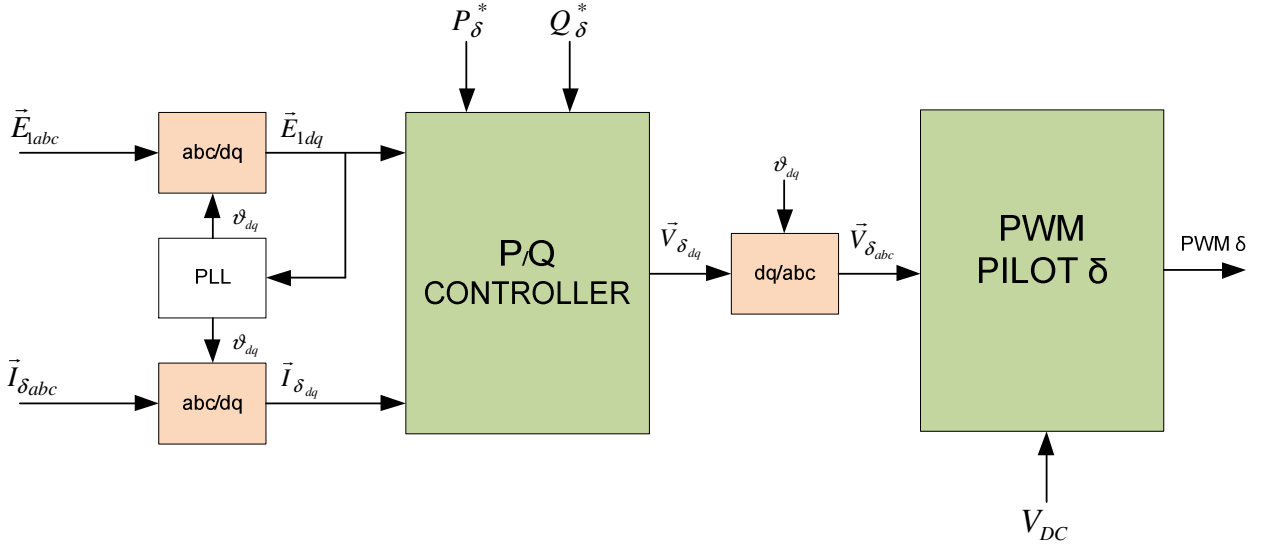
Figure 4.1: Pilot Control system overview

4.2 Pilot current controller

The control system has two control loops; the first one is an inner loop and it is used to control the converter current, instead, the second one is an outer loop to control the active power and the reactive power. For the inner loop was used the PI regulators to obtain the current values equal to the set-point values at steady state. (62) shows the set-points currents' vector, the currents' vector measured, the error currents' vector and the decoupling matrix. The proportional gains matrix and the integrator gains matrix are shown in (63). The gain values have been calculated considering the plant shown in figure 2.12, the integrator time constants τ_δ are equal to the RL circuit time constant. In this way, it is possible to obtain the fast-current response. To limit the overshoot to 5% in the transient, the proportional gains are calculated with the damping equals 0.707 (T_s is the sampling time, and the controller parameters are shown in (64)). With the equation (65), it is possible to obtain the control algorithm for the current inner loop as shown in figure 4.2 (the matrix U is the identity matrix).

$$\vec{I}^*_{\delta_{dq}} = \begin{vmatrix} i_{\delta d}^* \\ i_{\delta q}^* \end{vmatrix} \quad \overrightarrow{I_\delta}_{dq} = \begin{vmatrix} i_{\delta d} \\ i_{\delta q} \end{vmatrix} \quad \overrightarrow{I_{e\delta}}_{dq} = \begin{vmatrix} i_{\delta d}^* - i_{\delta d} \\ i_{\delta q}^* - i_{\delta q} \end{vmatrix} \quad \Omega_\delta = \begin{pmatrix} 0 & -\omega_{dq\delta}L_\delta \\ \omega_{dq\delta}L_\delta & 0 \end{pmatrix} \quad (62)$$

$$C_{pI\delta} = \begin{pmatrix} K_{pI\delta} & 0 \\ 0 & K_{pI\delta} \end{pmatrix} \quad C_{iI\delta} = \begin{pmatrix} K_{iI\delta} & 0 \\ 0 & K_{iI\delta} \end{pmatrix} \quad (63)$$

$$K_{pI\delta} = \frac{L_\delta}{3T_s} \quad \tau_\delta = \frac{L_\delta}{R_\delta} \quad K_{iI\delta} = \frac{K_{pI\delta}}{\tau_\delta} \quad (64)$$

$$\overrightarrow{V_\delta}_{dq} = C_{pI\delta}\overrightarrow{I_{e\delta}}_{dq} + C_{iI\delta}\int \overrightarrow{I_{e\delta}}_{dq}dt + \Omega_\delta \overrightarrow{I_\delta}_{dq} + U\overrightarrow{E_1}_{dq} \quad (65)$$
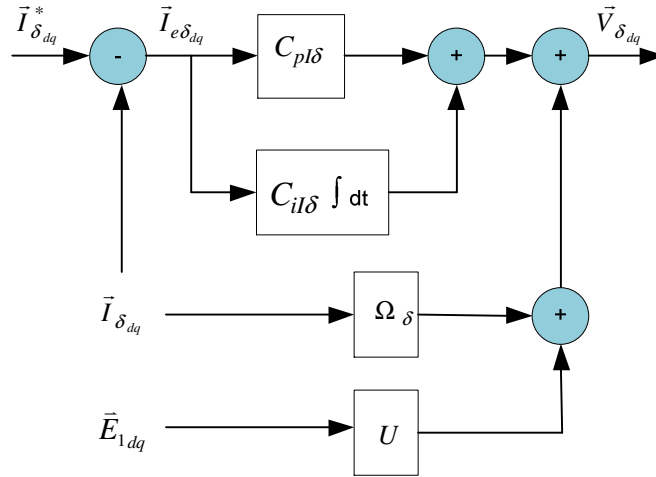
Figure 4.2: PILOT Current controller

4.3 Pilot power controller

The power controller is the outer loop to set the current set-points for the inner loop. To obtain the power values equal to the set-point values at steady state was used the PI regulators. (66) shows the power set-points' vector, the powers' vector measured, the power errors' vector and the decoupling matrix. The proportional gains matrix and the integrator gains matrix are shown in (67). To calculate the active and reactive power in dq rotating frame has been used the low pass filters to obtain the constant value for voltages and currents. The gain values have been calculated to have a slower dynamic than the current inner loop dynamic to assure a right working for the current

controller. With the equation (68), it is possible to obtain the control algorithm for the power control loop as shown in figure 4.3.

$$\bar{\Gamma}_\delta^* = \begin{vmatrix} P_\delta^* \\ Q_\delta^* \end{vmatrix} \quad \bar{\Gamma}_\delta = \begin{vmatrix} P_\delta \\ Q_\delta \end{vmatrix} \quad \bar{\Gamma}_{e\delta} = \begin{vmatrix} P_\delta^* - P_\delta \\ Q_\delta^* - Q_\delta \end{vmatrix} \tag{66}$$

$$C_{p\Gamma\delta} = \begin{pmatrix} K_{pP\delta} & 0 \\ 0 & K_{pQ\delta} \end{pmatrix} \quad C_{i\Gamma\delta} = \begin{pmatrix} K_{iP\delta} & 0 \\ 0 & K_{iQ\delta} \end{pmatrix} \tag{67}$$

$$\vec{I}_{\delta_{dq}}^* = C_{p\Gamma\delta}\bar{\Gamma}_{e\delta} + C_{i\Gamma\delta} \int \bar{\Gamma}_{e\delta}dt \tag{68}$$
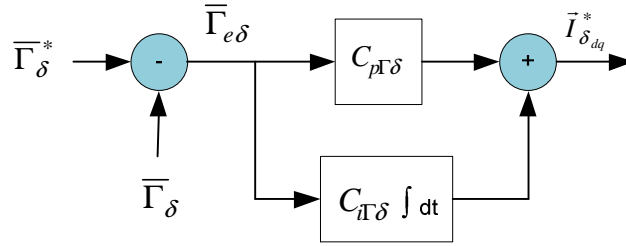
Figure 4.3: PILOT Power controller

4.4 Co-Pilot converter control system overview

In figure 4.4 is shown the co-pilot control system. The V_{DC}/Q controller is able to keep hold the V_{DC} voltage at the reference value and to control the reactive power exchanged between the co-pilot converter and the PCC of the feeder 2. So, in this way the power active balance in the DC link is assured as shown in the equation (69), where P_ε is the co-pilot active power, P_δ is the pilot active power, P_{EV} is the EV charging power and finally P_{loss} is the total active power losses (it is used the load convention). The control system has seven inputs: the grid 2 voltages in dq rotating frame, the converter currents in dq rotating frame, the DC link voltage and the set-points for the DC link voltage and for the three-phase reactive power. The controller outputs are direct and quadrature converter voltages. Thanks to the inverse Park transformation it is possible to obtain the three-phase

75

voltages to apply to the inputs of the three-phase LCL filter. Finally, to generate PWM signals to send to the IGBTs of the co-pilot converter, it is used the sinusoidal modulation with the third harmonic injection.
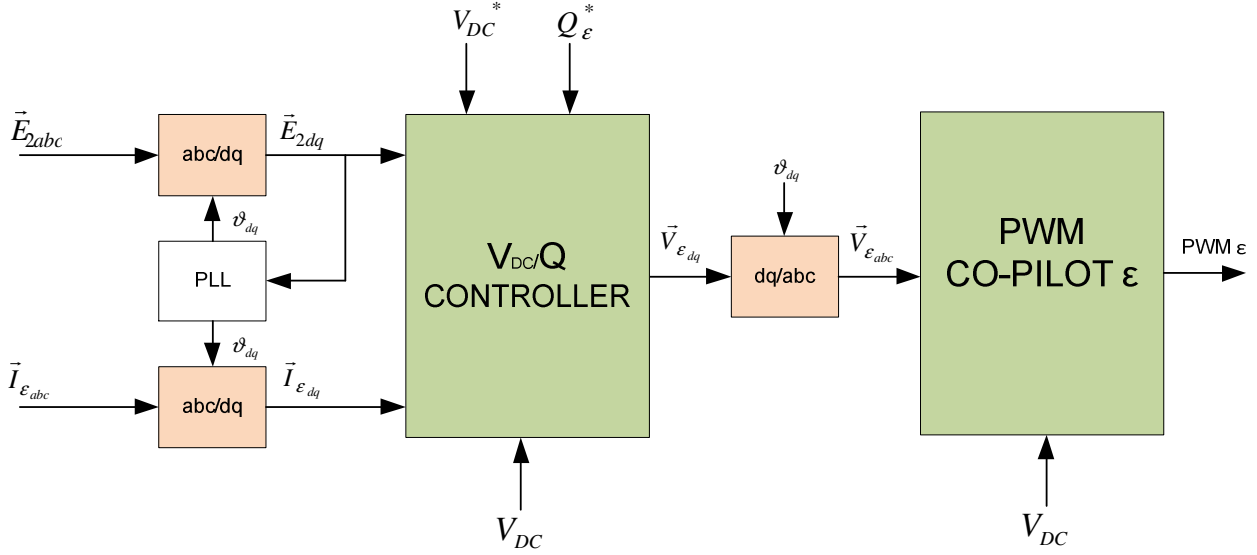
Figure 4.4: Co-Pilot Control system overview

$$P_\varepsilon = P_\delta + P_{EV} + P_{loss} \tag{69}$$

4.5 Co-Pilot current controller

The control system has two control loops; the first one is an inner loop and it is used to control the converter current, instead, the second one is an outer loop to control the DC link voltage and the reactive power. For the inner loop was used the PI regulators to obtain the current values equal to the set-points values at steady state. (70) shows the current set-points' vector, the currents' vector measured, the current errors' vector and the decoupling matrix. The proportional gains matrix and the integrator gains matrix are shown in (71). The gain values have been calculated considering the plant shown in figure 2.14, the integrator time constants τ_ε are equal to the RL circuit time constant. In this way, it is possible to obtain the fast-current response. To limit the overshoot to 5% in the transient the proportional gains are calculated with the damping equals 0.707 (T_s is the sampling

time, and the controller parameters are shown in (72)). With the equation (73), it is possible to obtain the control algorithm for the current inner loop as shown in figure 4.5 (the matrix U is the identity matrix).

$$
\vec{I}^*_{\varepsilon dq} = \begin{vmatrix} i_{\varepsilon d}^* \\ i_{\varepsilon q}^* \end{vmatrix} \quad \overrightarrow{I_{\varepsilon dq}} = \begin{vmatrix} i_{\varepsilon d} \\ i_{\varepsilon q} \end{vmatrix} \quad \overrightarrow{I_{e\varepsilon dq}} = \begin{vmatrix} i_{\varepsilon d}^* - i_{\varepsilon d} \\ i_{\varepsilon q}^* - i_{\varepsilon q} \end{vmatrix} \quad \Omega_\varepsilon = \begin{pmatrix} 0 & -\omega_{dq\varepsilon} L_\varepsilon \\ \omega_{dq\varepsilon} L_\varepsilon & 0 \end{pmatrix} \quad (70)
$$

$$
C_{pI\varepsilon} = \begin{pmatrix} K_{pI\varepsilon} & 0 \\ 0 & K_{pI\varepsilon} \end{pmatrix} \quad C_{iI\varepsilon} = \begin{pmatrix} K_{iI\varepsilon} & 0 \\ 0 & K_{iI\varepsilon} \end{pmatrix} \quad (71)
$$

$$
K_{pI\varepsilon} = \frac{L_\varepsilon}{3T_s} \quad \tau_\varepsilon = \frac{L_\varepsilon}{R_\varepsilon} \quad K_{iI\varepsilon} = \frac{K_{pI\varepsilon}}{\tau_\varepsilon} \quad (72)
$$

$$
\overrightarrow{V_{\varepsilon dq}} = C_{pI\varepsilon} \overrightarrow{I_{e\varepsilon dq}} + C_{iI\varepsilon} \int \overrightarrow{I_{e\varepsilon dq}} dt + \Omega_\varepsilon \overrightarrow{I_{\varepsilon dq}} + U\overrightarrow{E_{2 dq}} \quad (73)
$$
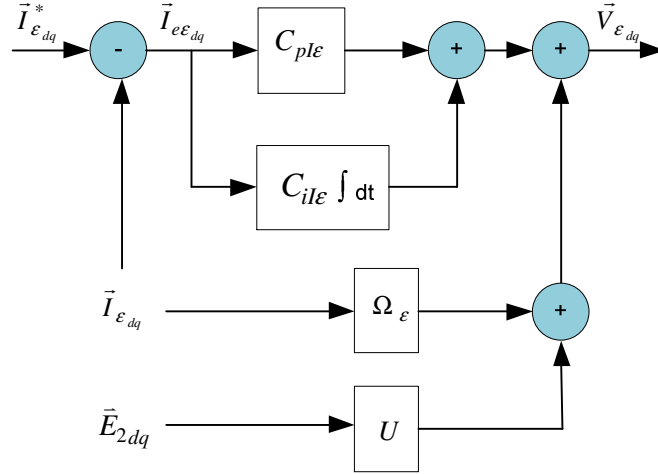
Figure 4.5: CO-PILOT Current controller

4.6 Co-Pilot power controller

The power controller is the outer loop to set the current set-points for the inner loop. To obtain the power values equal to the set-point values at steady state was used the PI regulators. (74) shows the voltage-power set-points' vector, the voltage-powers' vector measured, the voltage-power errors' vector and the decoupling matrix. The proportional gains matrix and the integrator gains matrix are shown in (75). The gain values have been calculated to have a slower dynamic than the current inner loop dynamic to assure a right working for the current controller. With the equation (76), it is possible to obtain the control algorithm for the current inner loop as shown in figure 4.6.

$$\bar{\psi}_\varepsilon^* = \begin{vmatrix} V_{DC}^* \\ Q_\varepsilon^* \end{vmatrix} \quad \bar{\psi}_\varepsilon = \begin{vmatrix} V_{DC} \\ Q_\varepsilon \end{vmatrix} \quad \bar{\psi}_{e\varepsilon} = \begin{vmatrix} V_{DC}^* - V_{DC} \\ Q_\varepsilon^* - Q_\varepsilon \end{vmatrix} \tag{74}$$

$$C_{p\psi\varepsilon} = \begin{pmatrix} K_{pV_{DC}\varepsilon} & 0 \\ 0 & K_{pQ\varepsilon} \end{pmatrix} \quad C_{i\psi\varepsilon} = \begin{pmatrix} K_{iV_{DC}\varepsilon} & 0 \\ 0 & K_{iQ\varepsilon} \end{pmatrix} \tag{75}$$

$$\vec{I}_{\varepsilon_{dq}}^* = C_{p\psi\varepsilon}\bar{\psi}_{e\varepsilon} + C_{i\psi\varepsilon} \int \bar{\psi}_{e\varepsilon} dt \tag{76}$$
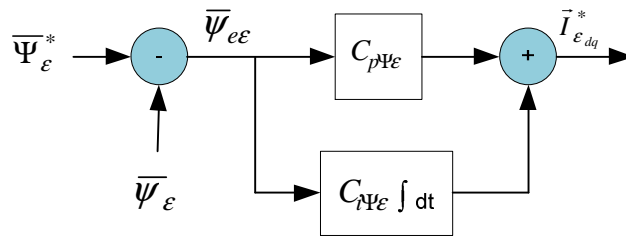
Figure 4.6: CO-PILOT Power controller

4.7 PLL for pilot and co-pilot converter

The pilot and the co-pilot control system work in dq rotating frame. The schemes of PLLs used for both converters are equal to the PLL scheme for the STATCOM and SSSC converters as explained in 3.2.1. For this device there are two PLLs; the power configuration it is the same of the HVDC

system where there is a DC link between two AC grids. Thus, it is possible to manage the active

and the reactive power between two grids with different frequencies and different line voltages.

The VOC technique has been used for both PLLs. (77) shows the PLL equation to obtain the

pulsation $\omega_{dq\delta}$ and (78) shows the dq rotating frame angle $\vartheta_{dq\delta}$ for the pilot converter control system.

Instead, (79) shows the PLL equation to obtain the pulsation $\omega_{dq\varepsilon}$ and (80) shows the dq rotating

frame angle $\vartheta_{dq\varepsilon}$ for the co-pilot converter control system. In figure 4.7 is shown the PLL schemes

for both converters.

$$\omega_{dq_\delta} = K_{pPLL}e_{1q} + K_{iPLL}\int e_{1q}dt + \omega_{ref_\delta} \tag{77}$$

$$\vartheta_{dq_\delta} = \int \omega_{dq_\delta}dt \tag{78}$$

$$\omega_{dq_\varepsilon} = K_{pPLL}e_{2q} + K_{iPLL}\int e_{2q}dt + \omega_{ref_\varepsilon} \tag{79}$$

$$\vartheta_{dq_\varepsilon} = \int \omega_{dq_\varepsilon}dt \tag{80}$$
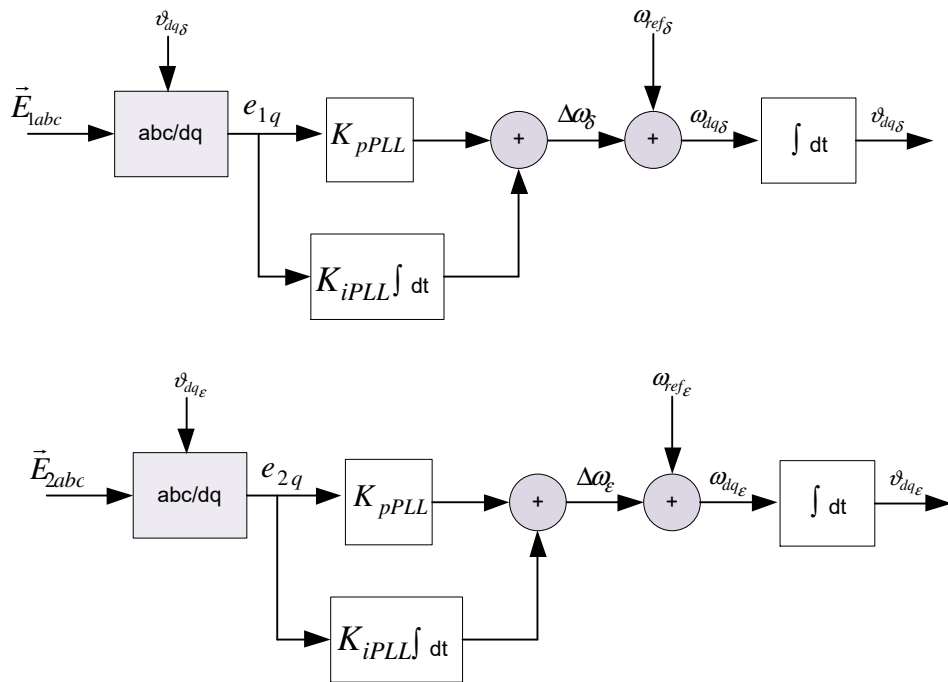
Figure 4.7: PLL for pilot and co-pilot converter

4.8 LCL filters

One of the most important aspect of power electronics is the current and voltage THD (Total Harmonic Distortion), so, to reduce it has been used LCL filters for both converters. In this way, the harmonic current i_h flows in LC mesh in the converter side as shown in figure 4.8. The current i_i is the converter current and i_g is the grid current, instead, i_c is the capacitor current. L_{fi} is the converter side inductance, L_{fg} is the grid side inductance and C_f is the filter capacitor. With the capacitor it is possible to have a low impedance at high frequency, so, the LCL attenuation is higher than the L or LC filter attenuation. In figure 4.9 is shown the LCL filter Bode diagram where is possible to see the filter attenuation equal to -60 dB/dec, instead, the LC filter attenuation is equal to -40dB/dec and the L filter attenuation is equal to -20dB/dec. The LCL transfer function between the grid current and the converter voltage is shown in (81).
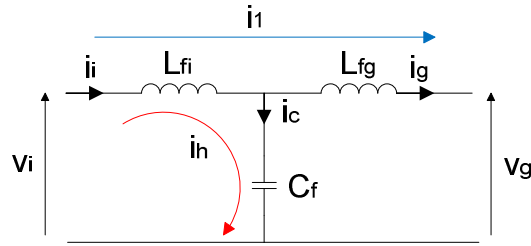

Figure 4.8: LCL filters

$$G_{LCL}(s) = \frac{I_g(s)}{V_i(s)} \tag{81}$$

Figure 4.9: LCL filter Bode diagram
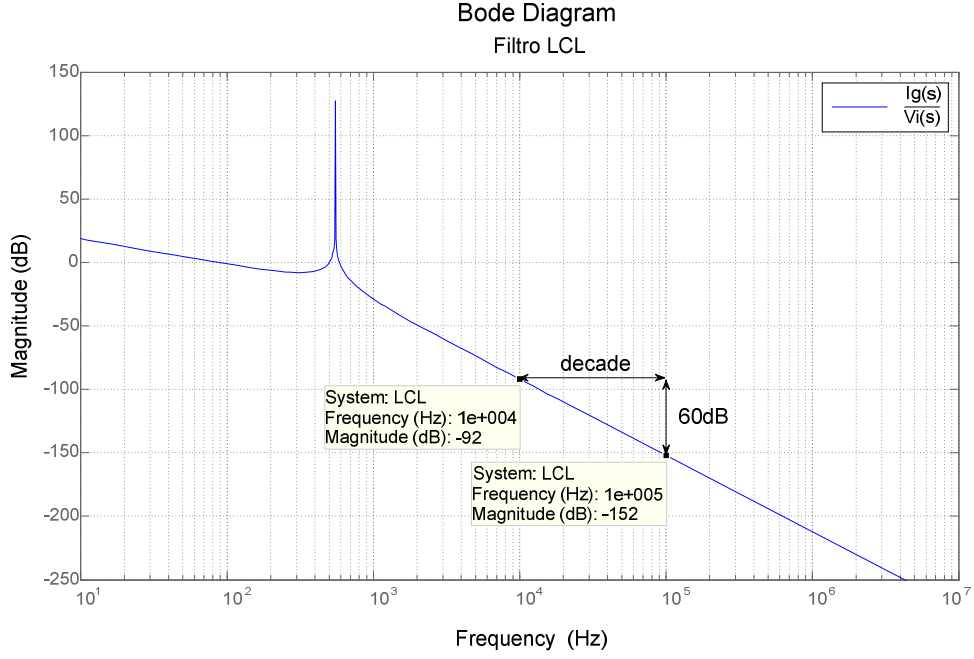
4.8.1 Design of LCL filter parameters

The converter side inductance L_{fi} is designed to obtain a converter current attenuation equal to 3% as shown in (82). So, the inductance value is calculated by (83) where ω_{sw} is equal to the switching frequency.

$$|G_{iLCL}(\omega_{sw})| = \frac{|I_i(\omega_{sw})|}{|V_i(\omega_{sw})|} = 0.03 \tag{82}$$

$$|Z_i(s)| = \frac{1}{0.03} = \omega_{sw}L_{fi} \quad \rightarrow \quad L_{fi} = \frac{1}{0.03\omega_{sw}} = 0.5 \, mH \tag{83}$$

The grid side inductance L_{fg} has been chosen equal to 1 mH and it is equal to the transformer inductance and the grid inductance. The capacitor has been designed by (84), with a reactive power equal to 1000 VAr (3% of the nominal apparent power). This reactive power has been compensated in the current control loop.

$$|Z_c(s)| = \frac{V^2}{Q} = \frac{1}{\omega C_f} \quad \rightarrow \quad C_f = \frac{Q}{V^2\omega} = 20 \ \mu F \tag{84}$$

The LCL filters parameters are equal for both grids, so the grid impedance (and transformer impedance) is the same for pilot and co-pilot converter.

4.8.2 Design of active damping for LCL filter

The transfer function for the converter side current is shown in (85) and figure 4.10 shows the Bode diagram for the G_{iLCL} (green line). R_g is the ohmic component of the grid impedance. The resonant peak causes the increment of the harmonic current component at the resonant frequency, so, to avoid this, has been used the active damping. In particular, it has been used the digital notch filter on the alfa and beta components on the output voltages for both converters [33].

$$G_{iLCL}(s) = \frac{I_i(s)}{V_i(s)} = \frac{L_{fg}C_f s^2 + R_g C_f s + 1}{(L_{fi}L_{fg}C_f)s^3 + (R_g C_f L_{fi})s^2 + (L_{fi}+L_{fg})s + R_g} \tag{85}$$

The transfer function G_{notch} is shown in (86), where ω_r is the LCL resonant frequency and δ_z and δ_p are the damping coefficients for the numerator and the denominator. In the figure 4.10 is shown in blue colour the Bode diagram for the G_{notch} where it is possible to see the notch in the magnitude response curve.

$$G_{notch}(s) = \frac{s^2 + 2\delta_z\omega_r s + \omega_r^2}{s^2 + 2\delta_p\omega_r s + \omega_r^2} \tag{86}$$

To see the effects of the digital notch filter, the transfer function G_{inew} has been calculated. (87) shows the transfer function G_{inew} and in the figure 4.10 in red colour is shown the Bode diagram for the new transfer function; the resonant peak has been avoided using the active notch filter.

$$G_{inew}(s) = \frac{I_i(s)}{V_i(s)} = \frac{L_{fg}C_f s^2 + R_g C_f s + 1}{(L_{fi}L_{fg}C_f)s^3 + (R_g C_f L_{fi})s^2 + (L_{fi}+L_{fg})s + R_g} \frac{s^2 + 2\delta_z \omega_r s + \omega_r^2}{s^2 + 2\delta_p \omega_r s + \omega_r^2} \quad (87)$$

Figure 4.10 shows all Bode diagrams for (85), (86) and (87). The design of the notch filter has
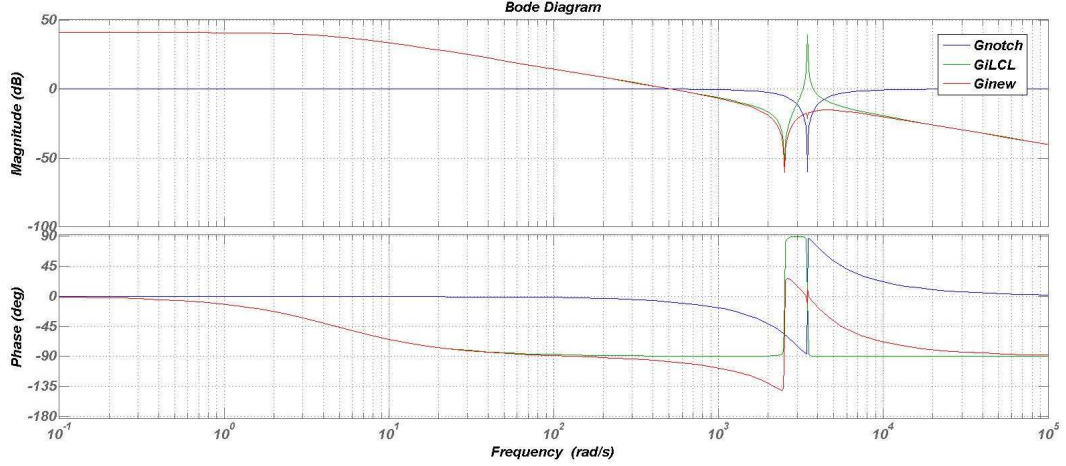
been made in according to [33].

Figure 4.10: LCL filter Bode diagram without and with active notch filter

4.9 Active low pass filter for feedforward PCC voltage

The main causes that increase the current Total Harmonic Distortion (THD) are discussed in [34].

There are several current control typologies [35], but for the three-phase converters, the most type

of controller used is the vector controller in dq rotating reference frame with the grid voltage

feedforward compensation on d-axis and on q-axis, so, it is necessary to measure grid voltages at

PCC to obtain direct and quadrature components. With VOC technique, the direct component will

be equal to the amplitude of the grid voltage and the quadrature component will be equal to zero at

steady state. If the voltage harmonic content at PCC is equal to zero, dq components of that voltages

are constant without ripple. But in the point of common coupling there are high frequency

harmonics due to the PWM modulation of the converter and the high frequency harmonics due to

other PWM converters in the micro-grid. In this way, the dq components of grid voltages measured

at PCC have a high ripple frequency. This ripple will be injected into the inner current control loop

after PI controllers and before the inverse Park transformation. So, the output current will have more harmonic content and higher THD value [36] [37]. It has been investigated the effect of the high frequency ripple in voltages at PCC on harmonic current emission and the feasibility to use low pass filters to obtain clean dq voltage feedforward signals for the current controller and to obtain hence the better current THD.

To design and to investigate the effect of low pass filters on the current controller, it has been considered the scheme of the plant and of the current controller in s-domain to analyze the current response for a step variation of the PCC voltage. To do this, the superposition principle has been used for the PCC voltage. In this way, it is possible to see the effect in terms of overshoot, delay of the current time response and the harmonic attenuation in the frequency domain. Figure 4.11 shows the scheme in s-domain for d axis and for q axis. The capacitor of LC filter is neglected because only the fundamental frequency for the current controller is considered for this study. The dynamic on d axis and on q axis is the same, so, to study the effect of a low pass filter on the feedforward voltage it is possible to use only one ring. Furthermore, introducing a transfer function on feedforward in the current inner loop, it doesn't change the dynamic of the current in response to the current reference input (without variations of the PCC voltage). Thanks to the integrator in $G_c(s)$, the current will have a natural rejection of the voltage measured at PCC at steady state.
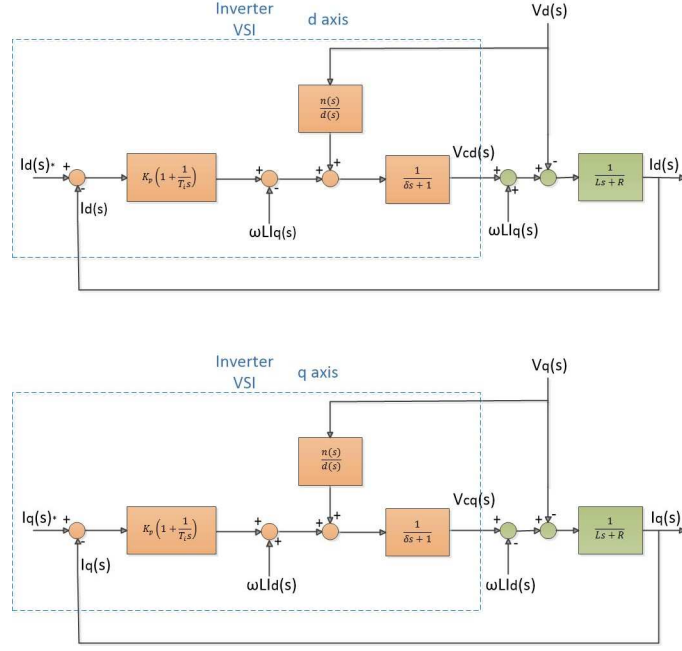
Figure 4.11: Control system and plant in dq frame

To know the effect in the time domain and in the frequency domain of low pass filters on the PCC voltage feedforward is needed to calculate the transfer function of the new system. To do this the superposition principle for the inner loop current has been used. For simplicity, I instead I_d or I_q is used to refer to current on d axis or on q axis. Furthermore, the decoupling components are neglected because they don't affect the current dynamic of the PCC voltage rejection. So, the scheme in s-domain has three inputs as shown in figure 4.12 and the current $I(s)$ is expressed with (88) where $I_0(s)$ is the component of current due to set-point and it has an optimal module dynamic thanks to the PI regulator, the $I_1(s)$ is the component of the current due to the voltage feedforward $V(s)$ with $G_f (s)$ and $I_2(s)$ is the component of the current due to the PCC voltage.
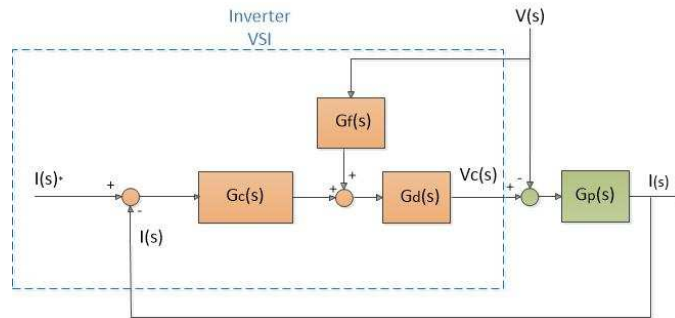

Figure 4.12: Simplified control system and plant in dq frame

$$I(s) = I_0(s) + I_1(s) + I_2(s) \qquad (88)$$

Figure 4.13 shows schemes in s-domain to associate the component $I_1(s)$ and $I_2(s)$ to the feedforward voltage with the low pass filter and the PCC voltage without the low pass filter. Now, it is possible to calculate the transfer function to obtain the time response and the frequency response of the PCC voltage rejection by current controller.
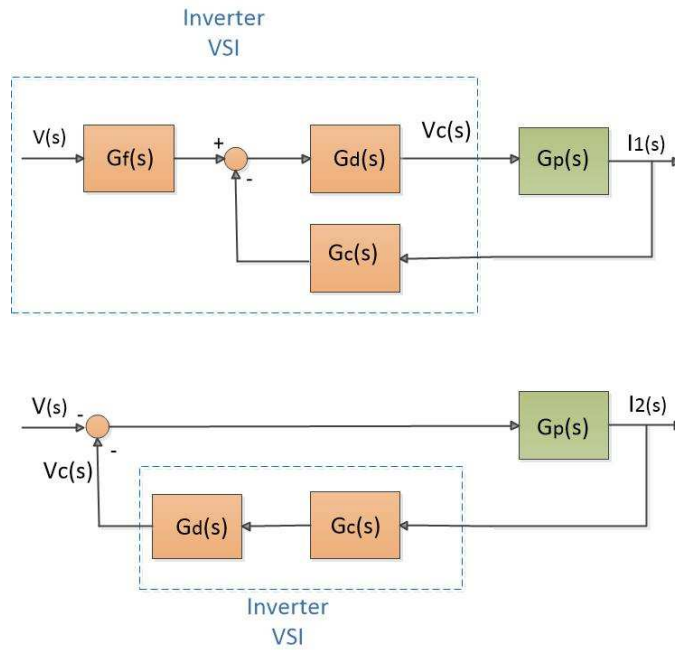
Figure 4.13: Scheme in s-domain to calculate I1(s) & I2(s)

There are three transfer functions associated to any components of the current $I(s)$, as in (89) G_0 is associated to the set-point input, in (90) $G_1(s)$ is associated to the feedforward voltage with the low pass filter and $G_2(s)$ in (91) is associated to the PCC voltage. In this way, it is possible to study the current $I(s)$ dynamic for current set-point variations or for PCC voltage variations due to load variations or other causes. (92) shows the mathematical formula to calculate the current $I(s)$ and to obtain the current dynamic. At steady state the current value is equal to the set point which attributes to integrator in $G_c(s)$ and the components associated to the PCC voltage inputs are equal to zero at steady state (93).

$$G_0(s) = \frac{I_0(s)}{I^*(s)} = \frac{G_c(s)G_d(s)G_p(s)}{1+G_c(s)G_d(s)G_p(s)} \tag{89}$$

$$G_1(s) = \frac{I_1(s)}{V(s)} = \frac{G_{f(s)}G_d(s)G_p(s)}{1+G_c(s)G_d(s)G_p(s)} \tag{90}$$

$$G_2(s) = \frac{I_2(s)}{V(s)} = -\frac{G_p(s)}{1+G_c(s)G_d(s)G_p(s)} \tag{91}$$

$$I(s) = I^*(s)G_0(s) + V(s)(G_1(s) + G_2(s)) \tag{92}$$

$$\lim_{s \to 0} sI(s) = I^* \tag{93}$$

Hence, to analyze the rejection dynamic with the low pass filter it is possible to refer to (94) where the transfer function R(s) allows to know the current I(s) dynamic in relation to the PCC voltage when the current set-point I*(s) is equal to zero.

$$R(s) = \frac{I(s)}{V(s)} = \left(G_1(s) + G_2(s)\right) \leftrightarrow I^*(s) = 0 \tag{94}$$

To obtain the R(s) with the time constant form a first order low pass filter transfer function G_f(s) (95) is supposed. In this way, it is possible to know the effect in the time-domain for variations of the PCC voltage and in the frequency-domain using the Bode diagram. The R(s) transfer function is calculated by (96) [38], the low pass filter introduces one zero and one pole. So, the rejection time is higher than the classical solution without LPF. This is very important aspect to choose the right value of the filter time constant α.

$$G_f(s) = \frac{1}{1+\alpha s} \tag{95}$$

$$R(s) = \frac{T_i s R^{-1}[1-(1+\alpha s)(1+\delta s)]}{(1+\alpha s)(1+\tau s)\left[T_i s(1+\delta s)+K_p R^{-1}\right]} \tag{96}$$

To design in right way the low pass filter for the feedforward voltage in the inner loop current it is important to choose between two main aspects. The first one is the cut-off frequency to obtain the better clean voltage value on d axis and on q axis, but at the same time, the second aspect is the time delay and the effect associated to the cut-off frequency. This is directly proportional to the time constant of the filter, so, it is not possible to obtain a low cut-off value with a short delay.

Without a low pass filter the rejection of the PCC voltage is very fast, the only delay is due to ADC and digital implementation of current controller with the microcontroller. In ideal case δ equals zero, the R(s) equals zero and the current I(s) equals only to $I_0(s)$. In this work to design the first order low pass filter, the rejection time delay has been chosen to a quarter of half period (2.5 ms) of the voltage waveform. In this way, the current controller is able to reject PCC voltage variations very fast, so α equals 0.0005 s and the cut-off frequency ω_b is equal to 2000 rad/s or about 318 Hz (97), then the pole value equals cut-off frequency. To know the current overshoot of the rejection response, the step response of the R(s) transfer function is shown in figure 4.14, and also the comparison between rejection response with the cut-off frequency ω_b equaling to 1000, 2000 and 3000 rad/s. The current overshoot due to PCC voltage variations is directly proportionally to the LPF time constant. So, if the cut-off frequency decrease the time delay and the current overshot increase. Therefore, the time delay and the overshoot are inversely proportional to the cut-off frequency ω_b. In figure 4.15 the current I(s) dynamic with current set-point $I(s)^*$ variations and with PCC voltage variations is shown. It is important to note that at time 0.18 s the set-point changes value from -1 to 5 A and in the current response there is not the rejection contribute because there are not any PCC voltage variations.

At 0.19 s instead, there is a PCC voltage variation equals -10 V (from 325 to 315 V) and there is the rejection dynamic by current controller. As shown in figure 4.15 the overshoot and the time delay introduced by LPF with a cut-off frequency equal to 1000 rad/s (red line) is higher than the time delay and the current overshoot using the LPF with the cut-off frequency equal to 3000 rad/s (fuchsia color).

$$\alpha = \frac{time\ delay}{5} \qquad\qquad \omega_b = \frac{1}{\alpha} \tag{97}$$

$$G_f(s) = \frac{1}{1+\alpha s} = \frac{\omega_b}{s+\omega_b} \tag{98}$$
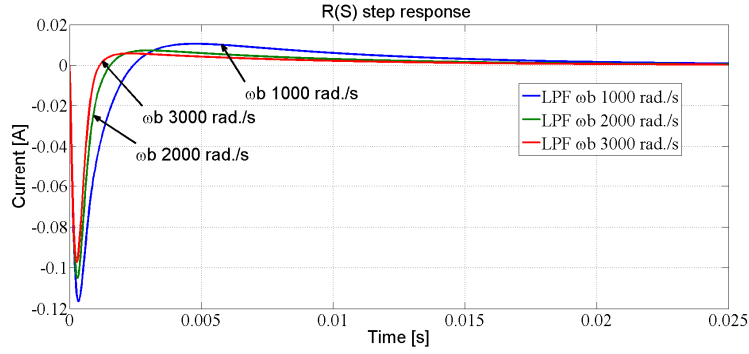
Figure 4.14: R(s) step response with LP filters
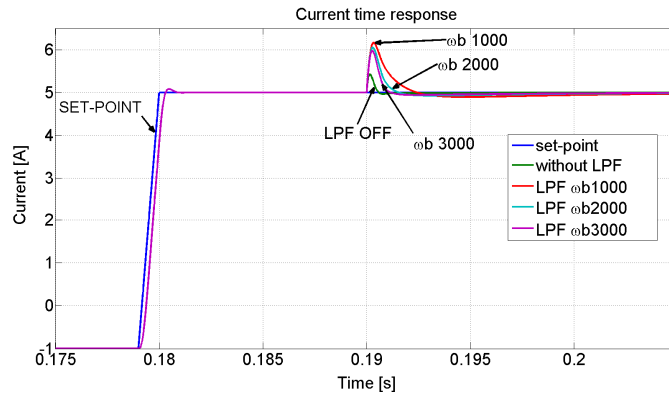
Figure 4.15: Current response with PCC voltage variations

To have better performances in terms of the current harmonic content it is possible to use high order filters. In this way the attenuation introduced is higher than the first order LPF. (99) - (102) are low pass filters with different order. Figure 4.16 shows the Bode diagram to compare the attenuation between LP filters with the cut-off frequency equal to 2000 rad/s in the frequency domain, instead, in figure 4.17 the step response in time domain for all different order filters is shown. With the increment of the LPF order the time delay and the overshoot increase.

$$G_{fB2} = \frac{4e6}{s^2+2828s+4e6} \tag{99}$$

$$G_{fB3} = \frac{8e9}{s^3+4000s^2+8e6s+8e9} \tag{100}$$

$$G_{fB4} = \frac{1.6e13}{s^4+5226s^3+1.366e7s^2+2.091e10s+1.6e13} \tag{101}$$

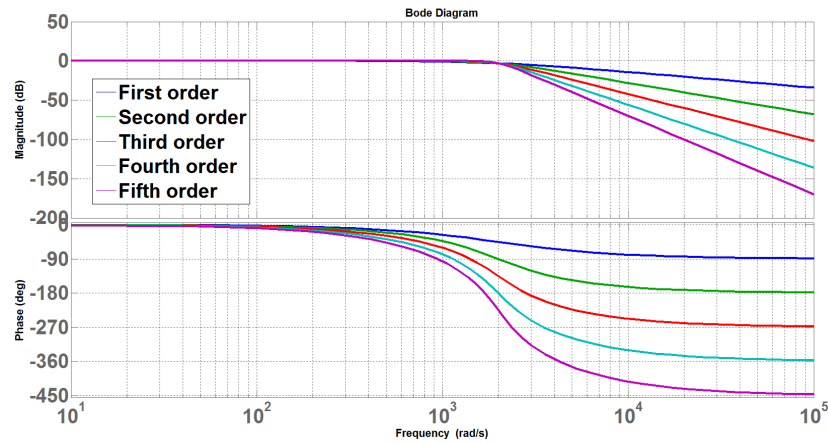$$G_{fB5} = \frac{3.2e16}{s^5+6472s^4+2.094e7s^3+4.189e10s^2+5.178e13s+3.2e16} \tag{102}$$

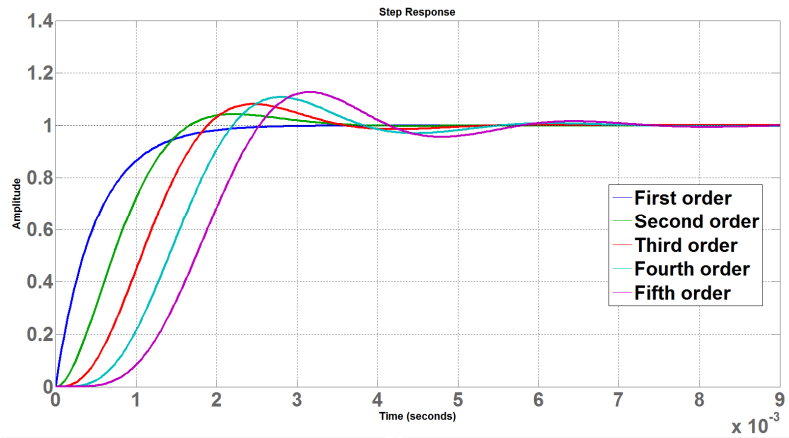**Figure 4.16:** Butterworth LPFs Bode diagram

**Figure 4.17:** Butterworth LPFs step response

The effects for the current harmonic distortion using a first order LPF for the PCC voltage feedforward has been investigated. In particular, to test low pass filters, the three-phase PWM inverter with 12 A as set point for current direct component i_d^* and 1 A for current quadrature component i_q^* has been used. The PLL works on the dq rotating frame and it's able to obtain that quadrature component of the PCC voltage equal to zero, and the direct component of the PCC voltage equals the voltage amplitude. In this case, the cut-off frequency is 2000 rad/s and the filter time constant equals 0.0005 s. The simulation with MATLAB/Simulink runs without LPF and after 0.1 s is activated the low pass filter for both voltage components in the rotating frame. In figure 4.18, it is possible to see the effect after the LPF is active at 0.1 s; the ripple on dq components of PCC voltages is strongly reduced using the low pass filter, so, in figure 4.19 LPF effects on PWM modulation signals are shown. In this way, the grid current has less ripple and in figure 4.20 grid currents for all phases before and after the first order LPF insertion at 0.1 s are shown. Thanks to the LPF the reduction of current THD is equal to 42%. With low pass filters, it is possible also to filter the noise ripple due to the acquisition electronic circuit board or to the voltage grid high frequency harmonic components.
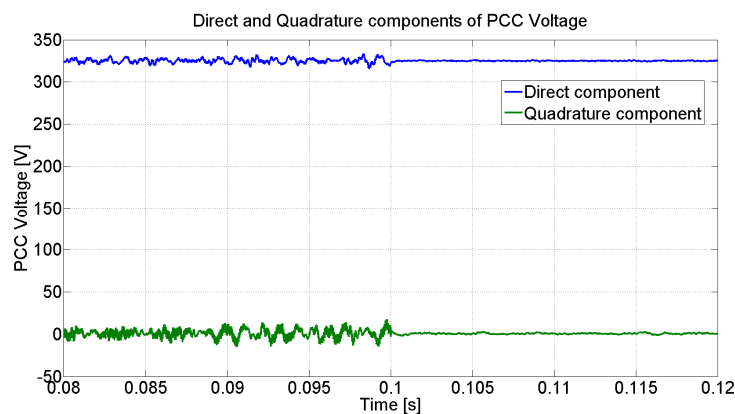
Figure 4.18: Direct and quadrature components of the PCC voltage

91
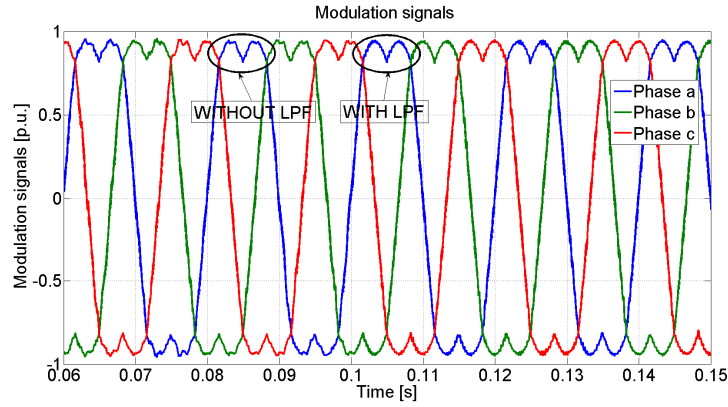
Figure 4.19: Modulation signals without and with LPF
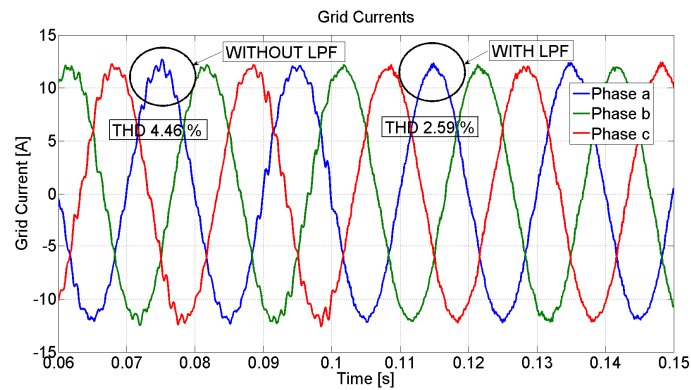
Figure 4.20: Grid currents without and with LPF

The disadvantage of the low pass filter has been examined with the LPF active for all simulation time. In figure 4.21 the PCC voltage step variation at 0.1 s equals -25 V is shown. Without LPF the PCC voltage rejection has not any overshoot in currents waveform as shown in figure 4.22, while, with the LPF active on direct and on quadrature components of the PCC voltage feedforward, during the step variation there is a current overshoot in grid currents waveform as shown in figure 4.23. This aspect confirms the mathematical considerations. Thanks to design of the LPF the time response is very fast and the rejection is completed in less of half period. So, using lower cut-off frequency, there will be a bigger overshoot in grid currents during the grid voltage variation. This is very important to considerate to design a low pass filter for the feedforward PCC voltage. So, to choose the right cut-off frequency must be made a compromise between the cut-off frequency and the overshoot in grid currents during a step variation of the PCC voltage.
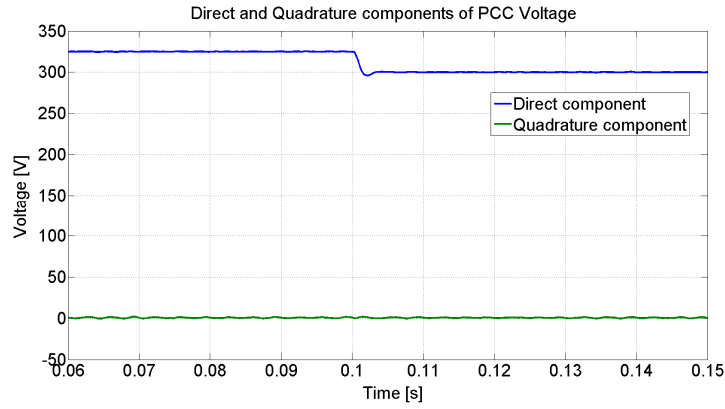
Figure 4.21: Direct and quadrature components of the PCC voltage
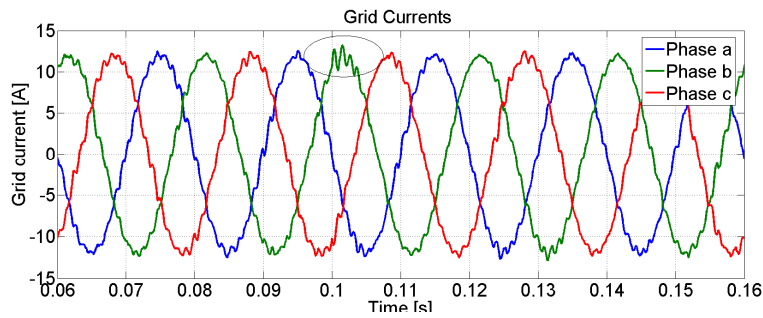
Figure 4.22: Voltage rejection at 0.1 s without LPF
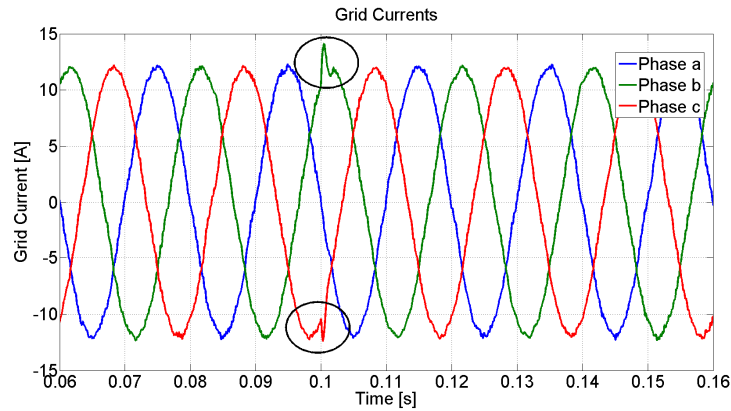
Figure 4.23: Voltage rejection at 0.1 s with the first order LPF

With the Butterworth filters from the second order to the fifth order it is possible to obtain more attenuation with the same cut-off frequency at low frequency, but with a more overshoot and more delay time than the one order first low pass filter as is shown in figure 4.17. To test effects of all Butterworth filters, has been made five simulations with the same cut-off frequency, to investigate the effect of low pass filters for the current harmonic distortion. In table 4.1 the current THD obtained for any low pass filters and without the LPF is shown.

TABLE 4.1: THD VALUES WITH BUTTERWORTH FILTERS

LPFs orders	Current THD [%]
Without filter	4.46
1	2.59
2	2.55
3	2.33
4	2.30
5	2.02

4.10 Power circuit and control parameters

In table 4.2 are listed the main technical parameters about the pilot power circuit, the co-pilot power circuit and the DC/DC power circuit including the filters parameters. Furthermore, in the table are shown the gains control parameters for all power electronics converters.

Table 4.2: DC charging station with B2B main technical parameters

Parameter	Value	Parameter	Value
Grid rated voltage feeder 1 [V]	400	LCL filters total inductance nominal value [mH]	1.5
Grid rated voltage feeder 2 [V]	400	DC link capacitor [μF]	1000
Grid rated frequency [Hz]	50	Battery resistance [Ω]	0.3
Ohmic component grid 1 impedance [Ω]	0.1	Pilot current loop proportional gain $K_{pI\delta}$ [V/A]	5
Inductive component grid 1 impedance [mH]	1	Pilot current loop integrator gain $K_{iI\delta}$ [V/A]	333.333
Ohmic component grid 2 impedance [Ω]	0.1	Pilot power loop proportional gain $K_{p\Gamma\delta}$ [A/W]	0.001
Inductive component grid 2 impedance [mH]	1	Pilot power loop integrator gain $K_{i\Gamma\delta}$ [A/W]	0.125
Pilot switching frequency [kHz]	10	Co-pilot voltage loop proportional gain $K_{pV_{DC}\varepsilon}$ [A/V]	0.25
Co-Pilot switching frequency [kHz]	10	Co-pilot voltage loop integrator gain $K_{iV_{DC}\varepsilon}$ [A/V]	3.333
DC/DC switching frequency [kHz]	10	Co-pilot reactive loop proportional gain $K_{pQ\varepsilon}$ [A/W]	0.001
Rated apparent power [kVA]	30	Co-pilot reactive loop integrator gain $K_{iQ\varepsilon}$ [A/W]	0.125
Rated EV charger power [kW]	20	Co-pilot current loop proportional gain $K_{pI\varepsilon}$ [V/A]	5
DC link Voltage [V]	650	Co-pilot current loop integrator gain $K_{iI\varepsilon}$ [V/A]	333.333
EV Charger Voltage [V]	200-500	DC/DC current loop proportional gain K_{pIEV} [p.u./A]	0.01
Battery voltage [V]	300	DC/DC current loop integrator gain K_{iIEV} [p.u./A]	1
Inductance LC filter DC side [mH]	5	DC/DC power loop proportional gain K_{pPEV} [A/W]	0.001
Capacitor LC filter DC side [μF]	50	DC/DC power loop integrator gain K_{iPEV} [A/W]	0.1

4.11 Test cases

To test the charging station with B2B, have been made two tests with MATLAB/Simulink software. In the first one, it is simulated the active and reactive power flow control with B2B converter integrated in the charging station, in particular, active and reactive power flow from grid 2 to grid 1 has been made by SSSC converter, so in this way, it is possible to avoid a congestion problem in the grid 1 or to decrease the grid 1 load increasing the grid capability. In the second one there is an active power flow inversion in the grid 2, so, with a proposed device, the excess green active power is used to charge the EV and at the same time it is used partially to supply the loads.

4.11.1 Case 1: active and reactive power flow control

In the study case 1, the charging station (with B2B configuration) is used to charge the EV and it is used to control the active and the reactive power flow between the grid 1 and the grid 2. In figure 4.24 is shown the test model where there is a load connected to the feeder 1. Thanks to the B2B integrated in the charging station at time equals 0.4 s the load is supplied from grid 1 and from grid 2, so in this way, the grid 1 has more capability or in the case of emergency contingency it is possible to improve the power quality using the B2B, in fact, it is possible to use the grid 2 to supply the grid 1 loads partially or totally due to the DC link in the charging station. The EV is supplied only by grid 2 for all simulation time.

In table 4.3 are reassumed the case 1 power values of the all components before and after the pilot converter operations at time equals 0.4 s.
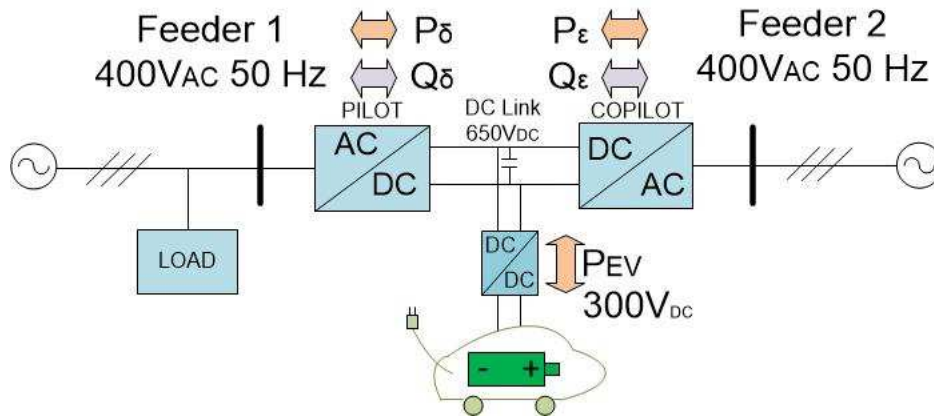
Figure 4.24: Case 1 test model

Table 4.3: Case 1 test power values

Active and reactive powers	*Before*	*After*
Grid 1 active power [kW] \ Load 1 active power [kW]	**10 \ 10**	**5 \ 10**
Grid 1 reactive power [kVAr] \ Load 1 reactive power [kVAr]	**4 \ 4**	**2 \ 4**
Grid 2 active power [kW]	**9**	**14**
Grid 2 reactive power [kVAr]	**-0.5**	**-0.5**
EV charging power [kW]	**9**	**9**

Figure 4.25 shows the active and the reactive power of the test model. The EV charging power is equal to 9 kW for all simulation time (it is not plotted for simplicity), instead, the active power flow between the two feeders is equal to 5 kW from grid 2 to grid 1 to supply partially the load on the feeder 1. The grid 2 reactive power is about zero (it is negative for the LCL filter capacitors) and the grid 1 reactive power is equal to 4 kVAr before the pilot converter start and after 0.4 s the grid 1 reactive power is equal to 2 kVAr. The pilot converter supplies a reactive power equal to 2 kVAr after 0.4 s and 5 kW to the grid 1 load. So, thanks to the proposed device it is possible to charge the EV and to supply the load 1 from both grids (5 kW from the grid 1 and 5 kW from the grid 2). The load used for the feeder 1 is a constant impedance load.
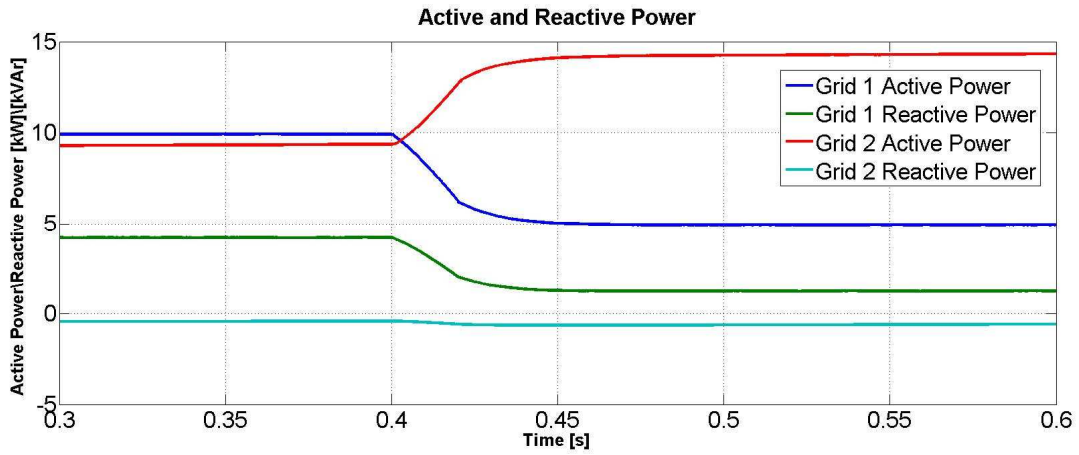
Figure 4.25: Test model active and reactive power

Figure 4.26 shows grid 1 line currents, where it is possible to see the decrease of the current magnitudes after 0.4 s due to the B2B that moves active power from the PCC of the feeder 2 to the PCC of the feeder 1 and the pilot converter supplies 2 kVAr as reactive power, so, the grid 1 supplies the load with 5 kW and 2 kVAr. Instead, in figure 4.27 are shown grid 2 line currents, where is shown the increase of grid 2 line currents after 0.4 s due to the 5 kW supplied from the grid 2 to the grid 1.
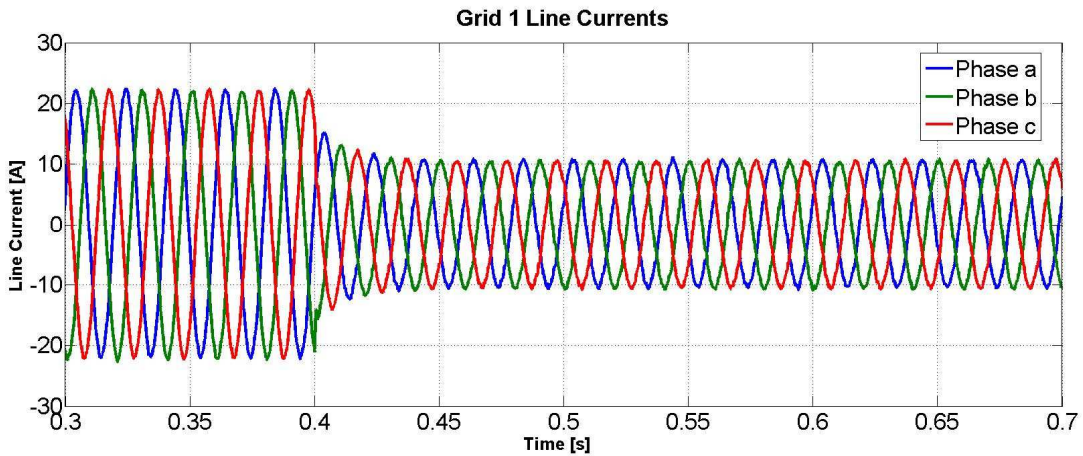
Figure 4.26: Grid 1 line currents
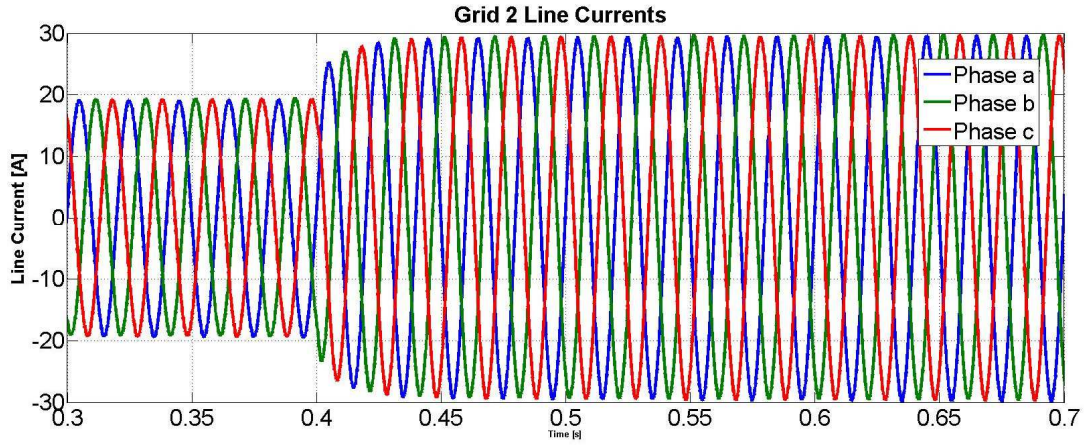
Figure 4.27: Grid 2 line currents

4.11.2 Case 2: active power flow inversion

In the study case 2 the charging station (with B2B configuration) charges the EV and it uses the green energy in the best way; in fact, thanks to the B2B at time equals 0.4 s the load on the feeder 1 is supplied from the solar generator and the EV charging power is constant for all simulation. In this way, in the grid 2 has been avoided the active power flow inversion and the green energy has been used to supply the load in the grid 1 and to charge the EV with only green energy. In figure 4.28 is shown the case 2 test model and in the table 4.4 are reassumed the case 2 power values of the all components before and after the pilot converter operations at time equals 0.4 s.

Figure 4.28: Case 2 test model

98

Table 4.4: Case 2 test power values

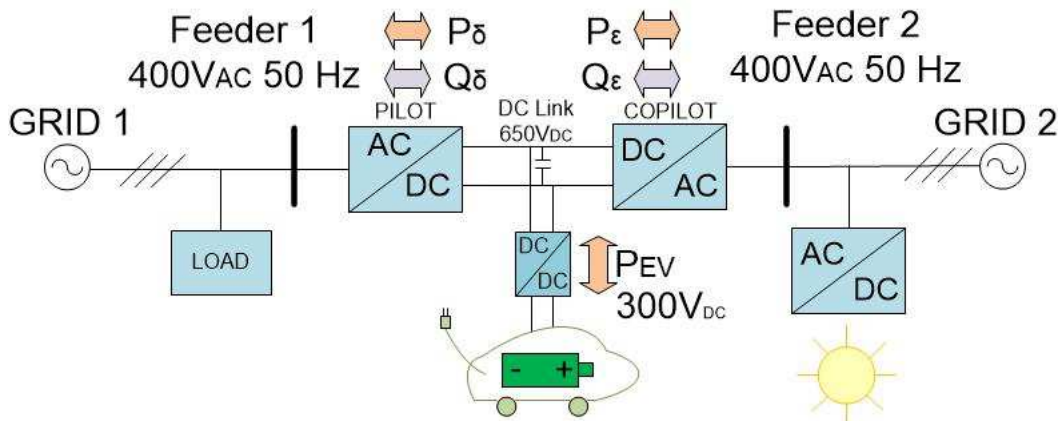| Active and reactive powers	Before	After
Solar active power [kW]	20	20
Grid 1 active power [kW] \ Load 1 active power [kW]	**20 \ 20**	**10 \ 20**
Grid 1 reactive power [kVAr] \ Load 1 reactive power [kVAr]	**9 \ 9**	**2 \ 9**
Grid 2 active power [kW]	**-10**	**0.5**
Grid 2 reactive power [kVAr]	**0**	**0**
EV charging power [kW]	**10**	**10**

Figure 4.29 shows the active and the reactive power of the test model. The EV charging power is equal to 10 kW for all simulation time (it is not plotted for simplicity). On the feeder 1 there is the load 1 with 20 kW and 9 kVAr and the power solar generation equals 20 kW. So before 0.4 s in the grid 2 there is an inversion of active power flow; the active power injected in the grid 2 is equal to 10 kW because the solar generator supplies the EV battery with 10 kW by co-pilot converter and the grid 2 with 10 kW. Using the pilot converter after 0.4 s, 10 kW are injected in the feeder 1 from the feeder 2. So, in this way, the grid 2 supplies only the active power losses and the active power flow inversion has been avoided.
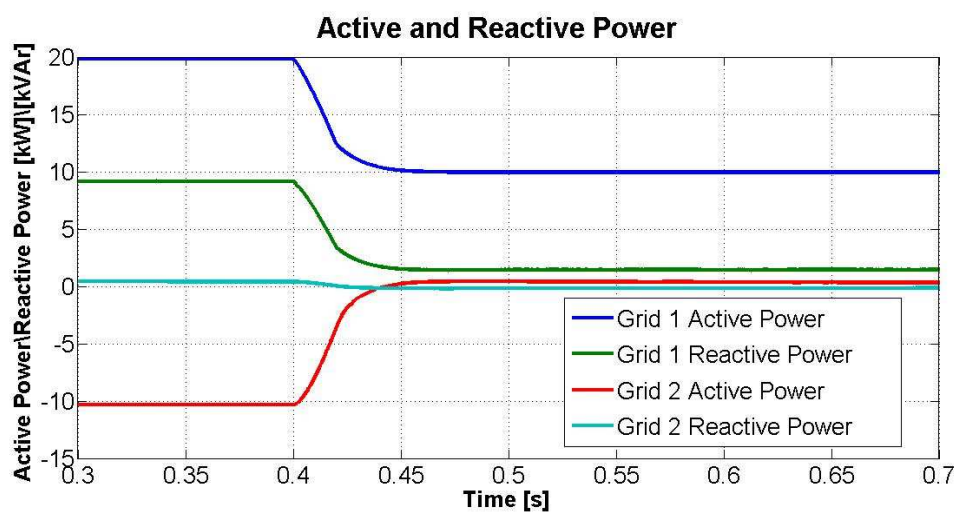
Figure 4.29: Test model active and reactive power

Figure 4.30 shows grid 1 line currents, where it is possible to see the decrease of the current magnitudes after 0.4 s due to the pilot converter that moves active power from the PCC of the feeder 2 to the PCC of the feeder 1. So, the grid 1 supplies partially the load with 10 kW and the solar power is used to charge the EV and to supply partially the load in the feeder 1. Instead, in figure 4.31 are shown grid 2 line currents, where is shown the decrease of grid 2 line currents after 0.4 s, in fact, the grid 2 supplies only the active power losses.

Figure 4.30: Grid 1 line currents

Figure 4.31: Grid 2 line currents

The DC/DC converter control performances are equal for both charging stations proposed (with UPFC and B2B converter).

Conclusion

In this work has been designed and tested two innovative solutions for LV grids; the charging station with UPFC and the charging station with B2B converter. Both solutions are able to charge the EV battery and at t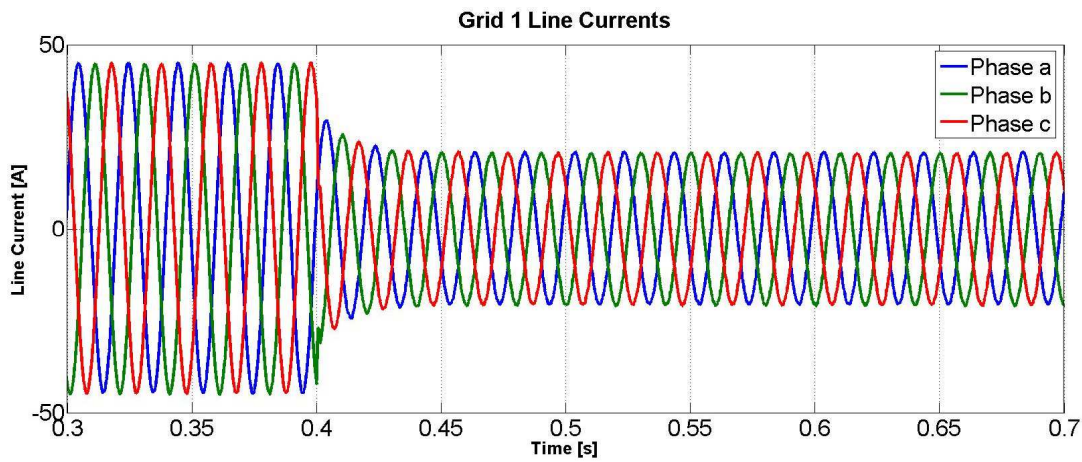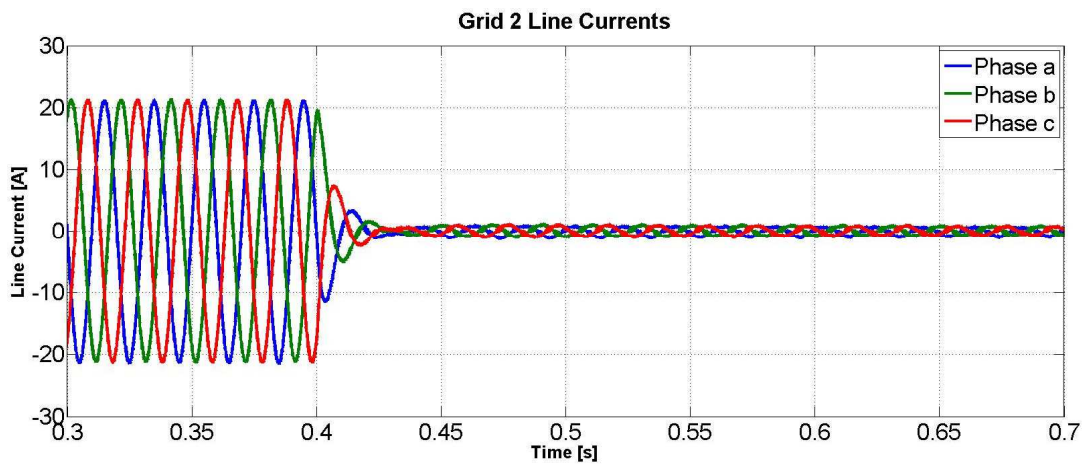he same time, thanks to the interline link between two feeders, they are able to control the active and the reactive power flow. The STATCOM converter (for the UPFC solution) is able to control the reactive power or the PCC voltage level, and both AC/DC converters for the B2B configuration are able to control the reactive and voltage level at PCC. So, with these converters, it is possible to manage in optimal way the LV grids, in fact, with the distributed charging stations it is possible to control the reactive/voltage profile on the LV feeder. Furthermore, with the AC link in the UPFC configuration and with the DC link in B2B configuration, it is possible to create the meshed grids and to manage the active and reactive power flow to avoid power flow inversion on one of two feeders to use in the best way the green energy and to reduce the total active power losses. Thus, using a central controller, it is possible to set the active and reactive power flow between two LV grids.

The charging station with UPFC solution uses the AC interline link, so, there is not decoupling between two feeders and it is not possible to control directly the SSSC PCC voltage, instead, with the charging station with B2B configuration, it is possible to control reactive or voltage profile for both PCC, so, this solution is more flexible than UPFC solution and there is the decoupling between two AC grids. With the B2B converter it is possible to interconnect two grids with different voltage level or with different frequencies. These solutions are cheap if in the AC grids there will be the growing of EV charging stations, so, it is possible to use an all-in-one solution without other devices to control reactive profile or voltage profile or to control active and reactive power flows between two feeders. The tests done with MATLAB/Simulink confirm the mathematical formulae for both solutions, and they confirm the proper functioning of the control systems designed.

So, the technical feasibility has been demonstrated for the proposed DC charging stations, but there are several future developments because the proposed solutions are new for the LV grid, and they have never been tested on the low voltage grid until now. The PWM B2B converter is very used for the HVDC and light HVDC systems, thus, the power and the current controller were studied and were tested on HV and MV grids, so, the future development for this converter is the realization and the installation on the LV grids to create and to manage the meshed systems. Instead, the UPFC solution is less common on the HV grids, for this reason there are more aspects to study; the series transformer works with low level voltage to the primary winding, so, it is important to determine the right winding ratio to obtain an optimal converter output voltage level, otherwise, the modulation index (for the SSSC converter) is too low and it is not possible to have a good voltage THD. The interline power controller for the UPFC, it is another important aspect to study and to implement to set the current set-points for the SSSC current controller.

Furthermore, for both DC charging stations, it is important to study the effects due to a short circuit on one of two feeders. Finally, one of the most important future development aspect is the local or central controller for these new LV components to set the active and reactive power set-points to optimal manage the LV systems to obtain the active power losses reduction and to use in the best way the green energy.

References

1. D. Kundu, "An Overview of the Distributed Generation (DG) Connected to the GRID", Joint International Conference on Power System Technology and IEEE Power India Conference, 2008. New Delhi, India, October 12-15th 2008;

2. H. Abu-Rub, M. Malinowski, K. Al-Haddad, "An Overview on Distributed Generation and Smart Grid Concepts and Technologies", Wiley-IEEE Press, 2014;

3. D. T. Ton, M. A. Smith, "The U.S. Department of Energy's Microgrid Initiative", The Electricity Journal, Volume 25, Issue 8, October 2012, pp. 84-94;

4. F. Nejabatkhah, Y. W. Li, "Overview of Power Management Strategies of Hybrid AC/DC Microgrid", IEEE Transactions on Power Electronics, Volume 30, Numero 12, December 2015;

5. B. O. Brewin, S. C. E. Jupe, M. G. Bartlett, K. T. Jackson, and C. Hanmer, "New Technologies for Low Voltage Distribution Networks", IEEE PES International Conference and Exhibition on Innovative Smart Grid Technologies (ISGT Europe), Manchester, UK, 5-7 Dec. 2011;

6. J. M. Bloemink, T. C. Green, "Benefits of Distribution-Level Power Electronics for Supporting Distributed Generation Growth", IEEE Transactions on Power Delivery, pp. 911-919, 24 January 2013;

7. D. De Santis, G. Abbatantuono, S. Bruno, M. La Scala, "Design of a 22kW Charging Station for LV distribution Grid control", INASE Conference Santorini, Greece, 17-21 Jul. 2014;

8. D. De Santis, G. Abbatantuono, S. Bruno, M. La Scala, "Low Voltage Grid Control through Electrical Vehicles Charging Stations", WSEAS Power System transaction, Dec. 2016;

9. W. Kempton, J. Tomic, "Vehicle-to-grid power implementation: from stabilizing the grid to supporting large-scale renewable energy", Journal of Power Sources, Vol.144, No.1, pp.280-294, 2005;

10. D. U. Sauer, M. Kleimaier, W. Glaunsinger, "Relevance of energy storage in future distribution networks with high penetration of renewable energy source", 20th International Conference and Exhibition on Electricity Distribution, 8-11 Jun. 2009;

11. J. Yang, M. Wang, Y. Zhang, D. S. Wang, F. F. Ye, "Applying power battery of electric vehicles for regulating peak in grid", East China Electric Power, Vol.38, No.11, 1685-1687, 2010;

12. Y. Ma, B. Zhang, X. Zhou, Z. Gao, Y. Wu, J. Yin, X. Xu, "An Overview on V2G Strategies to Impacts from EV Integration into Power System", 28th Chinese Control and Decision Conference (CCDC), Yinchuan, China, 28-30 May 2016;

13. D. De Santis, G. Abbatantuono, S. Bruno, M. La Scala, R. Sbrizzai "Feasibility of power flow control on LV distribution systems", INASE Conference Santorini, Greece, 17-21 Jul. 2014;

14. D. De Santis, G. Abbatantuono, S. Bruno, M. La Scala, R.Sbrizzai "Control of Power Flows in Low Voltage Distribution Systems", WSEAS Power System transaction, Dec. 2016;

15. H. Qin, R. Wu, A. M. Abd-el-Motaleb, L. Ran, X. Deng, P. Sensarma, "Utilisation of back-to-back VSC in a distribution network with DG", IEEE International Conference on Science of Electrical Engineering (ICSEE), Eilat, Israel, 16-18 Nov. 2016;

16. J. Alcalá, V. Cárdenas, R. J. Betancourt, J. Pérez-Ramírez, "Balancing the power of transformers in low voltage distribution feeders by using the Back - to - Back power converter", 8th International Conference on Electrical Engineering Computing Science and Automatic Control (CCE), Merida City, Mexico, 19 Dec. 2011;

17. J. Rocabert, A. Luna, Frede Blaabjerg, Pedro Rodríguez, "Control of Power Converters in AC Microgrids", IEEE Transactions on Power Electronics, pp. 4734 - 4749, 15 May 2012;

18. J. Liu, Y. Miura, T. Ise, "Power Quality Improvement of Microgrids by Virtual Synchronous Generator Control", Electric Power Quality and Supply Reliability (PQ), 2016, Tallinn, Estonia, 29-31 Aug. 2016;

19. G. Aurilio, D. Gallo, C. Landi, M. Luiso, V. Cigolotti, G. Graditi, "Low cost combined voltage and current transducer for Smart Meters", Proceedings of Instrumentation and Measurement Technology Conference I2MTC, Montevideo, Uruguay, 12-15 May 2014;

20. G. Aurilio, D. Gallo, C. Landi, M. Luiso, G. Graditi, "A low cost smart meter network for a smart utility", Proceedings of Instrumentation and Measurement Technology Conference I2MTC, Montevideo, Uruguay, 12-15 May 2014;

21. S. Depuru, L. Wang, V. Devabhaktuni, N. Gudi, "Smart meters for power grid-Challenges, issues, advantages and status", Power Systems Conference and Exposition (PSCE), Phoenix, AZ, USA, 20-23 Mar. 2011;

22. D. De Santis, D. A. Giampetruzzi, G. Abbatantuono, M. La Scala, "Smart Metering for Low Voltage Electrical Distribution System using Arduino Due", IEEE Workshop on Environmental, Energy, and Structural Monitoring Systems, Bari, Jun. 13-14th 2016;

23. G. Abbatantuono, S. Bruno, D. De Santis, M. La Scala, A. Naschetti, R. Sbrizzai, "Smart charging of electric vehicles for low voltage grids optimization", IEEE Workshop on Environmental, Energy, and Structural Monitoring Systems, Bari, Jun. 13-14th 2016;

24. D. De Santis, "A New DC Charging Station to Control Power Flows on Low Voltage Grids", International Journal of Science and Research, May 2017;

25. D. G. Cho and E. H. Song, "A simple UPFC control algorithm and simulation on stationary reference frame," IEEE International Symposium on Industrial Electronics ISIE 2001, Pusan, Korea, 12-16 Jun. 2001;

26. J. Joglekar, Y. Nerkar, "Application of UPFC for improving micro-grid voltage profile", IEEE International Conference on Sustainable Energy Technologies ICSET 2010, Kandy, Sri-Lanka, Dec. 2010;

27. M.A. Sayed, T. Takeshita, "Line loss minimization in isolated substations and multiple loop distribution systems using UPFC", IEEE Transactions on Power Electronics, Volume 29, Issue 11, pp. 5813-5822, Nov. 2014;

28. E. Rosas, V. Cárdenas, J. Alcalá, C. Núñez, "Active and Reactive Current Decoupled Control Strategy Applied to a Single-Phase BTB Converter", 6th International Conference on Electrical Engineering, Computing Science and Automatic Control, 10-13 Jan. 2009;

29. F. Belloni, R. Chiumeo, C. Gandolfi, M. Brenna, "Application of back-to-back converters in closed-loop and meshed MV distribution grid", AEIT Annual Conference - From Research to Industry: The Need for a More Effective Technology Transfer (AEIT), Trieste, Italy, 18-19 Sept. 2014;

30. C. Tang, Y. Chen, Y. Chen, Y. Chang, "DC-Link Voltage Control Strategy for Three-Phase Back-to-Back Active Power Conditioners", IEEE Transactions on Industrial Electronics, Volume 62, pp. 6306 – 6316, Oct. 2015;

31. T. Zhao, Q. Zong, T. Zhang and Y. Xu, "Study of Photovoltaic Three-Phase Grid-Connected Inverter Based on the Grid Voltage-Oriented Control," IEEE 11th Conference on Industrial Electronics and Applications (ICIEA), Hefei, China, 5-7 Jun. 2016;

32. K. M. Tan, V. K. Ramachandaramurthy, J. Y. Yong, "Bidirectional Battery Charger for Electric Vehicle", 2014 IEEE Innovative Smart Grid Technologies - Asia (ISGT Asia), Kuala Lumpur, Malaysia, 20-23 May 2014;

33. D. Ricchiuto, M. Liserre, D. De Santis, "Low-switching-frequency active damping methods of medium-voltage multilevel inverters", IEEE International Symposium on Industrial Electronics (ISIE), Hangzhou, China, 28-31 May 2012;

34. Q. Yan, X. Wu, X. Yuan and Y. Geng, "An Improved Grid-Voltage Feedforward Strategy for High-Power Three-Phase Grid-Connected Inverters Based on the Simplified Repetitive Predictor," IEEE Transactions on Power Electronics, vol. 31, pp. 3880-3897, Jul. 2015;

35. F. Blaabjerg, R. Teodorescu, M. Liserre and A.V. Timbus, "Overview of Control and Grid Synchronization for Distribuited Power Generation Systems," IEEE Transactions on Industrial Electronics, vol. 53, pp. 1398-1409, Oct. 2006;

36. X. Wang, X. Ruan, S. Liu and C.K. Tse, "Full Feedforward of Grid Voltage for Grid-Connected Inverter with LCL Filter to Suppress Current Distortion Due to Grid Voltage Harmonics," IEEE Transactions on Power Electronics, vol. 25, pp. 3119-3127, Sept. 2010;

37. H. Wu, "A Modified Grid Voltage Feedforward Method to Improve the Stability-Robustness of the Grid-Connected Voltage Source Converter under Weak Grid Conditions," Electricity Distribution (CICED), 2016 China International Conference on, Aug. 2016;

38. D. De Santis, M. Chen, "Design of Active Low Pass Filters to Reduce Harmonic Current Emission", 43rd Annual Conference of the IEEE Industrial Electronics Society (IES) IECON 2017, Beijing, China, 29 Oct.-1 Nov..